# HIERARCHICAL MICROSTRUCTURES TO OVERCOME THE CONFLICT BETWEEN STRENGTH AND TOUGHNESS OF HARD COATINGS: TIN/NI AS A MODEL SYSTEM

by

IGNACIO LOPEZ CABANAS

DISSERTATION

Submitted in partial fulfillment of the requirements
for the degree of Doctor of Philosophy at
The University of Texas at Arlington
August, 2022

Arlington, Texas

Supervising Professors:

Efstathios I. Meletis

Jon M. Molina-Aldareguia

# Abstract

HIERARCHICAL MICROSTRUCTURES TO OVERCOME
THE CONFLICT BETWEEN STRENGTH AND TOUGHNESS OF HARD COATINGS:
TIN/NI AS A MODEL SYSTEM

Ignacio Lopez Cabanas, Ph.D.

The University of Texas at Arlington, 2022

Supervising Professors: Efstathios I. Meletis & Jon M. Molina-Aldareguia

In the recent times, industry's production speed has been increasing and thus, the production of parts needs to adapt and so do the materials used to manufacture them. Hence, tools exposed to more extreme conditions using hard coatings need them to be more reliable.

In this work an improvement of the toughness of TiN/Ni coatings is achieved through the combination of different microstructures at different levels. This first part consisted on finding the optimum TiN/Ni composition by using a high throughput methodology for a faster analysis and the second on the combination of that composition with a multilayer structure to emulate nacre. The coatings prepared for the high throughput methodology were TiN/Ni with a Ni content ranging from 0 to 20 at.% in the same substrate by reactive magnetron sputtering with a continuous gradient. Since all the compositions were deposited under identical conditions any differences coming from deposition parameters are removed. By screening the mechanical properties, composition and microstructure it was found that TiN with around 10 at.%Ni presented the highest hardness and fracture toughness. These increments were found to be related to the formation a nanocomposite microstructure composed by equiaxed $\delta$-TiN grains surrounded by an amorphous tissue phase. The hierarchical addition of Ni first to TiN and then a multilayer system presents a similar hardness to pure TiN but much higher toughness. Analysis on the fracture mechanisms revealed that in all cases the crack propagates through the grain boundaries and particle interfaces. Additionally, the coatings were tested at 500°C, it was found that the multilayer system with TiN(10)Ni showed a ductile behaviour while the others were brittle, which is attributed to a higher Ni volume segregated into particles.

# Acknowledgements

I would like to thank my supervisors for their guidance during this project. Thank my girlfriend Gema, my family, as well as some very special friends Ally, Arturo, Clara, Coral, Jimena and Mario; without them supporting me and, honestly, just being there to talk, spend time together in the coffee breaks, skype calls, trips and walks around campus it has been what have made these years memorable.

I would also like to thank Yi Shen, who helped me learn the in-and-outs of the PVD system and characterization laboratory in UTA and Miguel Monclús as well as Manuel Avella whose technical assistance and expertise have helped to make this thesis possible. I wish to acknowledge J. Ferrer from the Centro Nacional de Aceleradores (CNA/CSIC) of Seville where the RBS measurements were carried out.

This investigation was supported by the European Research Council (ERC) under the European Union's Horizon 2020 research and innovation program (Advanced Grant VIR-METAL, grant agreement No. 669141. JMMA acknowledges funding from Comunidad de Madrid (IND2018/IND-9668). This project was also funded by the State Agency of Research through the Maria de Maeztu Unit of Excellence (CEX2018-000800-M).

# Contents

# List of Figures

# Chapter 1

# Motivation and objectives

Over the past years, extensive research on how to improve the hardness and the toughness of coatings has been made. This type of coatings are used in extreme conditions in which wear, high temperature and impacts are always present, such as in cutting tools. Hence, the high hardness and toughness requirements must be maintained at high temperatures to extend their lifetime. In order to accomplish this task, many different materials science and engineering approaches can be considered: from complex material selection based on atomic scale simulations to a more experimental approach based on the optimization of the microstructure of the coatings. This field keeps evolving and new solutions are found continuously to solve the challenges inherent to this type of coatings. Therefore, it is needed to understand how different deformation mechanisms responsible for the mechanical properties of hard coatings work, especially at high temperatures. Additionally, there is also a need to study hardening and toughening mechanisms and the interaction between them.

Among the approaches considered, this project concentrates on the optimization of the microstructure, based on the hierarchical addition of hardening and toughening mechanisms taking inspiration from nacre. Additionally, the choice of materials will be done based on literature, instead of by simulation screening, to be used as a proof of concept. For this purpose, nacre's microstructure could be divided into a nanocomposite microstructure added to a multilayer structure. The material system of choice is TiN and Ni, which allows the formation of a self-assembled structure due to the immiscibility of Ni in the TiN lattice and its lack of affinity for nitrogen [1], which segregates to the grain boundaries as a pure metallic phase. This

segregation refines the microstructure and increases the mechanical properties of the coating. However, the benefits of the formation of this microstructure only occurs at a very narrow range of compositions [2]. Therefore, in order to scan a wide range of compositions to find the Ni content at which the nanocomposite structure is formed, a high-throughput methodology is used. This method involves the deposition of a single coating with a continuous gradient in the composition and the mapping of the composition, phases and mechanical properties. Once the composition at which the nanocomposite microstructure is formed and performs best, is found, a multilayer system is added finalizing the formation nacre-like microstructure. Additionally, both microstructural changes will be analyzed separately taking a pure TiN coating as reference so the evolution and effect of each one change can be evaluated.

Thereby, the objectives of the project are the following:

- Find the TiN/Ni composition with the best mechanical properties by using a high throughput methodology to quickly screen a wide continuous range of Ni contents.
- Hierarchically combine different microstructural changes, hardening and toughening mechanisms to resemble nacre's microstructure and further increase the toughness without decreasing the hardness.
- Analyze the fracture mechanisms involved in the failure of the coatings at room temperature and 500°C related to the microstructural changes.

# Chapter 2

# Literature review

In this chapter a review on the microstructure of nacre and how the hierarchical addition of microstructures at different length scales allow the material to present a very high toughness using a high amount of a very brittle base material. In addition, a compilation of the materials and mechanisms that are currently being used in the field of hard-yet-tough coatings is presented. The review includes which type of materials are being used for these applications together with the most common processing techniques for them. Then, different mechanisms used for increasing their mechanical properties (hardness and toughness), are examined and finally, a brief assessment of which ones are most viable to work at high temperature is given and which changes could be used to mimic nacre's microstructure.

## 2.1 Hierarchical microstructure development

Over the last decades a lot of interest has risen towards imitating structures or materials present in living beings, which have been highly optimized by evolution to fulfill specific roles during the life of the organism. One of these materials is nacre, produced by mollusks for their shells in order to withstand impacts and has been the focus of many studies due its high fracture resistance despite being mostly made from a brittle compound. Nacre is a biomaterial composed of 95 wt.% aragonite (a crystallographic form of $CaCO_3$) and 5 wt.% organic polymers, which due to its unique microstructure presents a much higher toughness than monolithic ar-

agonite. This microstructure consists of a complex hierarchical build up across different length scales, which consists of hexagonal tiles of aragonite layered and bonded by an organic matrix as shown in figure 2.1. Furthermore, the aragonite platelets are not monolithic bricks but nanograins surrounded by a nanoscale organic network which present higher ductility than monolithic aragonite [3, 4].

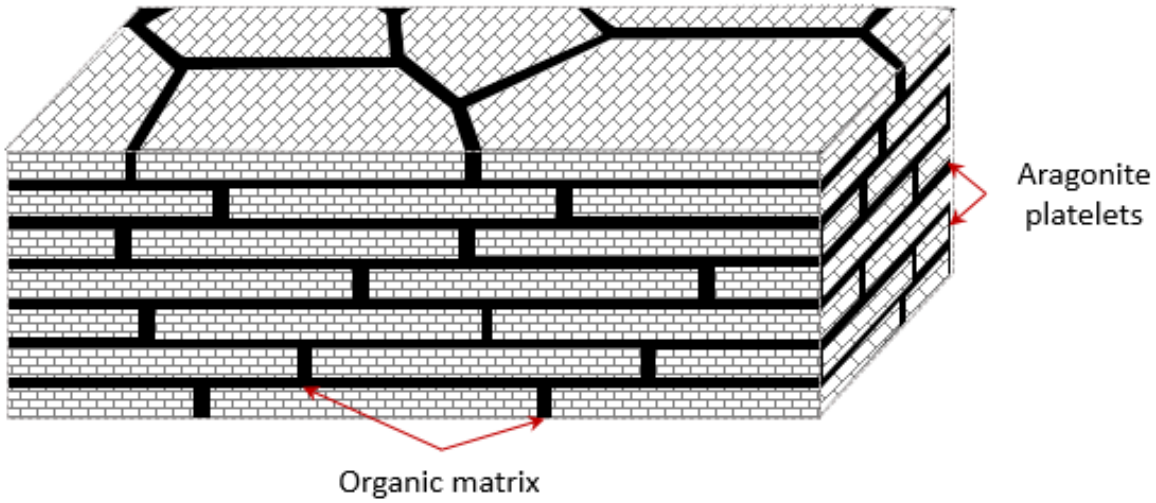


Figure 2.1: Schematic illustration of the microstructure of nacre.

Having a brick-and-mortar like structure allows the material to be able to deflect cracks at the organic layer and deform plastically by buckling. In addition to the previous microstructure, the tiles are rough, present some waviness and are linked by small bridges as it can be seen in figure 2.2 [5]. These too allow to add more resistance to the relative movement of the tiles when subjected to shear stresses.

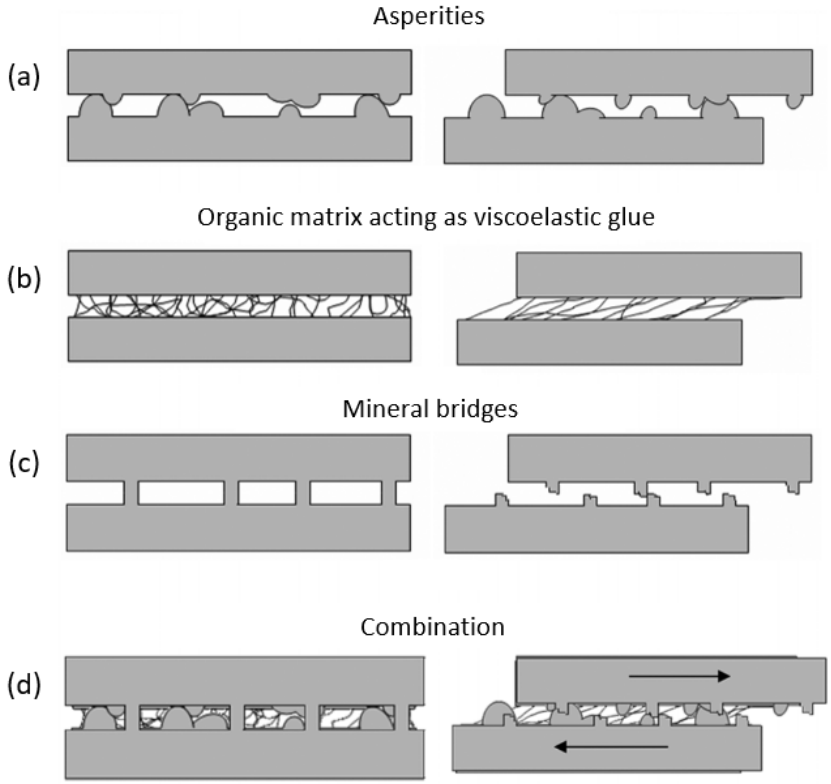


Figure 2.2: Schematic illustration of the different model for sliding between tiles: (a) inter-tile asperities, (b) organic layer acting as glue, (c) mineral bridges and (d) combination of the three mechanisms [6].

The addition of all these energy dissipation mechanisms thanks to the microstructural changes to pure aragonite increase the toughness of the material from 1 MPa $m^{1/2}$ to 3.3-9 MPa $m^{1/2}$ [7, 8]. As it was seen, the toughness increment is very substantial, thus it is possible that trying to replicate some elements of the unique microstructure of nacre and adding other mechanisms specific of the material choice, the toughness of hard coatings can be increased without a relevant loss of hardness.

## 2.2 Material families

Due to the industrial needs, coatings need to combine high hardness and toughness to be able to withstand the severe working conditions they are exposed to. However, these properties have to be maintained with temperature, hence coatings with high thermal stability are required. Additionally, the coatings must be formed by compounds with a high melting temperature and

a high oxidation resistance. Transition metal nitrides (TMN), with composition $MeN_x$ where Me = Cr, Mo, Nb, Ta, Ti or Zr for instance, fulfill these requirements. In order to improve their properties they are usually combined between them or with other elements like Si, B or C, giving rise to different microstructures [9–12].

Nevertheless, these chemical compositions are hard to obtain by conventional production methods, thus plasma deposition techniques are used for this purpose. Chemical Vapor Deposition (CVD) and Physical Vapor Deposition (PVD) together with their different variants are the processing techniques of choice when it comes to this type of materials and morphology [10, 12].

## 2.3 Strategies to improve the mechanical properties of hard coatings

In this section, a brief review of the strategies that have been proposed to improve the hardness and the toughness of hard coatings is made. The objective is to get a better understanding of the mechanisms responsible for the toughness and hardness enhancement and how these mechanisms might be affected by temperature.

### 2.3.1 Hardness-improving mechanisms

1. **Grain size refinement.** Reducing the grain size of the material leads to an increase of the hardness due to reduction of the pile-up of dislocations at the grain boundaries. Dislocation pile-ups at grain boundaries create a stress on the leading dislocation that facilitates grain boundary transmission. Hence, a reduction in grain size, reduces the length of the pile-up and the associated stress field, leading to a stronger material. The increment in hardness with grain size reduction is given by the Hall-Petch relationship [13, 14].

$$H = H_0 + k \cdot d^{-1/2} \tag{2.1}$$

where $H_0$ is the intrinsic hardness, k is the Hall-Petch constant and d is the grain size. However, the increase in hardness due to the reduction in grain size reaches a limit when the deformation mechanisms change from dislocation movement to grain boundary sliding, as shown in figure 2.3, which typically occurs for grain sizes < 10 nm. Nevertheless, this hardening mechanism might not be as effective at high temperature as it is at low temperatures, due to the activation of thermally activated dislocation climbing or diffusion assisted grain boundary sliding [15].

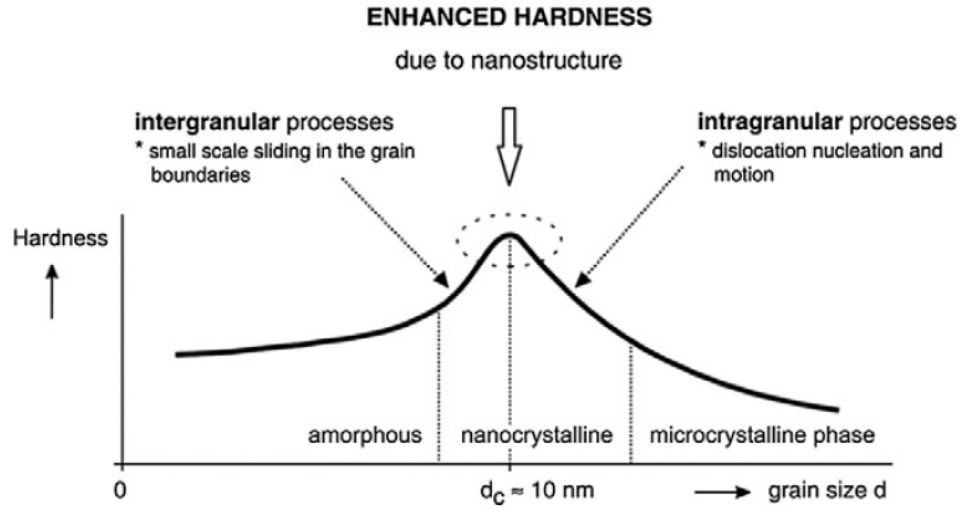


Figure 2.3: Schematic illustration of the effect of the grain size in the hardness [16].

2. **Grain boundary reinforcement.** Grain boundary sliding is a deformation mechanisms that can be activated for small grain sizes, specially at elevated temperature, thus limiting the hardness of the material. This can be prevented by anchoring the grain boundaries. Possible strategies include the modification of the grain boundaries, either by the use of precipitates or by inducing a nanocomposite structure, where the nanocrystalline grains are embedded in a strong matrix that reinforces the grain boundaries. An example of this type of strategy is found in nc-TiN/a-$Si_3N_4$ nanocomposite coatings, where a thin amorphous $Si_3N_4$ tissue surrounds the crystalline TiN nanograins, which prevents them from sliding against each other. Ideally, this tissue should be an extremely thin interfacial layer (a few atomic layers), as the hardness is dependent of the amount of matrix present in the coating. The evolution of the hardness with amount of Si for nc-TiN/a-$Si_3N_4$ can be seen in figure 2.4 [9, 17, 18], which shows a peak in hardness for a narrow Si content

that complies with this requirement.

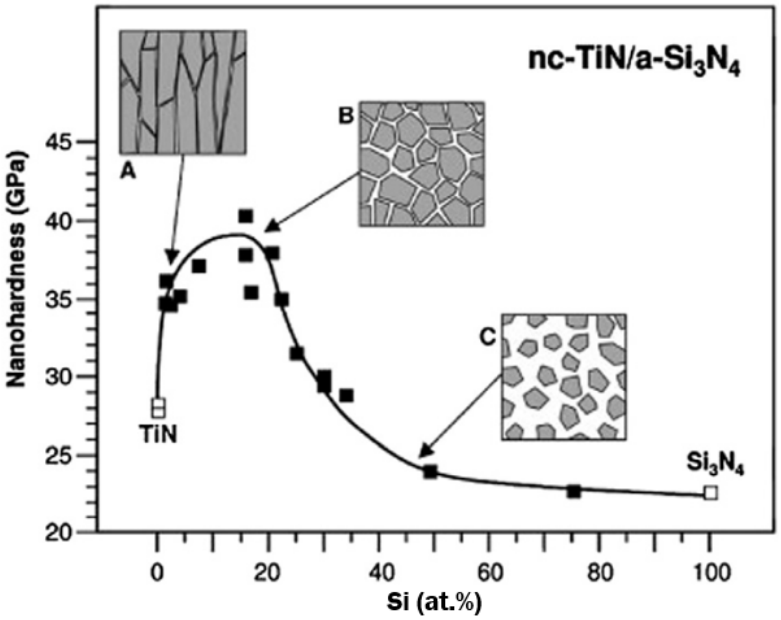


Figure 2.4: Hardness of nc-TiN/a-$Si_3$ $N_4$ evolution with the silicon nitride fraction [9].

Another alternative to strengthen the grain boundaries might be the introduction of a metal that does not form a nitride and that possesses a low solid solubility in the TMN. Material systems such as TiN/Ni [2, 19], ZrN/Ni [20, 21] or ZrN/Cu [22] have been studied for this reason. For a sufficient amount of metal, phase separation should lead to the formation of a coherent metallic layer that surrounds the TMN crystallites, which, on top of strengthening the grain boundaries, can increase the hardness by impeding dislocation transmission. Different mechanisms can act in this case, including strengthening due the differences on the shear modulus between the nitride and the metal [23] or due to coherency strains arising from the lattice parameter difference between them [24].

3. **Ion Bombardment.** Magnetron sputtering is a deposition technique in which some degree of bombardment of energetic particles (ions and, to a less degree, neutral atoms from the plasma) during deposition might arise. Due to this, coatings produced by this technique typically have better adhesion to the substrate and a higher density, due to re-sputtering effects, than those produced by evaporation. In addition, ion bombardment leads to the creation of more nucleation sites, which can help with the formation of nanocrystalline microstructures. Additionally, it might be responsible for the introduction of

intrinsic residual stresses and the creation of lattice defects that impede the motion of dislocations and hence increase the hardness [9].

The residual stresses and defects introduced depend on the energy of the bombarding ions which can be accelerated against the growing film by the application of a bias voltage to the substrate. As can be seen in figure 2.5, the residual stresses and the hardness increase as the bias voltage increases [3].

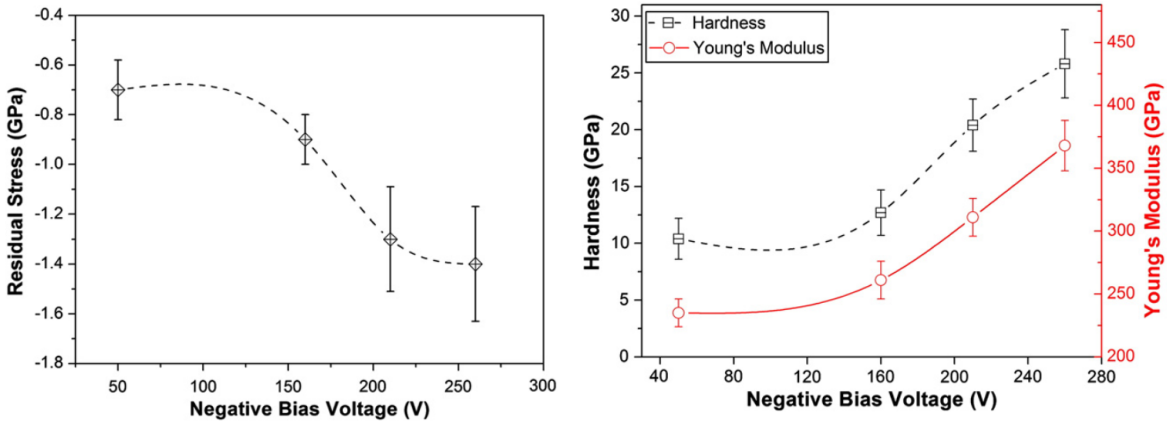


(a) (b)

Figure 2.5: Evolution of the compression residual stress and hardness of CrAlN as a function of the bias voltage [3].

Although this mechanism is effective at low temperatures, residual stresses relieve and lattice defects are annealed out through recovery and recrystallization processes at high temperature. Hence this hardening mechanism is not typically effective at elevated temperatures. Moreover, it might create adhesion problems.

4. **Multilayer and superlattice structure.** By modifying the architecture of the coating at the nanoscale, improved hardness can be achieved. As it was demonstrated by Helmersson *et al.*, a coating formed by alternating layers of two materials with different elastic constants, but a coherent crystalline structure, presented much higher hardness than single crystals of any of the components by themselves [25].

   For superlattices, the hardness presents a strong dependency on the invidual layer thickness. This is typically quantified by the bilayer period ($\Lambda$) or modulation wavelength.

By decreasing the size of $\Lambda$, the hardness increases up to a maximum for bilayer periods of a few nanometers, as can be seen in figure 2.6.

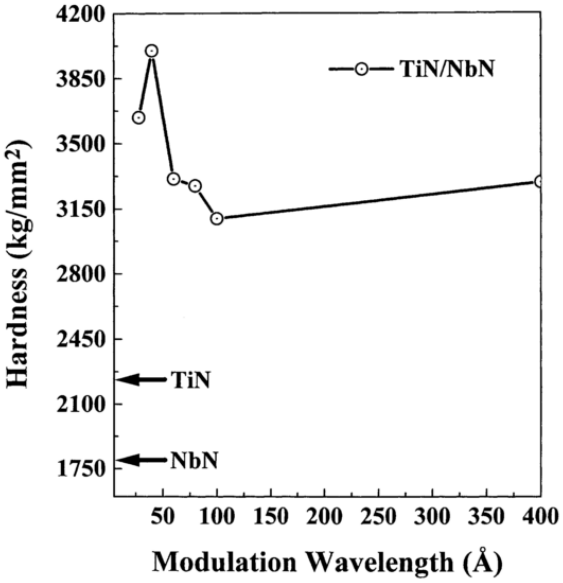


Figure 2.6: Hardness dependency with the modulation period of TiN/NbN multilayer coating compared to the hardness of single layer coatings of each of the constituents separately [26].

The super-lattice effect can be achieved even by using materials with incoherent lattices, or even when one of them grows amorphous, by reducing the layer thickness until the amorphous phase crystallizes by epitaxial growth on top of the other crystalline layer [27, 28]. However, not all material combinations present the superlattice effect [29].

### 2.3.2 Toughness-improving mechanisms

Another important property that hard coatings should present is fracture toughness, because being able to withstand impacts is of vital importance in industrial processes. However, toughness and hardness are competing material properties, meaning that when one of them is increased the other one tends to be reduced[29]. Therefore, to overcome this problem, new strategies are being investigated in order to increase toughness without reducing or sacrificing the hardness of the coating [11]. The following mechanisms represent different approaches to tackle this problem.

1. **The introduction of a toughening agent**

   (a) *The introduction of a ductile phase.* This is a direct way to increase the toughness. This phase can be in the form of a ductile matrix (metal matrix composite), as in ZrN/Cu [22], or of disperse precipitates (ceramic matrix composite), as in TaN/Cu [30].

   Co-sputtering different amounts of Ni together with nc-CrAlN/a-$SiN_x$, disperse Ni nanoparticles were found embedded in the a-$SiN_x$ matrix surrounding CrAlN nanograins [31]. Both mechanisms help the material to be more cracking resistant and contribute to the relaxation of the stresses at the crack tip. This way the material becomes much tougher at the expense of a hardness reduction, as shown in figure 2.7 for Ni contents up to 12% .

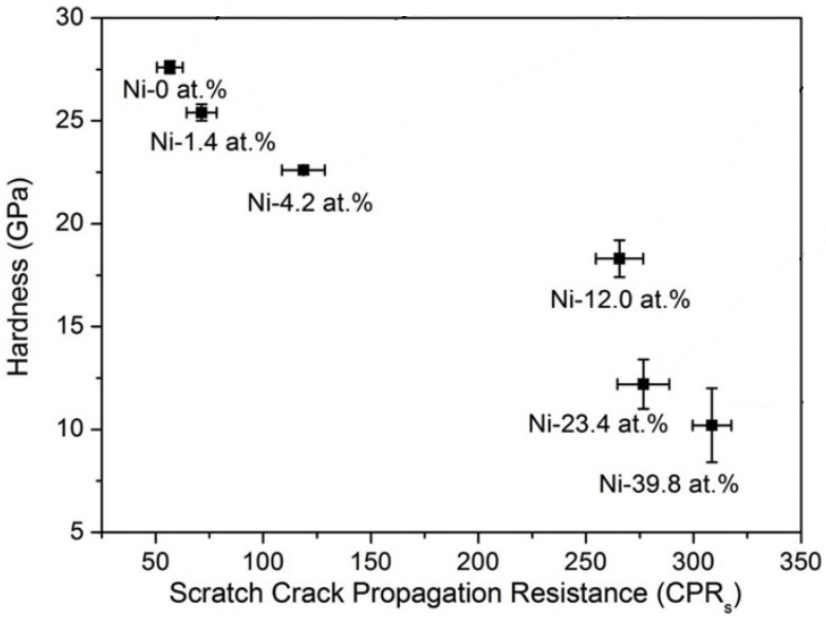


Figure 2.7: Hardness versus scratch toughness showing the effect of Ni in nc-CrAlN/a-$SiN_x$ [31].

   (b) *The introduction of Carbon Nanotubes (CNT).* CNTs have been proposed as toughnening agents, through crack deflection at the nanotube/matrix interfaces, crack bridging and pull-out mechanisms. However, producing coatings with the right orientation of homogeneously distributed CNTs is difficult and if not done properly, it causes a reduction on the toughening effect [9].

2. **Phase transformation toughening.** It involves a phase transformation with a volume increase of the material through which the crack is propagating. This volume increase consumes a large amount of energy and creates compression stresses at the crack tip which slow its propagation, increasing the toughness of the material [32, 33]. However, this toughening mechanism is very material specific and therefore it is rare to be able to use it.

3. **Compressive stress toughening.** Since cracks propagate by tensile stresses, introducing compressive residual stresses into the coating increases the required stress to propagate the crack. However, too high compression stresses produce detrimental effects such as poor adhesion, delamination and micro-cracks which decrease the toughness [9]. As it is shown in figure 2.5, the compressive stresses increase with the bias voltage. Hence increasing the bias, increases the toughness to a certain limit as it can be seen in figure 2.8, where the toughness decreases when increasing the bias from 210V to 260V.

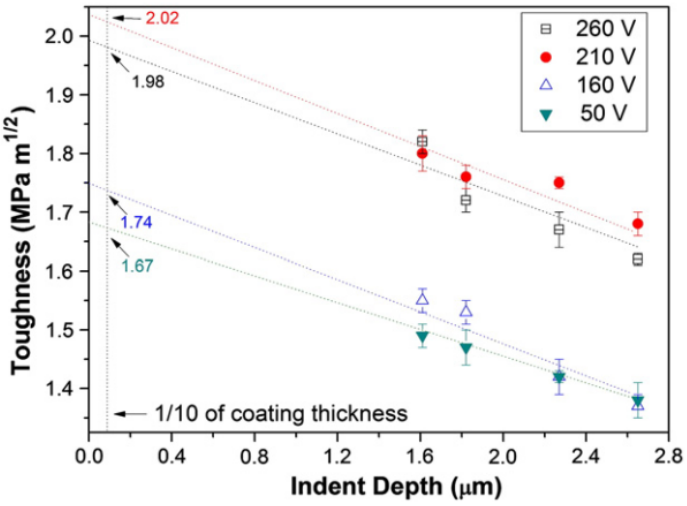


Figure 2.8: Toughness evolution with the indent depth at different bias voltage of CrAlN.

4. **Optimization of coating architecture**

   (a) *Gradient toughening.* The idea behind this strategy is to create a gradient structure or composition gradient. Usually a relatively soft layer with very good adhesion is deposited first on the substrate, followed by harder layer or layers with an increasing gradient in hardness. An example of this type of structure is shown in figure 2.9.

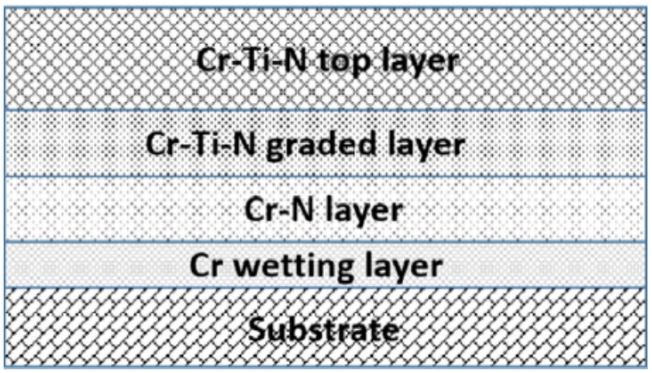


Figure 2.9: Sketch of the microstructure of the graded Cr/CrN/CrTiN coating [34].

The properties, reported by Sharear *et al.*, for Cr/CrN/CrTiN indicate a hardness similar to that of the single layer coatings, but with improved adhesion and toughness [34]. Similar properties were reported by Lin *et al.* for Cr/CrN/CrAlN [35]. Another example of a compositionally graded coating is shown in figure 2.10, where the hardness and crack propagation resistance of CrAlSiN coatings are compared with two coatings with different Si contents, but a graded Si composition. "CrAlSiN-GH" represents the graded coating with the highest Si content and "CrAlSiN-GL", the one with the lowest. Both of them are compared against CrAlSiN coatings with a similar Si content at the surface, but with a uniform Si composition through the coating thickness, demonstrating that the graded coatings present better overall properties than the uniform ones [36].

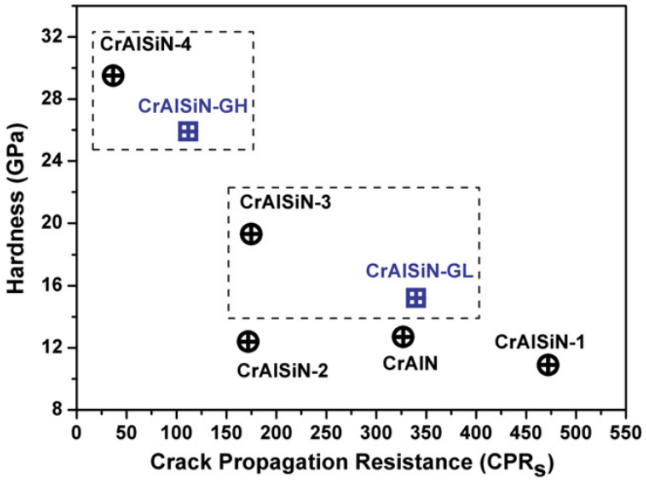


Figure 2.10: Hardness and crack propagation resistance of CrAlSiN coatings [36].

(b) *Multilayer structure.* As aforementioned, by modifying the architecture of a coating its properties can be greatly enhanced. By the introduction of layers with different properties new fracture mechanisms are introduced, for instance, cracks are deflected at the interfaces of the different layers.

As it can be seen in figure 2.11, the multilayer system formed by layers of $SiO_x$ and TiN follows the rule of mixtures for the elastic modulus. However, the toughness of the coating is substantially increased by increasing the number of layers [37].

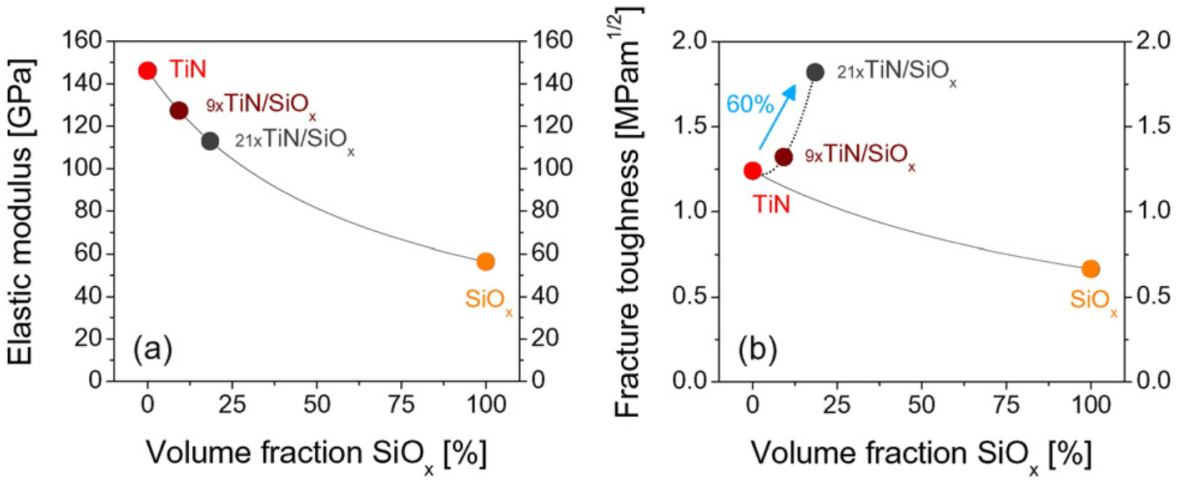


Figure 2.11: Comparison of the evolution of the hardness (a) and toughness (b) of a single layer and multilayer coating formed by $SiO_x$ and TiN [37].

The toughness of a multilayer coating depends on the number and thickness of the layers. By reducing the thickness of the layers the so-called superlattice effect, previously explained, might also increase the toughness of the coating, in addition to its hardness, as can be seen in figure 2.12 [38].

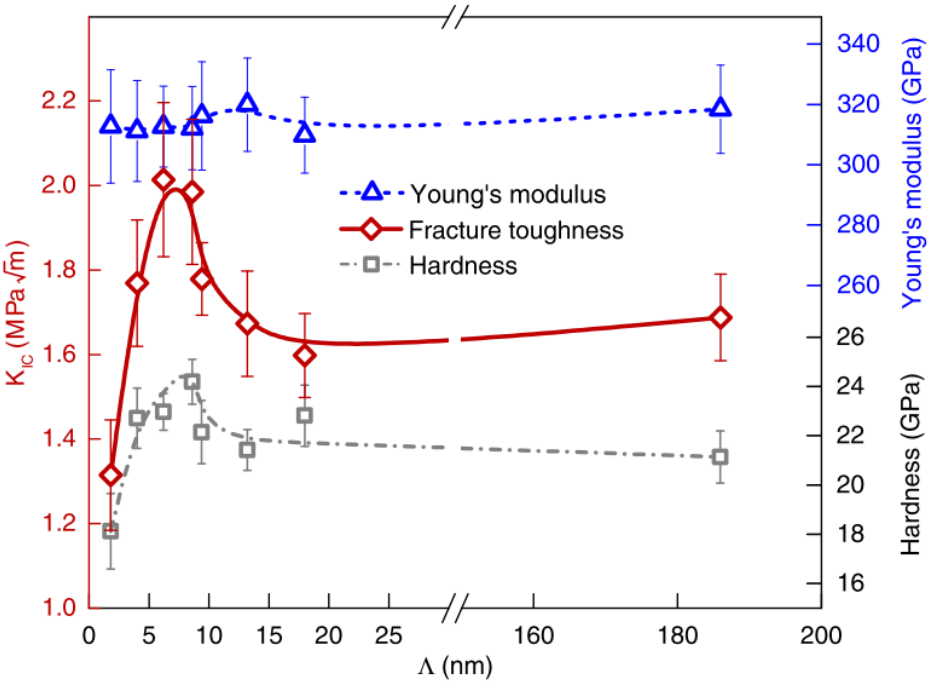


Figure 2.12: Evolution of the hardness, toughness and elastic modulus with the bilayer period Λ for TiN/CrN [38].

## 2.4 Review of the microstructural changes and hardening/toughening mechanisms

A review of different microstructural changes that can be made to the coatings seeking to imitate nacre and the mechanisms that have proven to be effective to improve the hardness and the toughness of the coatings was done. However, not all mechanisms can be applied at the same time or they are not viable to perform well at high temperature. The viability of these mechanisms at high temperature is evaluated next.

Residual compressive stresses, which are inherent to coatings produced by reactive sputtering, might be an effective strategy to increase hardness and toughness. However, they are unlikely to be effective at elevated temperature because the residual stresses are expected to be relieved through recovery and recrystallization processes. Other mechanisms such as the introduction of carbon nanotubes are very difficult to produce and be effective, or phase transformation toughening being very material specific, were discarded as well.

As seen before, a mechanism that has proven to be effective at room temperature is the formation of a nanocomposite structure with either a ceramic or metallic matrix. This microstructure presents an amorphous structure and has proven to be quite effective improving the coating's toughness, without compromising or even increasing its hardness. Another effective strategy to improve hardness and toughness simultaneously might be the formation of multilayer structures. Although the improvement of the properties might depend on the system as well as the optimal layer thickness of each compound, it seems to be the most promising mechanism to enhance the mechanical properties of these coatings. Gradient structures and compositional gradients, either in combination with a multilayer structure or by themselves also seem to be an effective mechanism to increase toughness, although in this case with a small reduction in the hardness. For these two strategies, the thermal stability of the coating is crucial for these mechanisms to be operative at elevated temperature.

It must be noted that amorphous-like in this case refers to a phase that does not appear in X-ray diffraction or electron diffraction patterns. This nomenclature will be used during this study. However, this phase is likely a crystalline phase of only a few atomic layers thick. This has been observed for TiSiN [39] and is expected for Ni due to the high tendency of metals to form crystalline phases unless the phase is highly defective or contaminated with N.

Regarding the mechanical behavior at high temperature, obtaining a nanocomposite structure might be one of the most promising strategies to increase the mechanical properties of hard coatings. Thus, the objective of this part of the work has been the use a high throughput methodology for the development of this type of microstructure. The material system of choice has been Ti-N-Ni, which at the right composition has the potential of forming a nanostructure consisting of TiN nanocrystals surrounded by a Ni rich tissue. As explained by Li *et al.* and Musil *et al.* (for ZrN), this microstructure makes TiN/Ni present a higher hardness than pure TiN [2, 40]. However, the effectiveness of this microstructure at high temperatures has not been analyzed yet.

When it comes to multilayer coatings there are many variables in their design and thus, different mechanisms that can be used to modify their behavior, specially when combining materials of different nature. In this case, to increase the toughness while keeping a high

hardness, even at high temperature, focus is put in two main aspects that have a strong effect on these mechanical properties: number of interfaces and ductility of metallic layers. At low bilayer periods the hardness of the coatings increases reaching a maximum when the bilayer thickness is around 10nm [41, 42]. It is believed that this increase is caused by the superlattice effect, mentioned before [38]. Having a high interface volume can also lead to an increase of the toughness by other mechanisms as well. Even if the metallic phase cannot behave plastically due to the reduced thickness, the microstructure is refined becoming harder and cracks may deflect at the interfaces dissipating energy. When increasing the thickness of the metallic phase, the layers are formed by a few grains and thus becomes more ductile and therefore, toughness will increase but keeping a relatively high hardness due to the increment caused by the Hall-Petch effect. A further increment of the metallic layer thickness allows dislocation generation by Frank-Read sources and hence increase the ductility of the coating [23]. How fracture and deformation mechanisms of ceramic-metal multilayer coatings evolve as the metallic layer increases have been previously studied by Wiecinski *et al.* [43].

Therefore, after this assessment of the different mechanisms with a more promising behavior at high temperature, the project will be divided in two parts. The first is the analysis of the nanocomposite structure by using a high throughput methodology and samples with a continuous analysis suitable for it. The second consists on the characterization of coatings that combined result in a nacre-like microstructure as shown in figure 2.13. By combining the mechanisms selected at different scales, this analysis seeks to improve the toughness of the coatings without a substantial reduction of hardness. For this purpose, the hard phase in the multilayer systems in this study are TiN, to be used as reference, and TiN/Ni, with the optimum composition found in the previous analysis, and pure Ni as the ductile phase. This study would show what is the effect of a tissue phase on the crack propagation and the Ni layers in a system with no residual phases such as TiNi intermetallics or Ni nitrides.

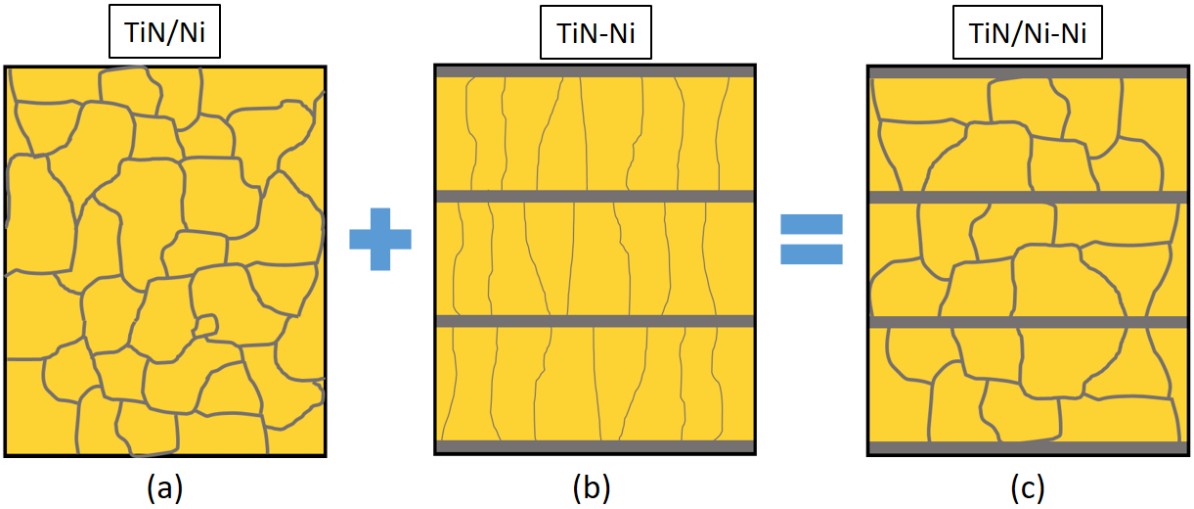


Figure 2.13: Sketch of the hierarchical build up of nacre-like microstructure using a nanocomposite and a multilayer microstructure. (a) Nanocomposite structure, (b) multilayer structure and (c) combination of both microstructures.

# Chapter 3

# Experimental procedure

The coatings were prepared by using a homemade magnetron sputtering system. In order to characterize them, different analysis techniques were used. Thickness was measured using optical profilometry by masking part of the substrate before the deposition. X-ray diffraction (XRD) was used to analyze the phases that appear in the coating as well as electron diffraction (ED) in conjuction with transmission electron microscopy. For the compositional analysis, energy dispersive spectroscopy (EDS) was used to estimate the composition of the coatings and correlate the mechanical properties with it. In addition to EDS, Rutherford backscattered spectroscopy (RBS) was used at selected spots to check the stoichiometry of the TiN and compare the results with EDS. Hardness and toughness were measured by nanoindentation and micropillar splitting respectively, and TEM and high resolution electron microscopy (HREM) were used to analyze the microstructure of the coatings.

## 3.1 Sample preparation procedure

### 3.1.1 Compositional gradient coatings

A homemade reactive magnetron sputtering system was used for the synthesis of the coatings. The coatings were deposited on a long strip of a Si <100> single-crystal, using Ti (99.95%) and Ni (99.9%) targets. The atmosphere in the chamber was composed of argon with 15% of

nitrogen, and the pressure during deposition was set to 0.66 Pa, after reaching a base pressure of around $3.4 \cdot 10^{-4}$ Pa. The substrate temperature was set to 400°C and the samples were cooled down in a nitrogen atmosphere after deposition, in order to avoid oxidation of the coatings. During deposition a bias of negative 100V was applied to the substrate.

Suitable samples for testing the high throughput approach must present a compositional gradient along them. To achieve this, the holder was maintained stationary during deposition, so that the composition along the thin-film varied, as a function of the distance to each target. The Ti and Ni targets were operated at a DC power of 150W and 12W, respectively. The power applied was calibrated so that the deposition rates met a 10:1 ratio at the center of the holder.

As shown in figure 3.1, the Si strip was placed in such a way that one edge of the substrate was directly facing the Ti target, while the other was approximately at the center of the substrate holder. The distance between the targets and the centre of the holder was 4" ( 10cm), which was the holder's diameter as well. The target's diameter was 2" ( 5cm) and the thickness of the Ti target was 0.25" ( 0.63cm). The thickness of the Ni target, however, was 0.125" ( 0.32cm) and was placed on top of a Cu plate with the same dimensions to prevent overheating.

Not rotating the holder, however, leads to thickness uniformity and temperature homogeneity issues that should be taken into account. As a mean to avoid big thermal gradients and to reduce the thermal stresses caused by them, a 45 min thermal stabilization stage was carried out, followed by the deposition of a pure Ti interlayer. During this process, the holder was rotated at 30 rpm, so that the uniformity of the interlayer was preserved. Without this step, it was found that the coating on part of the substrate broke and formed a non-uniform coating with a very rough surface in which the substrate could still be seen.

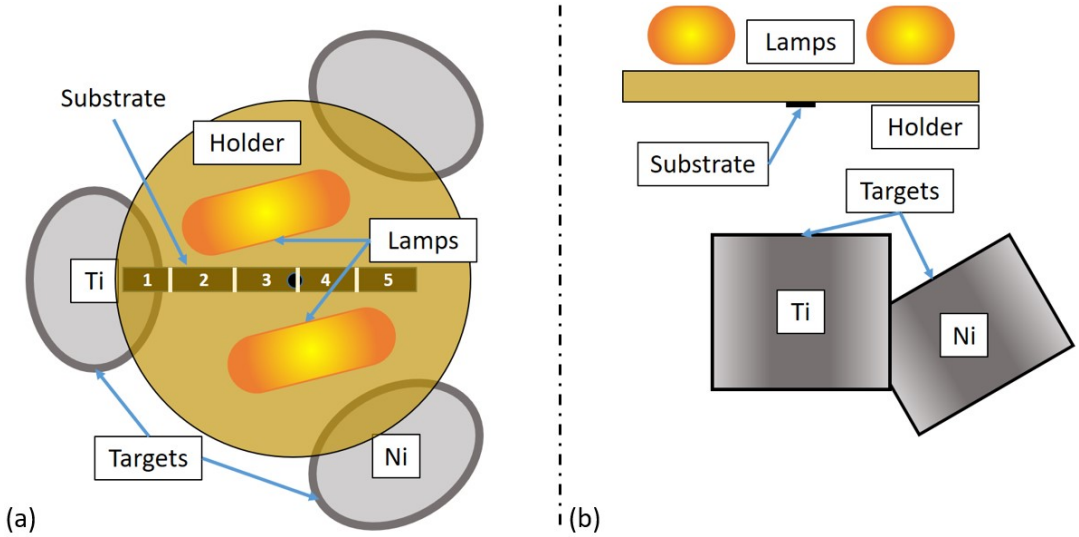


Figure 3.1: Schematic representation of the deposition set up. (a) top view and (b) front view.

In order to test the thermal stability of the coatings, some samples were heat treated in vacuum at 500°C and 800°C, after deposition. The temperature of the oven increase at a rate of 5°C /min and it was kept at that temperature for another two hours and the samples were let to be cooled down in the oven.

### 3.1.2 Multilayer samples

As means to be able to compare the effectiveness of the different microstructures in the mechanical properties, separately and combined, a coating for each of the steps in the hierarchical build-up towards the nacre-like microstructure was deposited. The deposition of the multilayer coatings was controlled by the use of shutters on top of the targets. There are two different systems which were analyzed. The first one seeks to analyze the effect of the amount of interlayers and the second one the effect of Ni plasticity within the coating. The thickness of the Ni layers was chosen following Koehler's criteria for a metal to be able to deform plastically [23]. The value chosen is above the critical thickness at which the material is able to generate dislocations and thus, present a ductile behavior. The following thin films were designed for this purpose:

Table 3.1: Summary of the second set of samples

| | TiN & TiN(10)Ni [nm] | Ni [nm] |
|---|---|---|
| Monolithic | - | - |
| Interfaces | 10 | 2 |
| plasticity | 100 | 60 |

The naming of the coatings is as follows. For the monolithic coatings is TiN for pure titanium nitride and TiN(x)Ni where x is the amount of Ni found to perform best during the analysis of the gradient coatings. The multilayer coatings are named with the thickness of the hard phase followed by its composition, a dash and the thickness of the Ni layer. For instance, 10TiN-2Ni refers to the multilayer coating with layers of 10nm of TiN with Ni layers of 2nm.

For this set of samples the same magnetron sputtering system was used, however in this case the coatings have an homogeneous composition and three different substrates were used, 4140 steel, M2 steel and Si <100> single-crystal. The same targets were used but the power applied to them was increased to 300W for Ti and the Ni power was adjusted to obtain the optimal TiN/Ni composition obtained from the analysis of the samples with compositional gradient at 23W. The increase in the power of the targets sought to have higher deposition rates in order to have thicker coatings, specially relevant for high temperature tests. Due to the depletion of the Ti target, a new one with the same purity was used. The atmosphere of the chamber was also varied, the base and deposition pressure were kept the same but the nitrogen content was increased to 25% and later to 30% for the new target. The bias applied to the substrate was increased to negative 120V.

Due to the use of metallic substrates, a few changes were made to the deposition process. First, the substrates were sputter cleaned for 2 minutes in order to remove the oxide layer that forms on steels and second the interlayer thickness was increased in order to reduce the residual stresses that may come from thermal expansion and deposition of thicker coatings. Last, the thermal stabilization time was increased to 1.5h.

However, during the production of the samples with Ni thickness of 60nm, the samples presented delamination after the first Ni layer, as it can be seen in figure 3.2. In addition to

the loss of adhesion, the samples deposited at 400°C showed cavities formed at this moment and thus, increasing the roughness of the coating. This could be a result of the increasing roughness of the Ni layers since its recrystallization process starts at around 250-300°C [44].

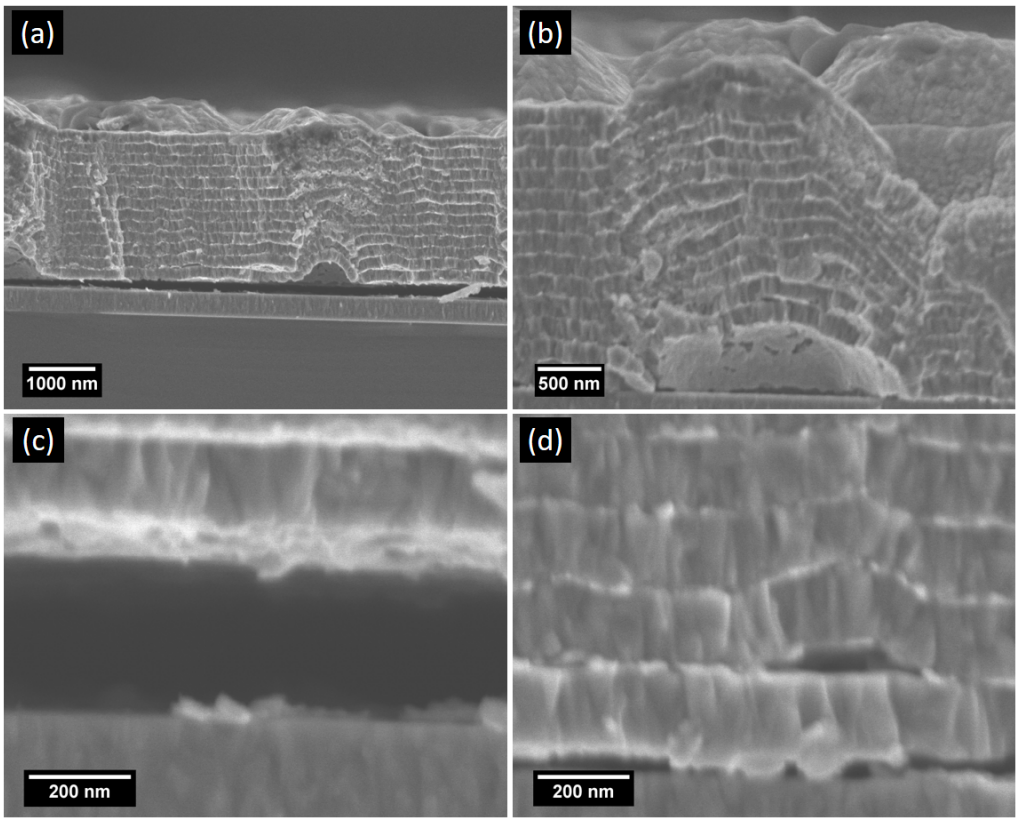


Figure 3.2: Cross section SEM micrographs of TiN(100nm)-Ni(20nm) deposited at 400°C on Si

In order to avoid this delamination, the substrate temperature was lowered down to 150°C over several depositions. At this temperature the resulting coatings were smooth, however, the delamination problem was not completely prevented, as it can be seen in figure 3.3.

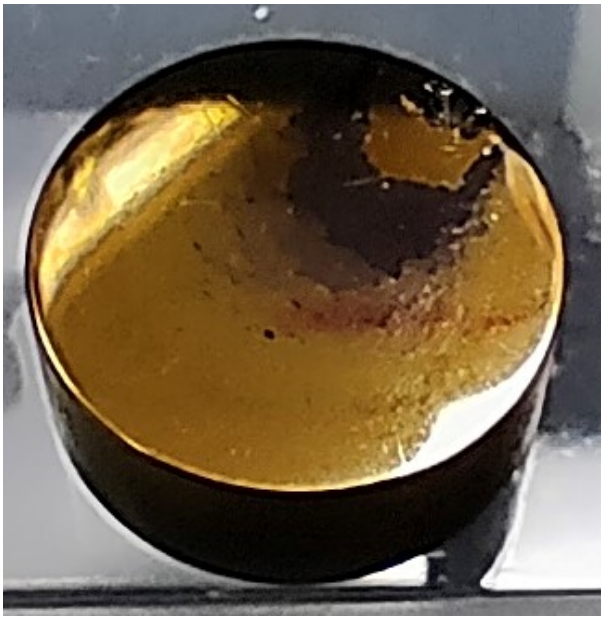

Figure 3.3: Photo of TiN(100nm)-Ni(20nm) deposited at 200°C on M2 steel

Using other methods such as using TiN(10)Ni which presented lower residual stresses or smoother compositional transitions between the layers. Using those modifications the delamination during the deposition process was delayed, obtaining coatings with more layers, but never avoiding it.

Given that the results obtained by changing the temperature of the substrate did not solve the delamination issues, other parameters were changed. Since the adhesion problems seemed to come from the Ni layers, those were modified to reduced their roughness and increase the adhesion. The parameter that was decided to be changed was the bias used during the depsotion of Ni.

To analyze its effect of the deposition rate and the crystallinity of the Ni layer, 4 coatings of pure Ni were deposited using 0, -120V, -500V and -1000V at 200°C. The rest of the parameters used were the same as for monolithic coatings. However, for -1000V a higher target power (40W instead of 23W) was used due to resputtering phenomena reducing dramatically the deposition of Ni and even redepositing of elements from the substrate holder. The latter was used for the Ni layers of 60nm in the final samples and the effect on the surface morphology and microstructure will be further analyzed.

As it can be seen in figure 3.4, when using 0V Ni(111) peak appears displaced towards higher angles. When increasing the bias to -120V, the peak shifts towards the reference presenting a higher intensity as well which could indicate a larger grain size thus, increasing of the roughness causing adhesion issues. A further increase in the bias to -1000V, reduces the intensity of the peak the Ni coating presents the minimum and its position is closer to the reference. Due to the limited thickness of these samples, the signal intensity of the peaks was low and no other peaks besides the (111) orientation were observed.

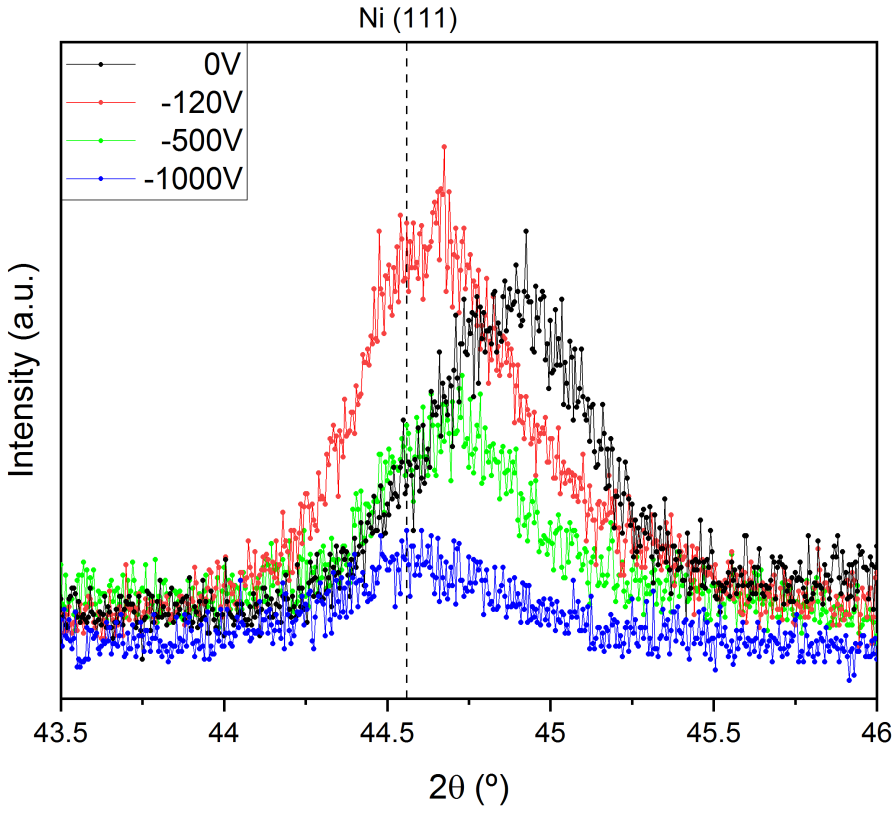


Figure 3.4: XRD patterns of pure Ni as a function of substrate bias

When the bias is increased, the surface temperature also gets higher due to the higher energy of the atoms arriving to the substrate. Thus, when applying -120V to the substrate Ni is able to release part of the stresses and present a more crystalline microstructure compared to the unbiased Ni coating. Increasing the bias to -500V makes the ion bombarding of the Ni atoms start removing part of the material and redeposit. This resputtering process provides the

coating with a finer microstructure despite having a higher surface temperature. For -1000V, this effect is more dominant producing a coating microstructure with less crystallinity with a smaller grain size. In addition, since the peak is closer to the reference it suggests that under these conditions Ni presents almost no residual stresses, which may have improved the adhesion of the layers.

When depositing the 60nm Ni layers, the use a bias of -1000V improved the adhesion enough, so that Si<100> substrates presented no delamination, but still did not present an homogeneous surface. In order to enhance the mobility of the atoms the substrate temperature was increased to 400°C which, in addition to the higher bias applied to the substrate during the deposition of Ni layers, made the coating present a smooth and uniform surface. Nevertheless, the metallic substrates still presented some delamination and rough surface.

Since the power of the Ni target and the bias had to be changed between layers, a 15s gap in which both shutters were closed was added so those parameters could be changed with minimal impact on the coating.

Since parts of the samples are to be tested at 500°C, they were subjected to the same heat treatment than the previous set of samples. However, after the heat treatment, part of the samples were delaminated so the high temperature tests were performed in as-deposited samples. Additionally, the heat treated results were obtained from heat treated M2 steel substrates which mostly survived the heat treatment.

## 3.2 Phase, chemical and residual stresses characterization

Prior to the deposition of the coatings, an area of the substrate was masked in order to determine the coating thickness using optical profilometry. Phase analysis of the samples was performed by XRD using a PANanlytical P4311 diffractometer in $\theta/2\theta$ configuration using Cu K$\alpha$. The gradient samples were divided into sections of around 5x5 mm, thus their composition cannot be considered uniform due to it changing gradually. This was considered a good balance between resolution and signal intensity, since further reduction of the measure-

ment area would imply a reduction of the intensity of the XRD spectra to correctly perform a qualitative assessment of the evolution of the microstructure.

Different characterization techniques with high spacial resolution were used to map the elemental composition, structure and mechanical properties of the TiN/Ni coating as a function of position along the substrate. However, some of these techniques are more suitable for high throughput analysis despite having very high lateral resolution. Therefore, some of them were used to continuously characterize the coating while other were used at selected measurement areas. This has to be taken into account when comparing the results from the different characterization techniques and their interpretation.

Elemental mapping was performed by high throughput EDS used to estimate the amount of Ni/Ti ratio present in the coatings and to determine the composition profile along the samples with high resolution (interaction volume of the order of microns) and high precision (typically $\pm 1\%$). Ni was assumed to be correctly estimated and the combination of Ti and N to be TiN. The Si signal was assumed to be coming from the substrate since it was fairly constant for all measurements. These measurements were taken with a step size of 1mm along the edge of the substrate. Nevertheless, the accuracy of EDS to detect light elements is low, so non-RBS measurements were carried out at selected positions to determine the N content. This characterization technique allows the determination of the stoichiometry of the TiN phase and validate the EDS results. These measurements were performed using a He beam with a spot size of 1.5mm at an energy of 3.7 MeV. This energy was selected to increase the accuracy in the nitrogen signal since at this energy the cross-section for N is non-Rutherford [45]. RBS measurements were performed in a high vacuum chamber which is connected to a 2MV Tandetron accelerator located at the Centro Nacional de Aceleradores (CNA/CSIC) in Seville [46]. The backscattered ions were detected by a standard Si-barrier detector located at an angle of 165°. The atomic percentage of Ti and N in the coatings was estimated by comparing experimental and simulated spectra. For the simulations, the commercial computer code SIMNRA was used [47].

Coatings deposited by plasma processes inherently present residual stresses, which are of importance since they can improve the hardness of the coating but compromise the adhesion of the coating to the substrate. These stresses are the result of the interaction between deposition conditions, being especially important ion bombardment effects and substrate temperature, microstructure evolution and constraints imposed by the substrate. For instance, the difference in thermal expansion and lattice mismatch. Traditional methods for the measurement of residual stresses like XRD diffraction or substrate curvature lack the spacial resolution to be applied to coatings with compositional gradients. Therefore, a methodology that allows their measurement with a higher spatial resolution is needed in order to evaluate them reliably. Korsunsky *et al.* proposed a new methodology based on FIB milling and digital image correlation which is suitable for this purpose [48]. By combining the incremental milling of annular trenches and tracking previously formed markers using a high resolution scanning electron microscope (SEM) imaging, the strain relief upon material removal can be measured [48]. Firstly, a Pt layer was deposited over selected areas of the coating to later mill a pattern of holes by FIB to serve as markers, as shown in figure 3.5 (a). Secondly, annular trenches with diameter and depth equal to the coating thickness, were milled to ensure total strain relief of the coating and allow the determination of the average residual stress in each location, as shown in figure 3.5 (b). Due to the small thickness of the coating and thus, of the annular trenches, it was critical to obtain images free of artifacts, such as drift, and the maximum resolution that can compromise the tracking of the surface pattern. For this purpose, prior to the Pt deposition and a gold layer was sputtered to improve the surface conductivity and minimize drift during the acquisition process of the image. The resolution of the SEM images taken was 6114x4415 pixels and the dwell time was set to $1\mu$s, using three different scanning rotations of 0, 45 and 90 degrees with respect to the marker pattern. This way the strain relief was determined using three directions, ensuring that the measurements were made in the scanning direction of the electron beam, which is less susceptible to drift artifacts. Finally, it was assumed that the stress state of the residual stresses is biaxial, so that using the average strain relief, $\overline{\epsilon}$ was calculated from:

$$\sigma_R = \frac{E}{1-\nu} \cdot \overline{\epsilon} \tag{3.1}$$

Where E is the elastic modulus and $\nu$ is the Poisson ratio of the coatings.

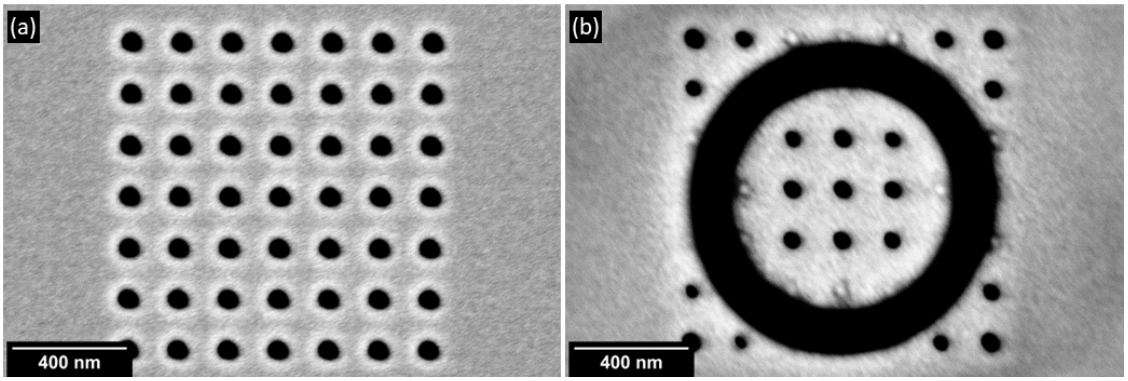


Figure 3.5: Residual stress measurement steps, (a) pattern mill and (b) micropillar mill

For the samples prepared with homogeneous composition the residual stresses were calculated by measuring the deflection of the Si substrates using Stoney's equation (3.2)[49]. This method could not be used for the samples with compositional gradient due to its insufficient lateral resolution.

$$\sigma_R = \frac{E_s}{6(1-\nu_s)} \frac{h_s^2}{h_f} \left( \frac{1}{R} - \frac{1}{R_0} \right) \tag{3.2}$$

where $E_s$, $\nu_s$ and $h_s$ are the elastic modulus, Poisson's ratio of Si and the substrate's thickness respectively. $h_f$ is the thickness of the coating, $R$ and $R_0$ are the curvature of the sample after and before the deposition of the coating. The curvature was measured using optical profilometry. In order to correctly compare the samples, the substrates used were prepared to have the same dimensions only presenting a very small variation in their thickness ranging from 0.5 to 0.53mm.

## 3.3 Mechanical characterization

Nanoindentation experiments were performed using a Hysitron TriboIndenter TI950 with a Berkovich diamond tip. Since the thickness is expected to vary along the sample since the holder is not rotating, nanoindentation tests were performed in depth control in order to avoid any effect from the substrate even at low-thickness regions. A hardness profile was carried out along the sample using 70nm deep indentations and then correlated to the composition profile. Hardness and elastic modulus were calculated using the Pharr *et al.* method assuming a Poisson ratio for the coating of $\nu$=0.24 [50].

For nanoindentation mapping, around 150 matrices of four measurements with a spacing of 325$\mu$m between them were performed for as-deposited samples. For heat treated samples the amount of matrices and spacing was similar but matrices of five nanoindentations were used instead. This change was implemented due to an increase in the variability in the results likely coming from a morphology change of the surface during the heat treatment. Since the indentation depth is very low, this affects greatly the results. Samples heat treated at 800°C were not mechanically tested for the same reason.

Toughness was obtained following the procedure described by Sebastiani *et al.* by micropillar splitting tests and equation 3.3 [51]. The micro-pillars were indented using the same equipment as for nanoindentation but using a cubic corner diamond tip instead. The aspect ratio (height to diameter ratio) of the micropillars should be around unity. They were machined by focused ion beam (FIB) milling using a FIB-FEGSEM dual-beam microscope (Helios NanoLab 600i). An example of one of the milled micro-pillars is presented in figure 3.6. They were milled at different positions along the sample so that toughness could also be mapped despite the lower lateral resolution.

$$K_{IC} = \gamma \cdot \frac{P_{max}}{R^{3/2}} \tag{3.3}$$

where $K_{IC}$ is the fracture toughness, $\gamma$ is a dimensionless coefficient that depends on the elasto-plastic properties of the coating and the indenter geoemetry, $P_{max}$ is the maximum indentation load, and $R$ is the pillar's radius. Gamma values were extrapolated from the $E/H$ ratio of the coatings from values calculated for a cube-corner indenter by Ghidelli *et al.* [52] in the range 0.6-0.83. Groups of four pillars were milled at twelve spots along the sample and the spacing between micropillars was 10$\mu$m as shown in figure 3.6. Despite having a variable coating thickness along the sample, the same milling parameters were used for all the micropillars, with a target height close to the average thickness of the coating.

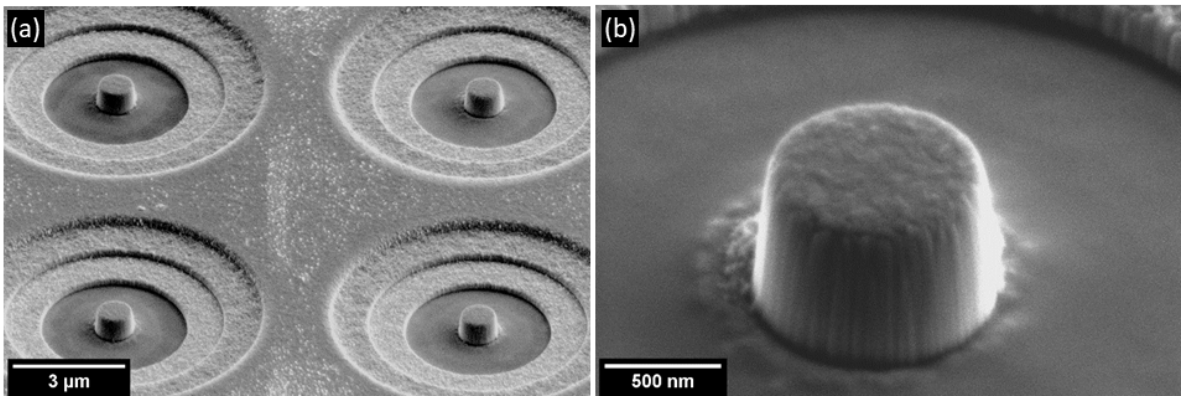


Figure 3.6: (a) Grid of micropillar milled for splitting experiments; (b) High magnification image from one of the pillars from the gradient samples

Additionally, in order to test how the Ni content affects the mechanical properties of TiN at high temperature, nanoindentation tests were carried out at 200, 350 and 500°C using the same equipment and tip but a different stage. Pillar splitting tests were not performed at these temperatures due to the lack of reliability to make the nanoindentations at the center of the pillars because of their small radius. Additionally, only measurements at two specific locations from the samples with compositional gradient were tested, being pure TiN and TiN/Ni at the optimum composition after the heat treatment at 500°C. These nanoindentation tests were performed using a different load function, which for these experiments was load controlled using 3000$\mu$N as maximum load in an atmosphere mostly composed of Ar.

For the second set of samples, the microstructure of TiN and TiN/Ni was analyzed by high resolution transmission electron microscopy (HRTEM) and scanning transmission electron microscopy (STEM) using a Thermosfisher Talos F200X microscope. Samples were prepared by the lift-out technique using a FIB-FEGSEM dual-beam microscope (helios Nanolab 600i).

## 3.4 Evolution of depositions

In order to obtain samples to be analyzed by the characterization techniques described before, preliminary coatings were deposited and analyzed with different objectives to reach that point. The evolution of deposition parameters used for depositions and the addition of steps is

presented in table 3.2 as well as characterization techniques used on them, some observations and the problems they had. Parameters that are not mentioned in the table have been constant throughout all depositions and were mentioned before in section 3.1.

Table 3.2: Evolution of depositions

| Dep. | Objective | Changes | Analysis techniques | Observations | Problems |
|---|---|---|---|---|---|
| 1 | Calibration of TiN deposition rate | - | XRD | -Low deposition rate | -Low target power (50W)<br>-Low deposition time (30min) |
| 2 | Calibration of TiN deposition rate | -Increase target power to 100W<br>-Increase deposition time to 60min | XRD | -Presence of $TiN_xO_y$<br>-Low deposition rate | -Presence of Oxygen<br>-Low target power (100W) |
| 3 | Calibration of TiN deposition rate and avoid oxides | -Cooldown in $N_2$ atmosphere<br>-Increase target power to 150W | -XRD | -No presence of oxides<br>-Adequate deposition rate | - |
| 4 | Calibration of Ni deposition rate | - | - | -Excesive deposition rate | -High target power (30W) |
| 5 | Calibration of Ni deposition rate | -Lower target power to 10W | - | -Adequate deposition rate | - |

| | | | | | |
|---|---|---|---|---|---|
| 6 | Deposition of samples with gradient of Ni | -Increase deposition time to 90min | -XRD<br>-Nanoindentation<br>-RBS*<br>-TEM/HRTEM<br>-EDS<br>-XPS | -Rough surface but continuous coating close to Ti target<br>-Too high Ni content<br>-Bad pin disposition<br>-Nanocomposite structure obtained<br>-Presence of Si at surface for low Ni regions | -Low TiN depostion rate |
| 7 | Calibration of TiN deposition rate with TiN target and pulse power | -Pulse DC power | - | -Low deposition rate | -Low target power (100W, T=2.5$\mu$s, F=100Hz) |
| 8 | Calibration of TiN deposition rate with TiN target and pulse power | -Increase target power to 150W | - | -Low deposition rate | -Low target power<br>-Discarded |
| 9 | Preparation of pure TiN sample | - | - | -Low deposition rate | -Low Ar tank pressure |
| 10 | Deposition of samples with gradient of Ni | -Different pin distribution | - | -Samples are very grey | -Low deposition rate of TiN<br>-Forgot bias<br>-Change of power supply system |

| | | | | | |
|---|---|---|---|---|---|
| 11 | Preparation of pure TiN sample | -Increase of Ar tank pressure | - | - | -Detachement was observed after some time |
| 12 | Deposition of samples with gradient of Ni | -Change of power supply system | - | -Non-uniform coating close to Ti target | -Assumption of isolated event |
| 13 | Deposition of samples with gradient of Ni | - | EDS | -Right EDS range<br>-Rough surface close to Ti target | - |
| 14 | Recalibration of TiN deposition rate | -No rotation<br>-Low deposition time(30min) | - | -No rough surface appears | - |
| 15 | Recalibration of Ni deposition rate | -No rotation<br>-Low deposition time (30min) | - | -Low deposition rate, hard to measure | - |
| 16 | Deposition of samples with gradient of Ni | -Low deposition time (30min) | EDS | -No surface roughness appears<br>-A bit low %Ni range | -Low deposition rate |
| 17 | Deposition of samples with gradient of Ni | -Increase Ni target power to 12W<br>-Low deposition time (30min) | EDS | -Oxygen contamination<br>-Good %Ni range | - |
| 18 | Deposition of samples with gradient of Ni | - | EDS | -Debonded coating close to Ti target<br>-Good %Ni range | -Assumption of isolated event |

| | | | | | |
|---|---|---|---|---|---|
| 19 | Deposition of samples with gradient of Ni | - | - | -Debonded coating close to Ti target | - |
| 20 | Deposition of samples with gradient of Ni | -Adoption of longer thermal stabilization<br>-Introduction of interlayer | EDS | -Uniform coating<br>-Good %Ni target | - |
| 21 | Deposition of samples with gradient of Ni | -Rotation for interlayer deposition | -EDS<br>-XRD<br>-Nanoindentation map<br>-Micropillar splitting<br>Residual strains | -Uniform coating | - |
| 22 | Deposition of samples with gradient of Ni | - | -Heat treatment<br>-EDS<br>-XRD<br>-Nanoindentation map<br>-Micropillar splitting<br>Residual strains | -Detached coating after treatment close to Ti target | - |
| 23 \| 25 | Deposition of samples with gradient of Ni | -Increase deposition time to 100min | -Heat treatment trials | - | - |

| | | | | | |
|---|---|---|---|---|---|
| 26 | Calibration of TiN deposition rate | -Pulse DC power<br>-30 min deposition<br>-substrate rotation | - | -Low deposition rate<br>-No TiN obtained | -Low power<br>(100W, f=100Hz, T=2.5s) |
| 27 | Calibration of TiN deposition rate with 2 targets | -2 Ti targets<br>-Pulse DC and DC current<br>-15 min deposition | - | -No TiN obtained | -Not enough Nitrogen<br>(150W, f=100Hz<br>T=2.5s & 150W DC) |
| 28 | Calibration of TiN deposition rate and increase Nitrogen content | -20% Nitrogen | - | -No TiN obtained | -Not enough Nitrogen |
| 29 | Calibration of TiN deposition rate and increase Nitrogen content | -No bias | - | -No TiN obtained | -Not enough Nitrogen |
| 30 | Calibration of TiN deposition rate and increase Nitrogen content | -Bias of 100V | - | -No TiN obtained | -Not enough Nitrogen |
| 31 | Preparation of TiN sample for analysis | -75 min deposition | -EDS<br>-XRD<br>-Nanoindentation | -Low TiN stoichiometry | -Not enough Nitrogen |

| | | | | | |
|---|---|---|---|---|---|
| 32 | Preparation of TiN sample for analysis | -Ti 6Al 4V substrate | -EDS<br>-XRD<br>-Nanoindentation | -Low TiN stoichiometry | -Not enough Nitrogen |
| 33 | Calibration of TiN Deposition rate | -One Ti target with 300W DC<br>-25% Nitrogen<br>-15 min deposition<br>-Bias of-120V | - | -Low thickness for analysis | - |
| 34 | Preparation of TiN sample for analysis | -75 min deposition | -EDS<br>-XRD<br>-Substrate deflection | - | - |
| 35 | Calibration of Ni Deposition rate | -30 min deposition | - | - | - |
| 36 \| 38 | Calibration of TiN(10)Ni deposition rate and composition | - | -EDS | -wrong amount of Ni | -wrong Ni power |
| 39 | Preparation of TiN(10)Ni-Ni multilayer sample | - | - | -arc due to dirt | -clean shutter regularly |
| 40 \| 41 | Calibration of TiN deposition rate | -New Ti target<br>-30% Nitrogen | - | -Low Nitrogen content | - |

| | | | | | |
|---|---|---|---|---|---|
| 42 | Preparation of TiN(10)Ni-Ni multilayer sample ($\lambda = 20$nm) | - | -EDS<br>-XRD<br>-Cross section SEM | -Too much Ni<br>- High multilayer period | - Reduce layer deposition time |
| 43 | Preparation of TiN(10)Ni-Ni multilayer sample ($\lambda = 20$nm) | - | -EDS<br>-XRD<br>-Cross section SEM | - Wrong Ni content for period | - Reduce Ni layer deposition time |
| 44 | Preparation of TiN(10)Ni-Ni multilayer sample ($\lambda = 12$nm) | - | -EDS<br>-XRD<br>-Cross section SEM | - Wrong Ni content for period | - Reduce Ni layer deposition time |
| 45 | Preparation of TiN(10)Ni sample | - | -EDS | - | - |
| 46 | Preparation of TiN(10)Ni final sample | -M2 and 4140 steel substrates for final samples<br>-Sputter clean<br>-Deposition time aiming thickness $1.5\mu$m<br>-Thicker interlayer | -EDS | - Low Ni content | -Low Ni power |
| 47 | Preparation of TiN final sample | - | -EDS<br>-XRD | - | - |
| 48 | Preparation of TiN(10)Ni final sample | -Higher Ni target power | -EDS<br>-XRD | - Adhesion problems on M2 Steel | -High residual stresses |

| | | | | | |
|---|---|---|---|---|---|
| 49 | Preparation of TiN(10)Ni final sample | -Lower sputter clean energy<br>-Thicker interlayer | -EDS<br>-XRD | - Adhesion problems on M2 Steel | -High residual stresses |
| 50 | Preparation of TiN(10)Ni final sample | -Thicker interlayer | -EDS<br>-XRD | - Too much Ni content | - High Ni power |
| 51 | Calibration of TiN deposition rate | -New Ti target<br>- Higher Nitrogen partial pressure | - | - | - |
| 52 \| 54 | Calibration of TiN(10)Ni deposition rate and composition | - | -EDS | -wrong amount of Ni | -wrong Ni power |
| 55 56 | Calibration of TiN-Ni multilayer | - | -EDS | - | - |
| 57 | Final sample of TiN(10)Ni | - | -EDS | - | - |
| 58 \| 60 | Samples of TiN-Ni with Ni=2nm | - | -EDS | - | - |
| 61 | Final sample of TiN(10)Ni-Ni | - | -EDS | - | - |
| 62 \| 71 | Deposition of TiN-Ni with Ni=20nm | -Deposition time<br>-Addition of TiN gradient to interlayer<br>-Substrate temperature | - | -Poor adhesion (specially for metallic substrates)<br>-Rough surface | -Roughness of Ni layers reduces adhesion |

| | | | | | |
|---|---|---|---|---|---|
| 72 \| 77 | Calibration of TiN and Ni deposition rates | - | -EDS | - | - |
| 78 \| 79 | Deposition of TiN-Ni multilayer | - | -EDS<br>-HRSEM cross-section | -Low adhesion | - Increase substrate temperature to 250°C |
| 80 \| 98 | Deposition of TiN-Ni multilayer | -Variation of thickness of Ni layer | -EDS<br>-HRSEM cross-section | -Low adhesion | - Lower substrate temperature to 150°C |
| 99 \| 106 | Deposition of Ni | -Variation of Ni Bias at 200°C | - | - | - |
| 107 \| 109 | Deposition of TiN-Ni multilayer with Ni=60nm | -Use of -1000V for Ni deposition | -Better surface finish | - | - |
| 110 \| 111 | Deposition of TiN-Ni multilayer with Ni=60nm | -Substrate temperature set to 400°c | -Homogeneous surface | - | - |

*RBS results were received after deposition 19.

**After deposition 35, magnets were taken out and cleaned. A deposition rate drop was experience afterwards.

# Chapter 4

# Investigation of nanocomposite composition gradient of TiN/Ni: Results, analysis and discussion

The first part of the investigation was conducted to study the effect of Ni content in the co-sputtered TiN/Ni coatings. A high throughout method was utilized to obtain TiN/Ni coatings with a gradient in the Ni content. A long strip of a Si substrate was mounted in the holder, as shown in figure 4.1, where the label "Ti" marks the location of the Ti target and "C", the center of the holder. In order to proceed with the characterization of the coatings as a function of Ni content, the long Si strip was cut into sections of around 2cm in length, as presented in figure 4.1. TiN/Ni 1 refers to the location that was closer to the Ti target, while TiN/Ni 5 corresponds to the location that was further away.

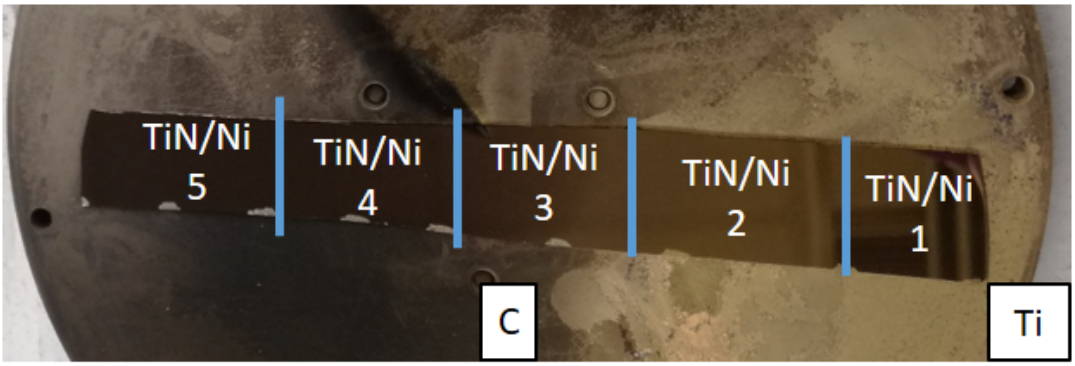


Figure 4.1: Sectioning of the samples and placement on the holder (C indicated the center of the substrate holder and Ti the location of the Ti target)

As described in the previous chapter, some of the coatings were heat treated to test their thermal stability. Upon annealing at 500°C, parts of the coating detached from the substrate, close to locations TiN/Ni-1 and TiN/Ni-2, as shown in figure 4.2. Heat treated samples at 800°C presented complete delamination up to TiN/Ni-3 section.

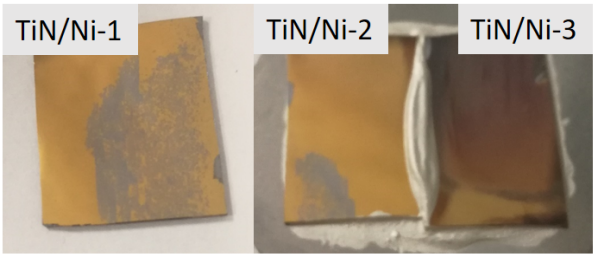


Figure 4.2: TiN/Ni-1 to TiN/Ni-3 heat treated samples

## 4.1 Thickness distribution and elemental composition

The thickness profile as a function of position in the substrate holder for different deposition runs is shown in figure 4.3, where the origin represents the location in front of the Ti target. The thickness was relatively uniform presenting some variation on the sides of the center of the holder This thickness profile is a consequence of not rotating the holder, during the deposition and the variation of the distance to the targets.

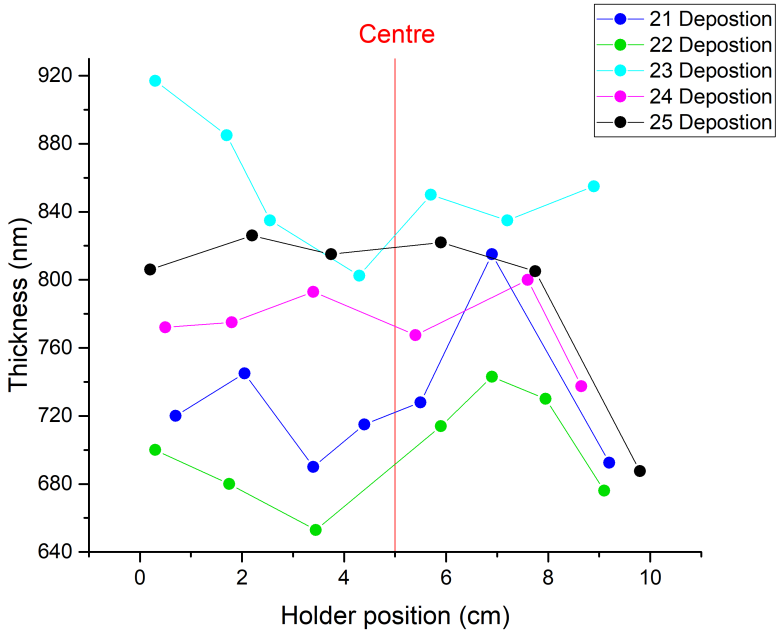


Figure 4.3: Thickness profile from samples with gradient composition

Figure 4.4 plots the Ni% as a function of position along the Si strip, measured by EDS. The origin represents the location in front of the Ti target. The EDS measurements showed that the adopted strategy was successful on producing a coating with a wide range of Ni content. Light elements, like N, are not accurately quantified by EDS but the Ni at.% can give a good estimation of the TiN/Ni ratio present in the coatings. Nevertheless, it should be born in mind that the Ni content obtained by EDS may be slightly underestimated due to the presence of the pure Ti interlayer. Although it is very thin compared to the overall thickness of the coating, it is composed solely of Ti and thus, the calculated Ni content might be slightly lower than its actual content.

As aforementioned, the samples were divided into five sections to facilitate the characterization, the ranges of the sample tested as-deposited are delimited by vertical dash lines in figure 4.4. The strips present a Ni content varying from 0 to 20% at. which is an ideal range to evaluate the impact of the addition of Ni on the mechanical behavior of TiN coatings since they contain practically pure TiN that can be used as reference. It has to be kept in mind that even small amounts of alloying elements can have an impact on the mechanical properties due to grain refinement effects [53]. Finally, it is worth noticing that the bulk of the variation in

Ni content occurs in locations close to the center of the substrate holder, while the variations on the edges of the long strip are smaller. In fact, TiN/Ni-1 and TiN/Ni-5 were not mapped with a high spacial resolution, because the Ni content did not varied as much as in the rest of the sections. In order to later correlate the Ni content with the mechanical properties, the composition profile versus distance was fit with a "BiDoseResp" function using the software Origin.

Additionally, a composition analysis by RBS was performed in preliminary samples in order to analyze the stoichiometry of the TiN phase and validate the EDS results since EDS measurements present certain uncertainty when it comes to N. RBS is a elemental composition characterization technique in which the spectra obtained needs to be compared with a simulation to know which elements are present and their amount. For some coatings, in which a single composition does not fit correctly the spectra, different layers with variations in the amount of each elements are added. The results shown in table 4.1 correspond to measurement areas in TiN/Ni-1, TiN/Ni-2 and TiN/Ni-4 , where it can be seen that the Ti:N ratio was very close to unity for pure TiN. When getting closer to the substrate, Si starts to appear and the Ti quickly drops while N slowly decreases. In order to analyze the stoichiometry and compare the results from both techniques, only the most superficial and thicker layer is taken into account.

Table 4.1: RBS composition from TiN and TiN/Ni preliminary samples

| | | [Ti] (at.%) | [N] (at.%) | [Ni] (at.%) | [Si] (at.%) | Thickness ($10^{15}$ at/cm$^2$) |
|---|---|---|---|---|---|---|
| Pure TiN | Layer 1 (Surface) | 47 | 53 | 0 | 0 | 5900 |
| | Layer 2 | 31 | 49 | 0 | 20 | 500 |
| | Layer 3 | 12 | 43 | 0 | 45 | 400 |
| TiN/Ni-2 (Max H) | Layer 1 (Surface) | 45 | 46 | 7 | 2 | 2700 |
| | Layer 2 | 40 | 46 | 7 | 8 | 900 |
| | Layer 3 | 37 | 26 | 5 | 32 | 800 |
| | Layer 4 | 25 | 17 | 5 | 53 | 800 |
| | Layer 5 | 3 | 16 | 4 | 77 | 200 |
| TiN/Ni-4 | Layer 1 (Surface) | 35 | 48 | 17 | 0 | 8400 |

Comparing the results from both techniques it was observed that EDS overestimates the amount of Ni in the coating as presented in figure 4.4. Nevertheless, this may slightly differ in samples with interlayer prepared afterwards.

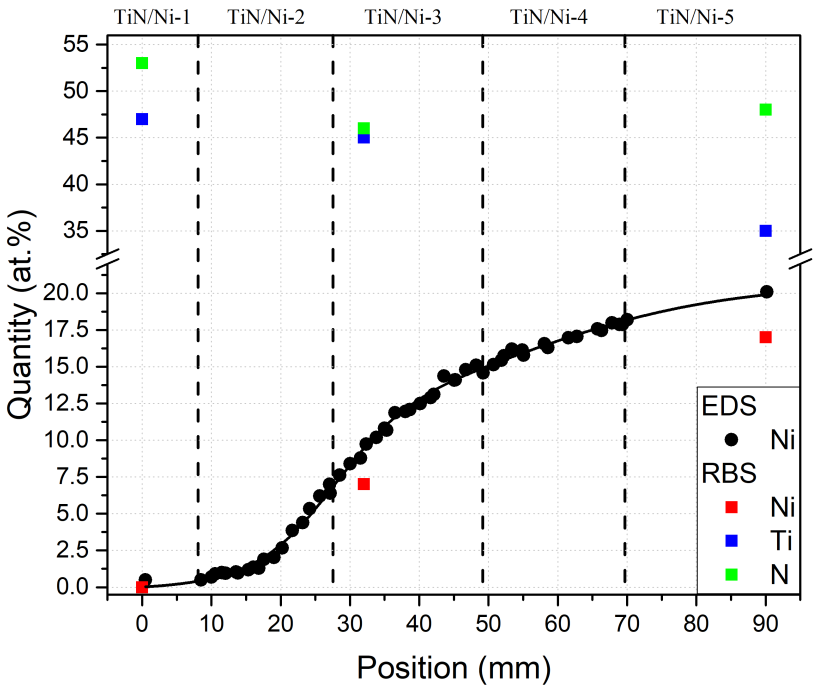


Figure 4.4: Elemental composition determined along the sample according to EDS and RBS results

Finally, a deeper analysis of the stoichimetry of $\delta$-TiN at the different positions show that N was relatively constant at 50±4 at.%, and thus the (Ti+Ni)/N ratio being 1±0.1. On the pure TiN side, the Ti/N ratio was 0.9 which is almost stoichiometric with an excess of N, being $TiN_{1.1}$. $\delta$-$TiN_x$ is stable over a wide range of stoichiometries, with x varying from 0.6 to 1.2 [54] depending on the deposition conditions. The confirmation by RBS results is that $\delta$-TiN is stoichiometric upto section TiN/Ni-3. However, the fact that the (Ti+Ni)/N ratio remains constant along the entire sample means that either Ni is dissolved within the TiN lattice or, segregated into a Ni rich phase that contains a large amount of N dissolved. At equilibrium conditions TiN and Ni are immiscible and Ni is not a strong nitride former [1], but since sputtering conditions are far from equilibrium, co-depositing Ti and Ni in a N containing atmosphere, it may result in any atomic mixture in the coating.

## 4.2 X-ray diffraction analysis

Figure 4.5 presents the XRD spectra from the different TiN/Ni sections, in the as-deposited state and after heat treatment. It is important to mention that the Ni composition varies along each section, as previously shown in figure 4.4. TiN/Ni-1, the section with the least Ni content, shows a preferred (111) growth orientation, since the TiN (200) peak barely appears. Interestingly, as the Ni content increases to 7 at.%, the preferred growth orientation switches to (200) for TiN/Ni-2. The effect is even more pronounced for Ti/Ni-3, with a Ni content between 7 and 15 at.%. Another obvious observation is the shift of the TiN peaks to larger diffraction angles, which implies a reduction in the interplanar spacing as Ni is incorporated into the coating. However, for TiN/Ni-4 and TiN/Ni-5, with Ni contents larger than 15 at.%, the preferred growth orientation is lost and the TiN(111) and TiN(200) peaks are even more strongly shifted to larger diffraction angles. Finally, the width of the diffraction peaks increases as the Ni content increases, which might be linked to a smaller TiN grain size or a lower degree of crystallinity. Interestingly, no signal of any peak corresponding to Ni was found in the as-deposited coatings. However, upon annealing, TiN/Ni-3 is the first one that shows a distinct diffraction peak corresponding to Ni(111), that increases in intensity for higher Ni contents. Additionally, the TiN diffraction peaks are even more shifted to higher diffraction angles, specially for intermediate Ni contents (TiN-Ni-2 and TiN/Ni-3).

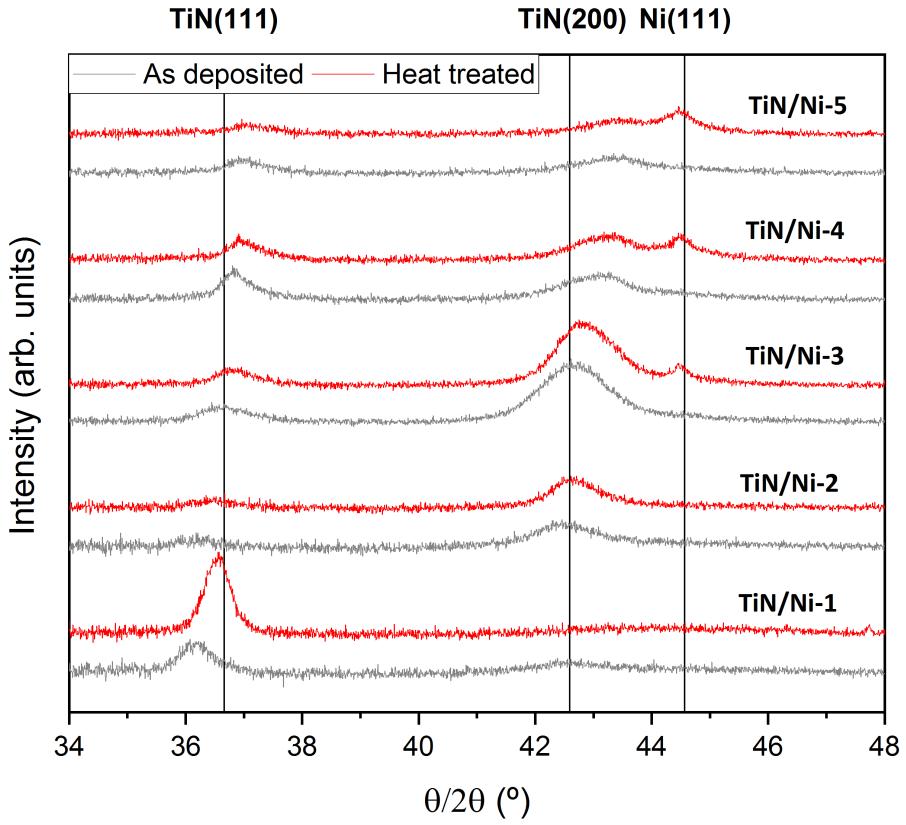


Figure 4.5: XRD patterns of the divided TiN/Ni samples

The XRD spectra offer a number of interesting observations. First, as Ni is incorporated in the coating, there is a clear transition from a TiN(111) to a TiN(200) preferential growth orientation. The TiN(200) preferred growth orientation is not linked to the presence of residual stresses according to Abadias, but favoured by renucleation events, that might be triggered by the presence of Ni [55]. Nevertheless, a further increase in the amount of Ni in the sample, seems to increase the intensity of the TiN(111) peak again, so this might only take place for a narrow interval of Ni content.

Second, the diffraction peaks shift to larger diffraction angles as the Ni content increases, implying a smaller out-of-plane lattice parameter. This might be linked to either a reduction in the TiN lattice parameter or to the presence of residual stresses. The latter might explain the coating debonding that took place in the samples deposited without a Ti interlayer, as presented in figure 4.6. However, one would expect the residual stresses to partially relieve

upon annealing. On the contrary, after the heat treatment, the peaks suffer a small shift towards even higher angles for TiN/Ni-2 to TiN/Ni-5, which means that there must be another factor affecting their position. Moreover, according to previous observations, an increase in the Ni content reduces the presence of residual stresses in the coatings [55]. Therefore, the most likely explanation is that the incorporation of Ni induces a reduction in the TiN lattice parameter, presumably due to a defective Ti sub-lattice, which would also explain the large increase in the width of the diffraction peaks with Ni content. Thus, Ni for this sections could be segregated presenting a highly overstoichimetric TiN or either be dissolved in the TiN lattice. Since the ionic radius of $Ni^{3+}$ (0.056nm) [56] is smaller than that of $Ti^{3+}$ (0.0075nm)[57], the substitution would lead to a smaller lattice parameter, which has been previously observed for $TiN/Ni/Si_3N_4$ composite coatings [58]. This conclusion also agrees with the RBS results in table 4.1 that imply a large increase in the Ti/N ratio as the Ni content increases for TiN/Ni-4.

Figure 4.6: Preliminary deposition sample showing a debonded region

Finally, the fact that the Ni(111) peak only appears upon annealing for TiN/Ni-3 implies that no crystalline Ni is present in the coatings in the as-deposited state, which agrees with previous work for which Ni did not appear in the XRD spectra up to 22.5% [2, 59]. This might support the idea that either the Ni is amorphous-like in the as-deposited state or that it is dissolve in the TiN lattice or both, as mentioned before. The former seems a likely explanation because upon annealing at 500°C, a distinct Ni(111) appears for Ni contents higher than 7 at.%. Additionally, it is possible that some Ni segregates out of the TiN lattice during annealing [1], which would explain the additional shift in the diffraction peaks upon annealing.

It is important to remind that the Ni content is not constant for the sections analyzed in figure 4.5, especially in the case of TiN/Ni-2 and TiN/Ni-3, for which the range of Ni content was relatively large, as shown in figure 4.4. This might affect the XRD analysis, as the microstructure is not expected to be entirely homogeneous within each section. According to the literature, when the growth conditions are such that a nanocomposite structure is obtained, the preferred growth orientation is TiN(200) [2]. Based on the evolution of the XRD spectra, if such microstructure has been attained at any location of the coating, this should be at a location in between TiN/Ni-2 and TiN/Ni-3.

## 4.3 Residual stresses

The values of the strain relief measured by image correlation upon FIB material removal in different locations of the coatings is presented in figure 4.7. The measurements were carried out in three different in-plane orientations, as explained in the experimental section. The results confirmed a state of biaxial residual stress, as expected for thin films, as the strain relief estimated in the three different orientations provide the same value, within experimental error. The almost pure as-deposited TiN was subjected to a state of large compressive residual strains, of the order of 1.5%. Incorporation of 4 at.% Ni produced a dramatic reduction of compressive residual strains down to 0.25%, while the residual strains were found negligible or even slightly tensile for Ni contents larger than 10 at.%.

To evaluate if the heat treatment had any strain relief effects measurements at 0 and 3.5 at.% Ni were repeated since higher Ni contents presented almost none residual strains in the as-deposited state. As shown in figure 4.7, the residual strains were reduced drastically, going from around 1.5% compressive strain to 0.25% for pure TiN and around 0.25% to almost none for 3.5 at.% Ni. The high residual strains present in the as-deposited TiN-rich coatings explains their tendency to delaminate upon annealing. These residual strains were seen to relieve despite the relatively low annealing temperature. Another plausible reason that may contribute to the reduction of residual strains upon annealing is a partial segregation of Ni from the lattice to the grain boundaries.

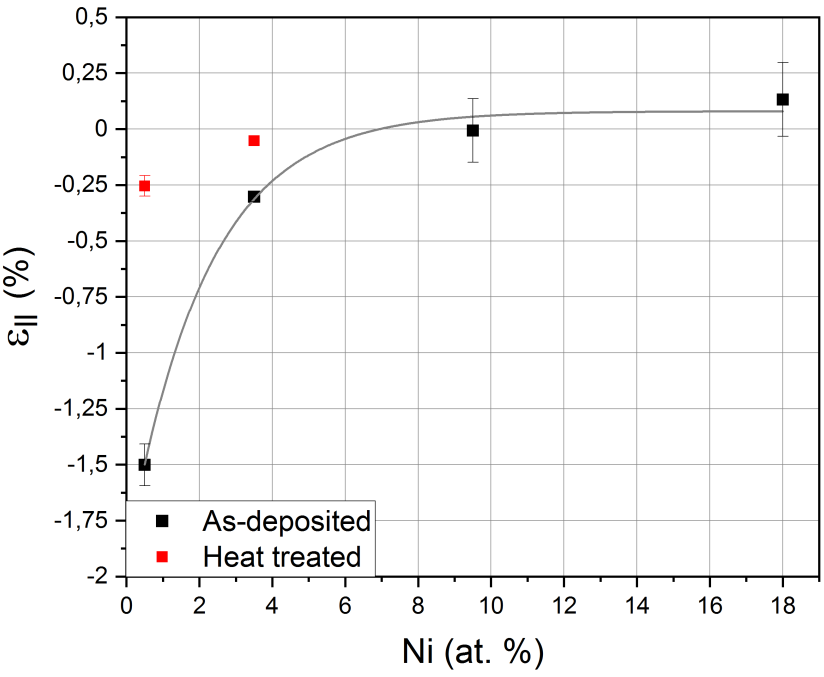


Figure 4.7: Residual strain evolution with at.% Ni

## 4.4 Mechanical properties

Figure 4.8 shows the evolution of the (a) elastic modulus, (b) hardness and (c) fracture toughness as a function of Ni content for as-deposited coatings and upon annealing at 500°C. For the as deposited coatings the elastic modulus was fairly constant, and of the order of 340 GPa, up to Ni contents of the order of 13 at.% and dropped quickly for higher Ni contents. Hardness and fracture toughness, however, increased slightly with Ni content, from 25 GPa and 4.3 MPa $m^{1/2}$, respectively, for very small Ni contents, up to 32 GPa and 4.8 MPa $m^{1/2}$, respectively, for Ni contents of the order of 9.5 at.% Ni. After this peak, both hardness and fracture toughness decreased slowly with a further increase in Ni content, to drop strongly, together with the elastic modulus, for Ni contents larger than 13 at.%.

Upon annealing the elastic modulus was not constant anymore but dropped slowly with Ni content, up to Ni contents of the order of 13 at.%. Nevertheless, the hardness trend changes from the as-deposited coatings. Values at very low Ni contents are similar but a bit lower and then, at around 4 at.% Ni there is a drop in hardness that recovers afterwards as more Ni is incorporated into the coating reaching 28 GPa at around 10 at.%. This drop could be related to a reduction in the residual stresses and a further segregation of Ni to the grain boundaries due to the heat treatment. For Ni contents higher than 13 at.%, the scatter of the elastic modulus measurements increased dramatically and the hardness dropped strongly. The increase in the scatter of the data might be related to the increase in surface roughness during the heat treatment for high Ni contents, as was shown in TiN/Ni-3 in figure 4.2. Fracture toughness of the heat treated samples showed a bigger scatter than the as-deposited ones, especially at higher Ni contents, but still followed the same trend and presented similar values.

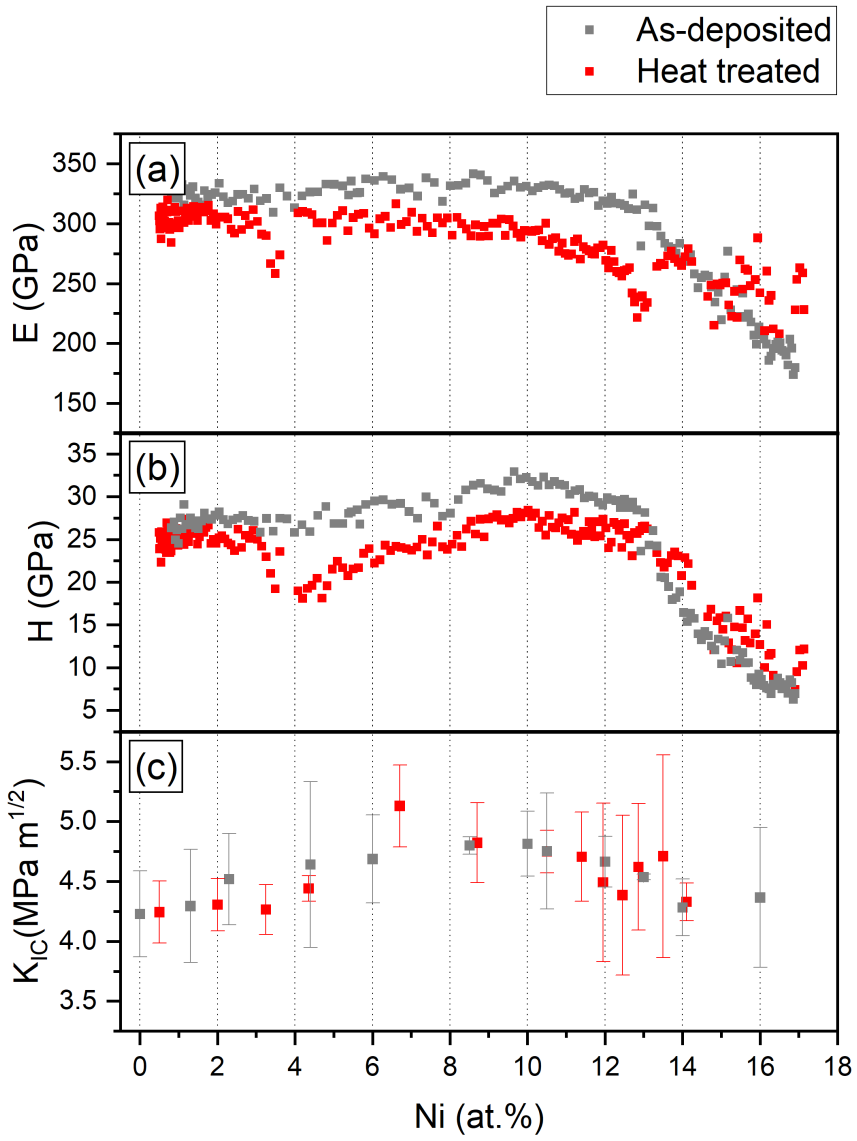


Figure 4.8: (a) Elastic modulus, (b) hardness and (c) fracture toughness comparison between as deposited and heat treated states as a function of Ni% content.

There are a number of observations that are worth discussing in more detail. First, the elastic modulus is fairly constant up to 13 at.% Ni. The elastic modulus mainly depends on the stiffness of the atomic bonds and it is relatively insensitive to the microstructure of the coatings. The fact that it remains constant enforces the idea that the TiN phase remains fully stoichiometric up to Ni contents of the order of 13 at.% Ni, and that the Ni either incorporates into the TiN lattice without strong changes in the strength of its bonds, or it segregated, forms a thin amorphous-like tissue around the TiN grains, without modifying the elastic properties of

the coatings. For higher Ni contents, however, Ni induces large changes in the stoichiometry of the TiN phase (see table 4.1), inducing a defective Ti sub-lattice, and probably the presence of a large amount of amorphous-like Ni, that affects strongly the elastic modulus of the coatings, and even their integrity and thermal stability, as observed during annealing.

Second, despite the constant elastic modulus up to 13 at.% Ni, the hardness and fracture toughness of the as-deposited coatings, initially increase with Ni content up to 9.5 at.% Ni, to decrease again for higher Ni contents. The maximum is located in the TiN/Ni-3 section, that according to the XRD patterns in figure 4.5, has a strong TiN(200) preferred growth orientation, with the TiN peaks slightly shifted to larger diffraction angles and with no evidence of crystalline Ni. These observations are compatible with the formation of a nanocomposite structure, where TiN grains, slightly enriched in Ni, are expected to be surrounded by a thin tissue of an amorphous-like Ni phase, which blocks the movement of dislocations and increases the resistance to deformation [2]. Final confirmation of this hypothesis can only come from TEM analysis of the microstructure of the coatings. However, the fact that, after the maximum, the hardness and fracture toughness decrease with Ni content might be related to the thickening of the Ni tissue phase, which is weaker than the TiN phase.

The hypothesis is also consistent with the changes observed in the coatings upon annealing. The XRD patterns suggest the segregation of Ni out of the TiN phase and its crystallization with temperature, which can explain the slight reduction in hardness.

Figure 4.9 presents the hardness evolution with the heat treatment and different testing temperatures showed in a timely progression as the the tests were performed on the sample. As shown in this figure, TiN presents a negligible hardness change after the heat treatment and then maintains that hardness up to 200°C at around 27 GPa to afterwards start dropping at 350°C and plummets at 500°C to around 8 GPa. After the tests, hardness seems to recover once the sample was cooled down to room temperature. This trend is similar in the case of the elastic modulus, however, the elastic modulus after the tests is much higher than the initial one.

TiN/Ni with approximately 10 at.% Ni was also tested under these conditions since this composition presented the highest hardness and toughness at room temperature. The hardness of the coating decreases after the heat treatment as it was seen during mapping in figure 4.8, but remains relatively constant for high temperature tests even up to 350°C going down to around 25 GPa at this temperature. Nevertheless, at 500°C the hardness drops to 10GPa which is similar to pure TiN. The elastic modulus also decreased after the heat treatment, however, it seems to increase slightly after the tests were performed.

Since the atmosphere is not completely inert some oxides may have formed during the time the samples were kept at elevated temperatures. This, in combination of the small depth of the indentation tests, may have had a great impact on the elastic modulus. For both coatings, the effect of the oxide layer can be noticed as the elastic modulus greatly increased after testing compared to the initial value.

It should be mentioned that no chemical analysis was performed on these samples after testing, but a visual inspection revealed a change in color. Since the samples had been subjected to heat treatment prior to testing no other microstructural changes are expected and thus, the only plausible hypothesis is the formation of oxides on the surface of the coatings.

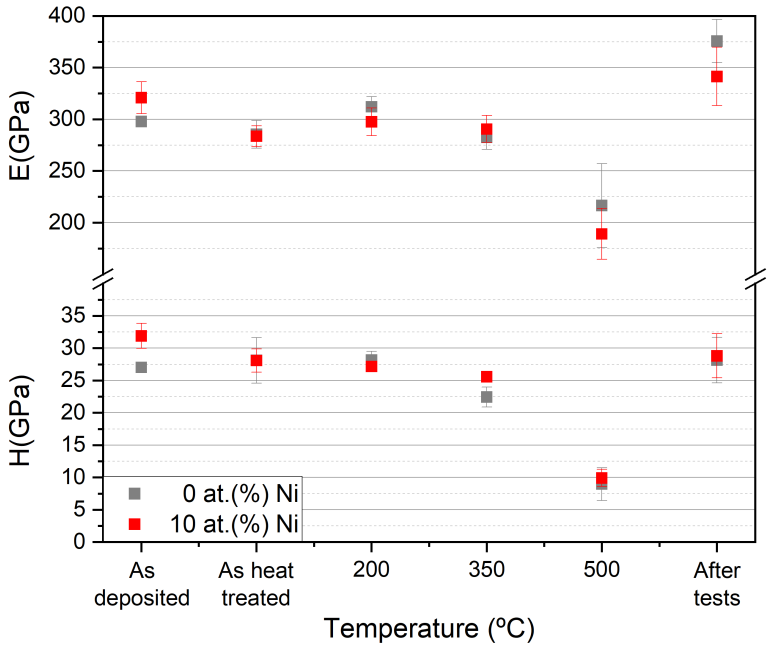


Figure 4.9: Hardness of the coating as a function of temperature

## 4.5 Microstructural analysis

The microstructure of the TiN-Ni coatings as a function of Ni content was analyzed using TEM. Lamellae transparent to electrons were extracted by FIB from three different locations corresponding to pure TiN, TiN(10)Ni at.% Ni and TiN(18)Ni at.% Ni. A bright-field (BF) image of the cross-section of the TiN coating is shown in figure 4.10(a). The Ti interlayer can be clearly seen, as well as the development of a columnar grain microstructure. The columnar grains have an inverted pyramidal shape which is compatible with the zone T in the Thornton's coating morphology diagram [60]. The columnar widths increase with coating thickness and reach tens of nanometers at the coating surface. The ED patterns in figure 4.10(b) and (c), taken from the areas indicated by the dashed circles, show a transition from more diffuse $\delta$-TiN (111) and (200) diffraction rings to distinct diffraction spots with coating thickness, as a consequence of the increasing width of the columnar grains. Figure 4.10(d) shows a HREM image, demonstrating a dense microstructure, without the presence of voids or pores along the columnar boundaries. This is the typical microstructure found in sputtered dense stoichiometric TiN coatings that develops as a result of competitive growth between different grain orientations in kinematically limited conditions [55], which leads to the (111) preferred orientation determined by XRD (figure 4.5).

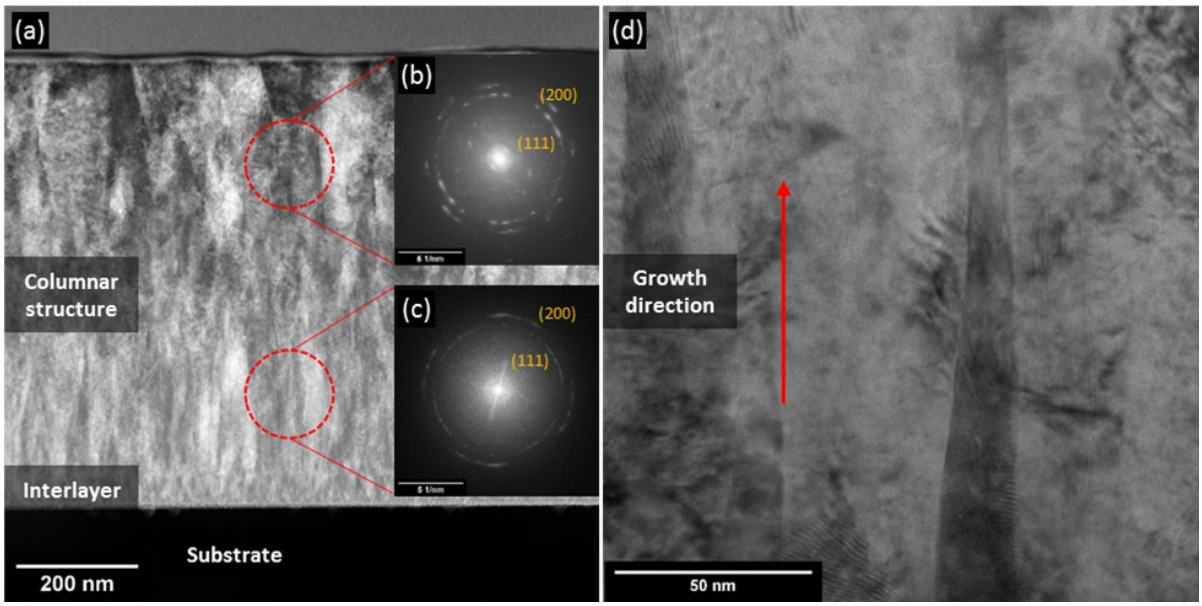


Figure 4.10: Images of the cross-section of the coating on the TiN position: (a) BF TEM;(b) and (c) DPs taken at the locations marked; (d)HREM showing the dense columnar boundaries

The TEM images corresponding to TiN/Ni with a nickel content of around 10 at.% (with maximum for which hardness and fracture toughness) are depicted in figure 4.11. The BF image in figure 4.11(a) shows that the columnar structure gradually transforms into a nanocrystalline structure with equiaxed grains as the coating grows. This transition is likely due to the time required during sputter deposition to reach the prescribed 15% partial pressure of $N_2$ after opening the $N_2$ flow or to complete the formation of a TiN rich layer on the surface of the Ti target, because it was observed that the nitrogen content increased gradually with coating's thickness during the transition, as shown in the elemental profiles obtained by EDS of figure 4.11(d). The nanocrystalline nature is clearly demonstrated by the diffuse diffraction rings in the ED pattern taken in this region (4.11(b)) and by the HREM image in figure 4.11(e), which shows equiaxed crystalline nanograins, with sizes of the order of 5–10 nm. Finally, the presence of an amorphous-like phase in some regions is also evident in figure 4.11(e), as pointed by the arrows. High-angle annular dark field (HAADF) images (figure 4.11(f)) and the corresponding Ni elemental map (figure 4.11(g)) in the same region also demonstrate that Ni is strongly segregated in this area, forming small domains that are evenly distributed at the same scale than the nanograin size without any evident directionality. TEM is a projection technique and the images show the superposition of several nanograins along the thickness of the TEM foil, which is of the order of 100 nm. Therefore, it is impossible to determine the chemical composition and spatial distribution of the crystalline and amorphous-like regions, but the TEM observations, combined with the XRD results (4.5), are compatible with what is expected for a nanocomposite microstructure formed by crystalline nanograins of $\delta$-TiN, preferably oriented in the (200) growth orientation, embedded in a Ni rich amorphous-like phase.

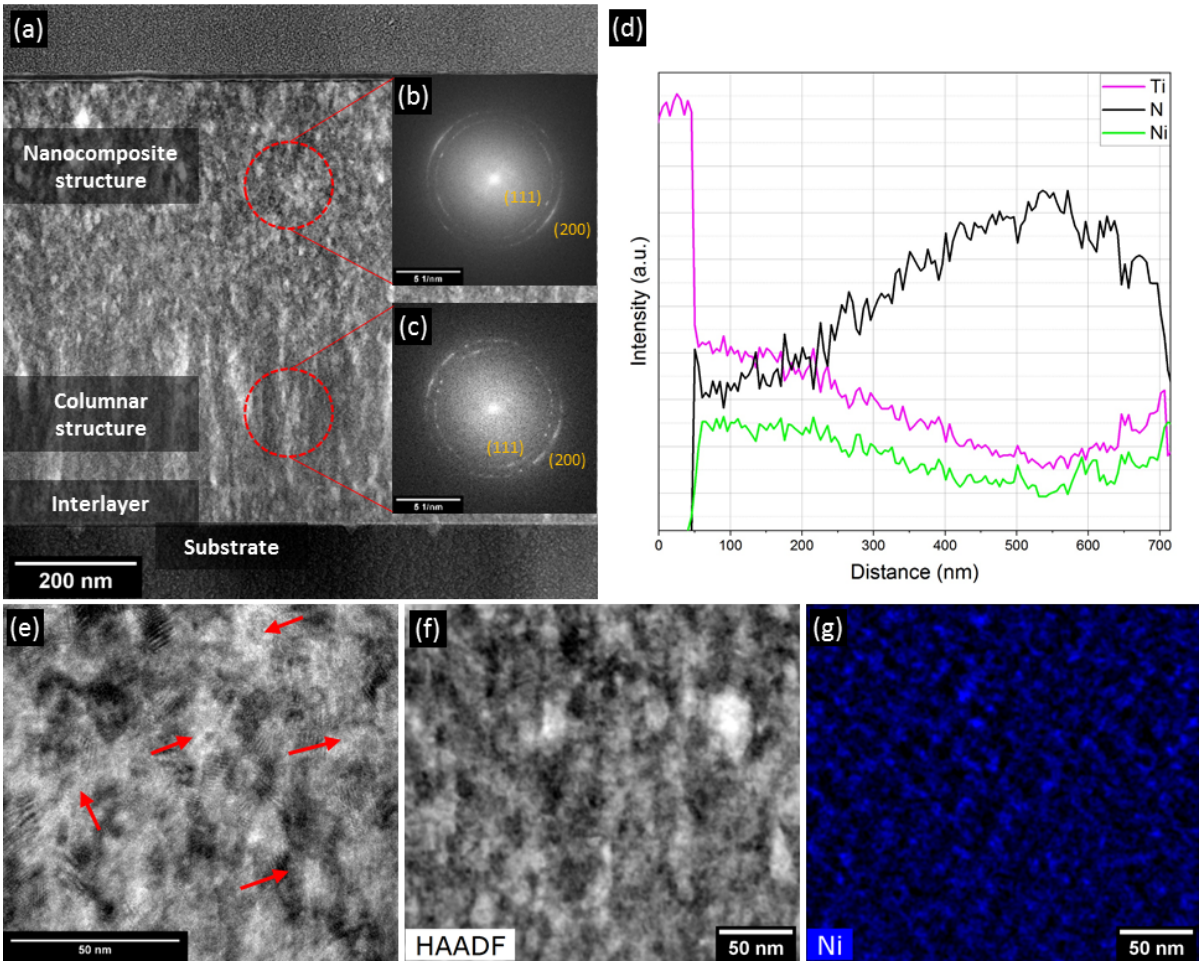


Figure 4.11: Images of the cross-section of the coating on the TiN with 10 at.% Ni position: (a) BF TEM;(b) and (c) DPs taken at the locations marked; (d) EDX profile, (e) HREM showing dense columnar boundaries; (f) HAADF STEM and (g) corresponding EDS map showing the Ni distribution

TEM images of TiN/Ni with 18 at.% Ni are shown in 4.12. The nanocomposite structure is lost with this Ni content, as shown by the distinct diffraction spots found in the DPs of 4.12(b) and (c). In fact, the BF image in 4.12(a) shows that the microstructure is composed of columnar grains but, contrary to the TiN rich location, the columnar grains are narrower, the coating develops a relatively rougher growth front and the columnar grain boundaries are more defective. In fact, the presence of a relative large fraction of voids along the columnar boundaries is evident from the bright lines, pointed by the arrows, that appear in the BF image of 4.12(d), which was taken under slightly underfocused conditions to enhance Fresnel contrast. Finally, the Ni elemental maps (4.12(f)), corresponding to the HAADF STEM image in (e), show that Ni segregates into relatively large veins preferably oriented along the growth direction, two of

which have been signaled by arrows as an example.

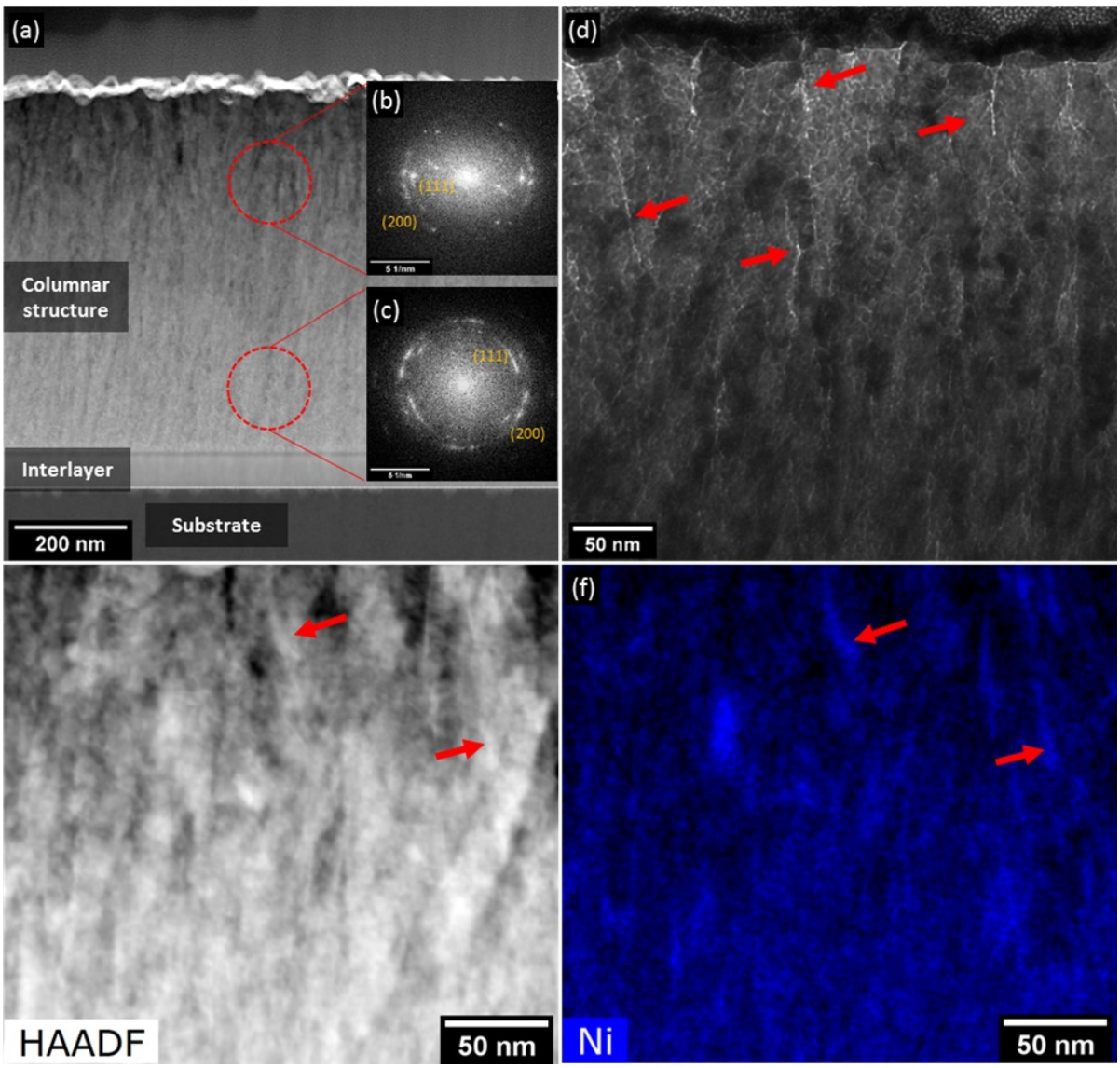


Figure 4.12: Images of the cross-section of the coating on the TiN with 18 at.% Ni position: (a) BF TEM;(b) and (c) DPs taken at the locations marked; (d)HREM showing the corresponding lattice fringes and dense columnar boundaries; (e) HAADF STEM and (f) corresponding EDS map showing the Ni distribution

## 4.6 Discussion

The results of this investigation demonstrate that Ni addition during growth of TiN coatings by reactive sputtering can trigger the formation of a nanocomposite structure formed of equiaxed nanograins of crystalline $\delta$-TiN embedded in a Ni rich amorphous-like phase. This microstructure shows a superior combination of hardness and toughness without residual stresses than can be beneficial for wear applications. Similar results have been observed for TiN/Ni coatings in previous works [2, 59, 61], but only for a limited number of chemical compositions, and using special deposition setups that promote strong ion irradiation conditions, like cathodic arc evaporation [62] or ion beam assisted sputter deposition [19, 59]. As a result, the prevailing ion irradiation effects in such conditions could not be completely decoupled from elemental composition effects on the microstructure development. Moreover, most previous works only measured the hardness of TiN/Ni composite coatings, but the impact of the microstructure on the fracture toughness of the coatings was unknown. The combinatorial thin-film synthesis approach used in this work, together with the use of advanced nanomechanical testing techniques, allowed the continuous screening of the effect of Ni content on the microstructure, residual stresses, hardness and fracture toughness of TiN/Ni coatings. Moreover, all possible compositions are produced in one single coating under identical deposition parameters (sputtering gas, target powers, substrate bias, substrate temperature, etc.) removing uncertainties due to differences in processing conditions, and allows focus the discussion on the role of Ni addition.

Sputtered $\delta$-TiN coatings are one of the most thoroughly studied hard coatings in the last decades and their stoichiometry, microstructure and mechanical properties are very dependent on the deposition conditions. According to 4.4, the $\delta$-TiN phase in the TiN rich side was slightly over stoichiometric under the deposition conditions used in this work. Moreover, high residual compressive stresses appeared (figure 4.7) and a (111) preferred growth orientation developed (figure 4.5). The high compressive stresses generate due to atomic peening and the generation of defects caused by ion bombardment effects, inherent to the sputtering process. Texture development in TiN coatings is affected by many process parameters. It is generally accepted that the (111) preferred orientation arises through a competitive columnar growth

process under kinematically limited conditions, because the (111) oriented columnar grains, which are the grains with the fastest growing direction, overlap the rest of the orientations [55]. The microstructure observed in this coating (figure 4.10) agrees well with that expected through a competitive columnar growth. Moreover, the hardness and elastic modulus, 25 GPa and 330 GPa, respectively, are those expected for good quality (111) oriented dense TiN coatings [63].

As Ni was incorporated into the film, a clear transition was observed from a TiN (111) to a TiN(200) preferred growth orientation (figure 4.5) for Ni contents up to 10–15 at.%, together with a complete relief of the compressive residual stresses (figure 4.8). In this range of Ni contents, the microstructure transformed from a $\delta$-TiN columnar grain structure (figure 4.10) to an equiaxed $\delta$-TiN nanocrystalline microstructure (figure 4.11). The TEM studies suggest the segregation of an amorphous-like Ni rich phase in this case. However, it was not clear if under the non-equilibrium conditions found during sputtering, some Ni could also be dissolved within the $\delta$-TiN phase. In this respect, it is interesting to note that the elastic modulus of the TiN/Ni composite coating remained constant at 330 GPa, up to 13 at.% Ni, while the hardness peaked at 10 at.%Ni and decreased slowly up to 13 at.% Ni. The average fracture toughness followed closely the hardness variation with Ni content, within the large experimental scatter. However, all hardness, fracture toughness and elastic modulus drop dramatically for larger Ni contents.

The elastic modulus is a property that depends on the strength of the atomic bonds in the coating, and it is relatively insensitive to minor additions of alloying elements and/or the material microstructure, as long as the material remains dense and the bond strength remains unaffected. This is particularly relevant for $\delta$-TiN$_x$, which exists over a wide range of Ti/N ratios ($0.6 < x < 1.2$) because changes in composition can be accommodated by a high vacancy concentration in the nitrogen sublattice (for $x < 1$) and the Ti sublattice (for $x > 1$). However, such high levels of vacancy concentrations lead to strong reductions in elastic modulus and hardness in TiN coatings due to the impact of stoichiometry on bond strength [63]. The fact that the elastic modulus remained constant at 330 GPa up to 13 at.% Ni indicates, therefore, that the $\delta$-TiN remained close to stoichiometry up to that point and enforces the conclusion that most of the Ni segregated out during the growth of the $\delta$-TiN crystalline grains. As a

matter of fact, the RBS results in figure 4.4 indicate that the Ti/N ratio remained close to 1 at least up to 10 at.% Ni. Another indirect evidence of the exact chemical composition of the $\delta$-TiN phase might be found on the value of the lattice parameter that can be extracted from the diffracted peaks in the XRD spectra that show substantial shifts with respect to the reference peak positions with Ni content (figure 4.5). The lattice parameters calculated using Bragg's law in the Bragg-Brentano geometry provide the out-of-plane lattice parameter, $a_\perp$, of the diffracting grains, which might be affected, by chemical composition and by the in-plane residual stresses due to Poisson effects. It is, however, possible to estimate the stress-free lattice parameter, $a_0$, from the knowledge of the in-plane residual strain $\epsilon_{\parallel}$ measured in figure 4.7 according to:

$$a_0 = \frac{a_\perp}{(1-2\nu\cdot\epsilon_{//})} \tag{4.1}$$

where $\nu$ is the Poisson's ratio of TiN. The results are plotted in figure 4.7, which shows the measured out of plane lattice parameter as well as the estimated stress free lattice parameter from the (200) and (111) peaks as a function of Ni content. The horizontal dash line represents the reference lattice parameter for stoichiometric stress-free $\delta$-TiN. The initial section with Ni contents below 0.5 at.% (TiN-1) reveals a slightly increased stress-free lattice parameter. Even though the maximum lattice parameter is expected for the stoichiometric compound [64], incorporation of N atoms in tetrahedral interstitial sites has also been observed for over-stoichiometric films (x > 1) in the case of TiN films grown under non-equilibrium conditions, leading to an expansion in the lattice parameter [**sundgren**], in agreement with our observations. Moreover, the high density of defects resulting from ion bombardment induced atomic peening might also contribute to this lattice parameter expansion [55]. With increasing the Ni content and with the transition to a (200) preferred orientation, however, the lattice parameter of the $\delta$-TiN phase continuously decreased and reached the reference value for stoichiometric $\delta$-TiN for Ni contents up to around 15%. The Ti/N ratio remained close to 1 up to at least 10 at.% Ni according to the RBS results, and this result supports the conclusion that most of the Ni segregates out of the TiN grains during growth. It appears, therefore, that the transition from a competitive columnar grain growth to a nanocrystalline nanostructure is triggered by the amorphous-like Ni phase stopping the growth of the TiN grains and forcing their re-nucleation, as it was proposed by Abadias, but without affecting their stoichiometry. This explains the development of a (200) preferred growth orientation, which is the preferred nuc-

leation orientation of TiN because its surface energy is the lowest for the (001) surface [65], and the little variation of elastic modulus in this composition range. In the light of the hardness and fracture toughness results (figure 4.8) the TiN/Ni interfaces that develop are much stronger that the columnar grain boundaries that develop in pure TiN coatings, which explains the continuous increase in hardness and toughness, even when the residual stresses are dramatically reduced.

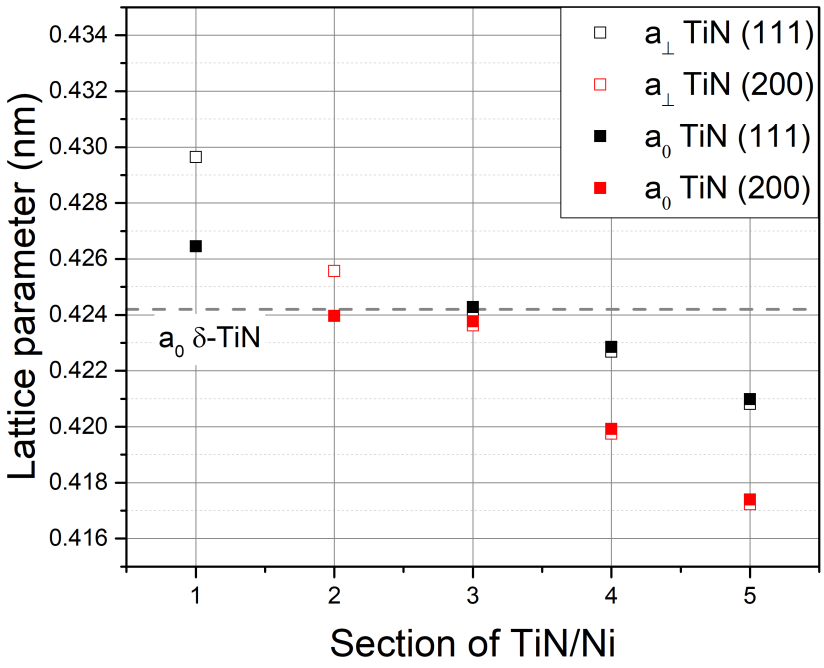


Figure 4.13: Out-of-plane lattice parameter evolution and estimation of the stress-free lattice parameter of $\delta$-TiN phase with Ni content

The dramatic reduction in compressive residual stresses with the incorporation of Ni also deserves further attention. One of the benefits of using the combinatorial approach presented in this work is that the compositionally graded film is grown under identical deposition conditions (bias voltage, magnetron power, gas flow rate, nature of sputtering gas species, temperature and pressure), and therefore, equivalent energy and flux of the bombarding species. If the compressive residual stresses found in the TiN rich side are due to atomic peening induced by ion bombardment, it is surprising that the incorporation of Ni to just a few atomic per cent produces such a drastic reduction of residual stresses. It is well known that the development of

a (002) texture can reduce the defect density induced by ion bombardment due to channeling effects, because <001> is the most open channeling direction in TiN [66]. But, on top of texture effects, such a drastic reduction in compressive residual stresses can only be explained if the Ni rich amorphous-like phase that surrounds the TiN nanograins contributes to relieve part of these residual stresses. Finally, the elastic modulus, hardness and fracture toughness of the coatings were drastically reduced for Ni contents higher than 13 at.% Ni. This reduction is triggered by the loss of the nanocomposite type microstructure. Instead, the microstructure evolves to the formation of columnar grains with a random texture surrounded by Ni-rich amorphous islands. Moreover, voids appear at grain boundaries (figure 4.12), contributing to the large drop in all, elastic modulus, hardness and fracture toughness. Additionally, such a drastic reduction in elastic modulus might also be a consequence of the loss of stoichiometry of the $\delta$-TiN phase. As a matter of fact, the lattice parameter of the $\delta$-TiN phase for this Ni content shows values that are well below what is expected for stoichiometric TiN (figure 4.12). It is hypothesized that either the TiN becomes highly over-stoichiometric or some Ni atoms get incorporated into the TiN phase by substitution of Ti atoms by Ni. This would result in a reduction in the lattice parameter because the ionic radius of $Ni^{3+}$ (0.056 nm) [56] is smaller than that of $Ti^{3+}$ (0.075 nm) Park *et al.*, as has also been observed in TiN/Ni/Si3N4 composite coatings [43]. This hypothesis is supported by the fact that the Ti/N ratio increases from 1 to 1.4 with increasing the Ni content from 7 to 17 at.% (figure 4.4), while the (Ti + Ni)/N ratio remains around 1 in the latter case. Considering that some of the Ni is present in the form of Ni rich amorphous-like islands, such atomic ratios can only be understood if the $\delta$-TiN phase contains substantial amounts of Ni and/or a high fraction of vacancies in the Ti sub-lattice. In either case, this would result in a large reduction in the bond strength of the TiN phase.

Regarding the nanoindentation tests at high temperature, no noticeable benefits were observed despite the microstructural change. Thus, another material is recommended to be used instead of Ni.

# Chapter 5

# Hierarchical microstructure coatings: Results, analysis and discussion

The build-up of coatings with a hierarchical microstructure was accomplished by combining the aforementioned nanocomposite nanostructure and a ceramic-metal multilayer system.A multilayer series combining pure ceramic TiN layers intercalated with metallic Ni layers was prepared, as reference. Then, the TiN layers were replaced by TiN(10)Ni nanocomposite layers, which corresponds to the coating composition that yielded the best combination of hardness and toughness in the previous study. Additionally, two different multilayer approaches were considered: one with very thin layers with the idea of increasing the density of interfaces and another with thick layers, which should favour the development of plasticity in the Ni layers.

The order in which the coatings are characterized is the following: thickness and residual stresses, roughness, X-ray diffraction, microstructure and mechanical properties. This order allows to modify parameters of later experiments so the results are valid. Two multilayer systems were deposited to see the effect of a high volume of interfaces and high plasticity. For this purpose the layer thickness selected for the first one are 10 and 2nm for the hard phase and Ni layers respectively. In the case of the second the layer thickness are 100nm for the hard phase and 60nm for the Ni.

## 5.1 Thickness and residual stresses

Table 5.1 presents the thickness of the coatings of this new set of samples and the substrate curvature after deposition. The residual stresses were calculated by using Stoney's equation 3.2.

In agreement with the results obtained in the previous study, TiN presents the highest level of residual stresses, which are reduced by the introduction of Ni, either for TiN(10)Ni or any multilayer system, and having a greater effect when combining them. The curvature of the multilayer samples with 60nm thick Ni layers varied from -45m to -1.6km, and are thus marked as "$\infty$" in the table. These measurements are similar to the ones obtained on Si wafers before deposition, therefore the residual stresses are assumed to be negligible.

Table 5.1: Thickness and residual stresses

| Material | Thickness [$\mu$m] | Substrate curvature [m] | Residual stresses [GPa] |
|---|---|---|---|
| TiN | 1.65 | -2 | -2.9 |
| TiN(10)Ni | 1.65 | -2.2 | -2.6 |
| 10TiN-2Ni | 1.4 | -3.14 | -2.2 |
| 10TiN(10)Ni-2Ni | 1.35 | -5 | -1.4 |
| 100TiN-60Ni | 1.63 | $\infty$ | 0 |
| 100TiN(10)-60Ni | 1.7 | $\infty$ | 0 |

Measurements performed by FIB trench method in the previous chapter showed that TiN(10)Ni had almost no residual stresses (figure 4.7), while the residual stresses were not negligible for the same film composition in the new set of coatings. This may have been caused by the change of the deposition parameters which provided a higher deposition rate. But, nevertheless, the results are consistent in the fact that the addition of Ni contributes to relieve part of the residual stresses present in the pure TiN coatings deposited in the same conditions. As it was discussed in the analysis of the gradient samples, the reduction of the residual stresses from pure TiN to

TiN(10)Ni is related to the refinement of the grains due to the formation of the nanocomposite structure and the segregation of Ni to the grain boundaries.

The multilayered coatings, with the intercalation of thin pure Ni layers, further contribute to a reduction of residual stresses. There might be two reasons for this. The first one is the presence of a metallic phase, which may be able to slightly relax and thus, reduce the stress build up. The second one is the forced renucleation of the ceramic layers after each Ni layer, which limits their thickness, and results in grain refinement, therefore limiting the to build up of residual stresses. Additionally, the multilayer containing TiN(10)Ni layers presents lower residual stresses than the coating with pure TiN layers, which demonstrate a beneficial synergetic effect of the nanocomposite and multilayer structure on limiting the build up of residual stresses.

Thicker Ni layers seem to provide the coating with a ductile phase without any inherent residual stresses, as it was seen previously. This may allow these layers to accommodate any residual stresses that may be introduced by the ceramic layers having an overall stress-free coating.

## 5.2 Roughness

Figure 5.1 show the surface morphology changes between the different coating systems both in the as-deposited state, and where the ceramic layer is either pure TiN or TiN(10)Ni. Monolithic coatings present a relatively smooth surface while the roughness of the thin multilayer samples seem to be even less pronounced. On the other hand, the coatings with thick layers present a very rough surface. The monolithic TiN(10)Ni coating shows a similar roughness to pure TiN, nevertheless the height distribution is different. While TiN presents wider but fewer peaks, TiN(10)Ni presents sharper and more numerous peaks. Differences coming from the hard phase layers used in the different multilayer systems seem to be negligible.

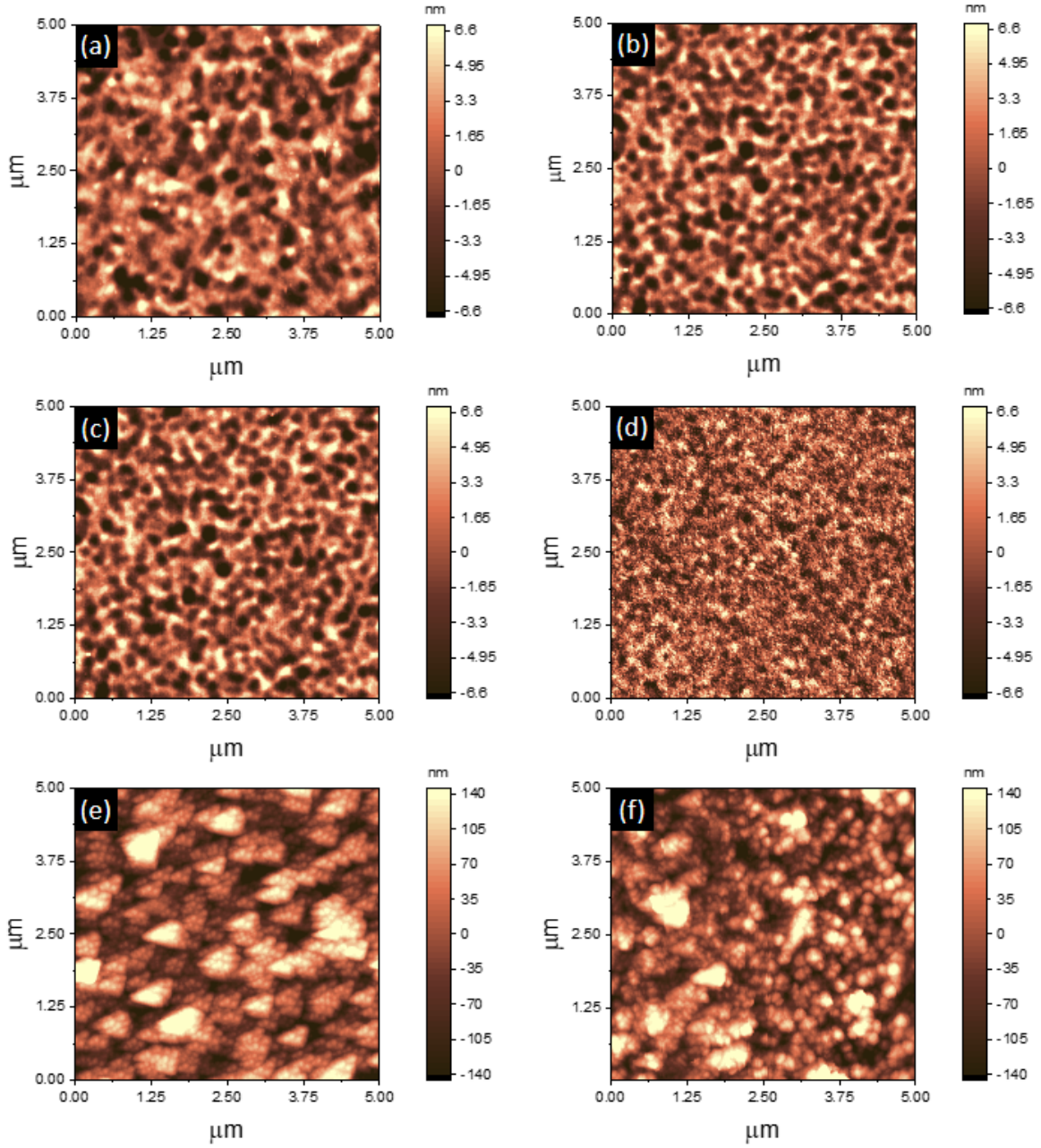


Figure 5.1: AFM images from the monolithic reference samples and the multilayer coatings as deposited. (a) TiN, (b) TiN(10)Ni, (c) 10TiN-2Ni, (d) 10TiN(10)Ni-2Ni, (e) 100TiN-60Ni and (f) 100TiN(10)Ni-60Ni.

Roughness differences between TiN and TiN(10)Ni are likely related to the grain size. TiN probably presents a columnar structure much broader than the smaller grains of the TiN(10)Ni, as suggested by previous analysis of the gradient samples and the XRD spectra of these samples (Section 5.3).

The smoother surface of the thin multilayer samples are similarly likely due to the forced renucleation process created by the introduction of the thin Ni layer, not allowing the grains to grow and thus, limiting the grain size and the roughness roughness of the coating.

However, the thick multilayer samples present a much rougher surface Considering that the mononithic ceramic coatings do not develop any substantial roughness with thickness, the large roughness must arise from growing relatively thick Ni layers. This might be a consequence of the deposition temperature, because it is well known that Ni, when deposited above the recrystallization temperature, generates a very rough surface [44]. If this is the case, it is likely that roughness will generate from the first Ni layer and that would be replicated and augmented with the number of layers. This will be more clear with the microstructural analysis of section 5.4.

It has to be noted that for the heat treated samples the images were taken from regions in the Si substrate samples, which in the case of TiN, TiN(10)Ni and 10TiN-2Ni were partially or almost fully delaminated. Another thing to take into account is the presence of oxygen and thus the surface morphology may have change due to the formation of oxides.

## 5.3 X-ray diffraction analysis

Figure 5.2 presents the XRD spectra of the coatings deposited on the Si substrates. The crystalline peaks present in all the coatings correspond to TiN(111), TiN(200), Ni(111) and Ni(200), while the Ti(100) peaks that appear in some of them come from the interlayer. Pure TiN presents a very strong (111) texture, with a small shift towards lower angles. With the addition of 10% of Ni this texture transitions to only (200) as expected from the previous analysis using the high-throughput method. Nevertheless, the peak is also slightly shifted to lower angles.

The multilayer samples with 2nm Ni layers present a TiN(200) texture independently of the Ni content of the ceramic phase, with both peaks almost at the reference position for pure TiN. However, the sample with TiN presents higher intensity and notably, no presence of any Ni peaks. The texture evolves to a mixed TiN(111) and TiN(200) in both cases, with increasing the thickness of the ceramic/nanocomposite layers to 100 nm and the thickness of the Ni layers to 60 nm. In addition, Ni (111) and Ni (200) peaks appear now, with the first one being more significant.

Upon heat treatment, the XRD spectra did not show significant changes, except for a small reduction in the peak widths and a slight shift towards higher diffraction angles. All peaks are slightly deviated towards higher angle and a bit narrower. An additional small peak appeared for the 100TiN/60Ni coating in the position expected for NiO, which indicates a slight oxidation during annealing.

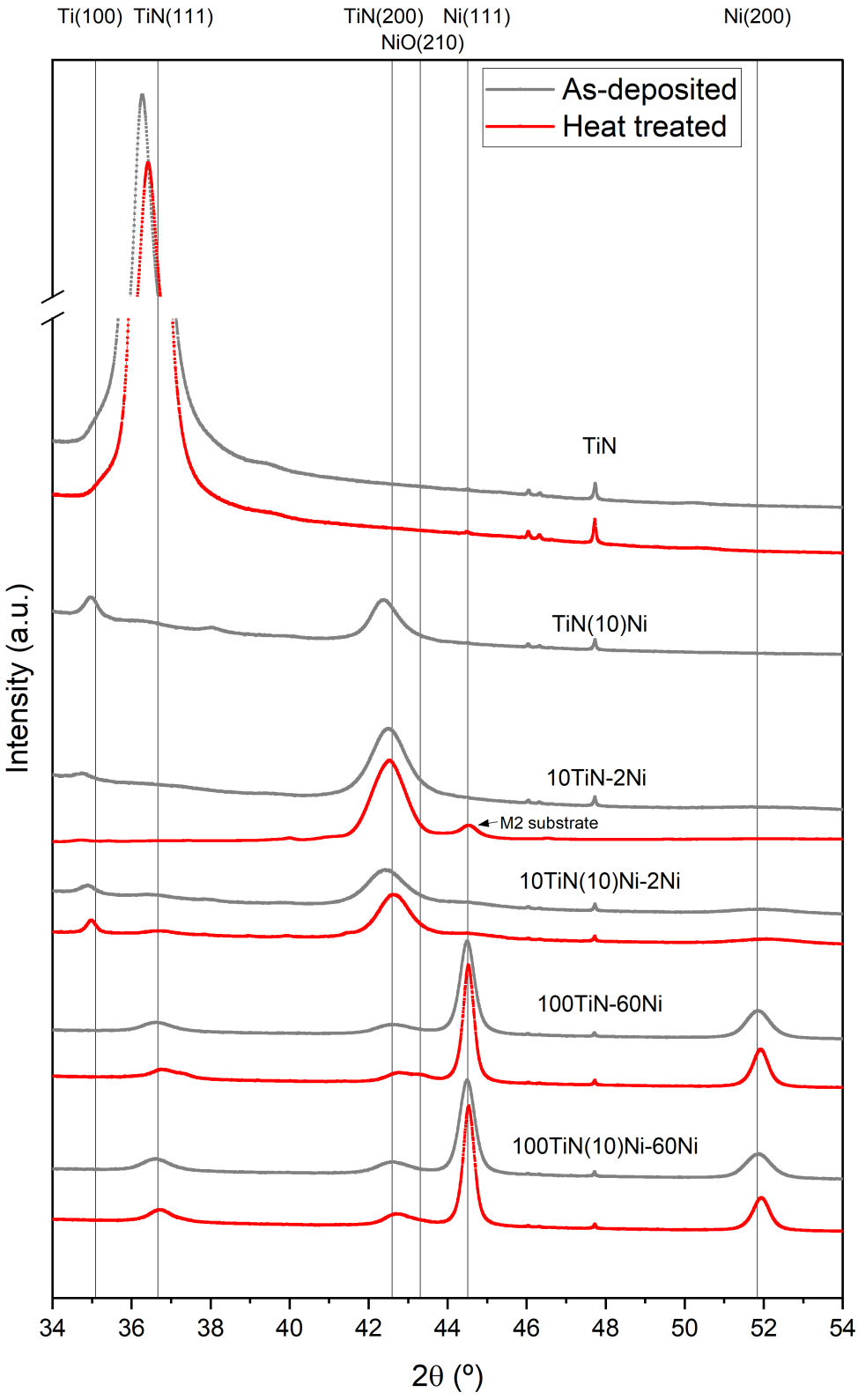


Figure 5.2: XRD patterns of monolithic reference samples and multilayer coatings as-deposited and heat treated.

The pure TiN coating presents a very intense (111) peak. This is consistent with the analysis of section 4.2, because this pure TiN coating is much thicker, which contributes to developing a stronger (111) texture with wider and more crystalline columnar grains. The peak shift towards lower diffraction angles is consistent with the high level of compressive residual stresses encountered for this coating in the previous section.

Regarding the monolithic TiN(10)Ni coating, the results are also consistent with the ones obtained in the previous set of samples. The incorporation of Ni results in a drastic change to a (200) texture of the TiN phase and lower intensity and wider diffraction peaks, in agreement with the expected transition from a columnar structure to a nanocomposite type structure, with small TiN equiaxed grains embedded in an amorphous-like Ni matrix. Additionally, the TiN peaks are also slightly shifted to lower diffraction angles, consistent with the higher residual stresses encountered for the new deposition conditions, that nevertheless are lower than for the pure TiN coating.

The multilayers with 2 nm thick Ni layers do not present any crystalline Ni peak, which indicates that the Ni layers are initially amorphous-like. The pure TiN layers present a (200) texture, the favored preferred orientation during nucleation, which is consistent with the fact that the amorphous-like Ni layers stop the growth of the TiN layers, so that each subsequent TiN layer is forced the re-nucleate again. The multilayer containing the TiN(10)Ni layers also showed a preferred (200) texture, as expected due to the inherent nanocomposite microstructure that the layers should have in this case, independently of the presence of the thin Ni interlayers.

Finally, the 60 nm thick Ni layers in the thicker multilayer coatings do show crystalline peaks, contrary to the thin 2 nm Ni layers. As it was shown previously, the Ni layers seemed stress-free when deposited alone, and since the peaks are at the reference values it can be assumed that the same occurs within the coating. This might occur because the deposition temperature is above the recrystallization temperature of Ni which relaxes the stresses in the Ni layers. If the Ni layers are able to accommodate all stresses coming from TiN, it would explain why these two samples presented no residual stresses. In the case of the crystal orientation of the ceraminc layers a mixed texture appears for both, pure TiN and TiN(10)Ni. This is

not surprising for the case of the pure TiN layers because the crystallline Ni layers would not force the re-nucleation of each successive TiN layers, so that the regular texture encountered in the monolithic TiN coatings is prone to develop. The fact that the TiN(10)Ni layers present a mixed texure is more difficult to explain. There are different possible reasons for this. First, that the actual Ni content in these layers might be too low to induce the nanocomposite microstructure. Second, that the high bias used for the deposition of these coatings influences the texture of the TiN(10)Ni layers. Or lastly, that the growth morphology suffers a drastic transition, as suggested by the large roughness of the coatings. These possibilities will be further discussed below in the light of the TEM observations.

As it was seen for the gradient samples (4.2), the peaks became a bit narrower and displaced towards higher angles after the heat treatment. These changes in the spectra were attributed to the partial release of residual stresses in the case of sections with Ni content below 15% and a slight improvement of the crystallinity of the TiN phase, which was expected since the maximum Ni content of the TiN is supposed to be around 10%. Regarding the Ni peaks from the thicker multilayer samples, this effect is more pronounced due to the fact that, despite the relatively short duration of the heat treatment, the chosen temperature was above its recrystallization temperature.

At this point, further analysis regarding the composition and microstructure of the ceramic layers is required to confirm this hypothesis. Both will be performed by TEM.

## 5.4 Microstructural analysis

Figure 5.3(a) shows the cross-section image of the pure TiN sample. It is noticed that the coating presents a clear columnar structure similar to what it was seen during the high-throughput analysis. The grain width close to the surface ranges from 130 to 180 nm. Figure 5.3(b) presents a high resolution image of a grain boundary and for each of the grains involved their respective fast Fourier transformed (FFT) image. For the grain on the left, the FFT only appears to have a (111) orientation while for the grain on the right the (200) diffraction spots also appears.

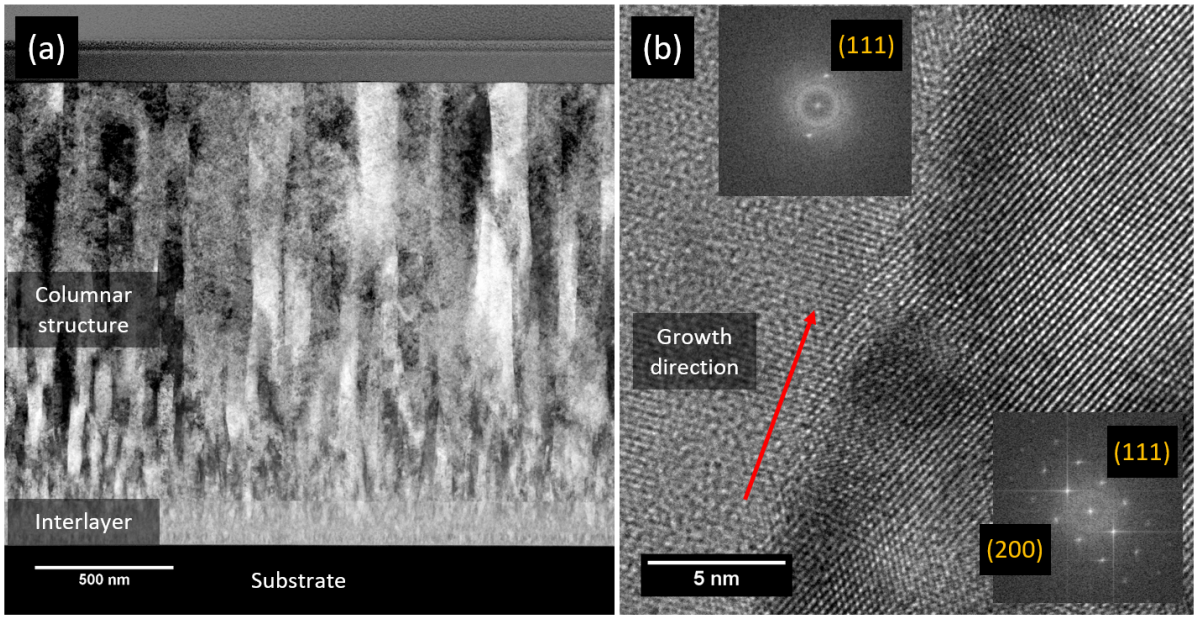


Figure 5.3: Images of the cross-section of the pure TiN coating: (a) BF TEM and (b) HREM of an area around a grain boundary. The insets show the FFT of the two grains involved.

Figure 5.4 presents images that belong to the cross-section of the TiN(10)Ni coating. The BF image of figure 5.4(a) shows that the coating does not have a columnar structure but it is formed by equiaxial grains. The ED pattern, figure 5.4 (b), does not show any evidence of crystalline Ni and it presents a preferred (200) $\delta$-TiN orientation in the form of half arcs, while the (111) $\delta$-TiN appears as a ring. As it can be seen in the HREM image, figure 5.4 (c), the grains seem to be surrounded by another phase. This was observed in previous analysis demonstrating that the nanocomposite structure is formed. The BF STEM and EDS map of Ni, figure 5.4 (d) and (e) respectively, show that Ni is distributed homogeneously supporting the idea of having a nanocomposite structure.

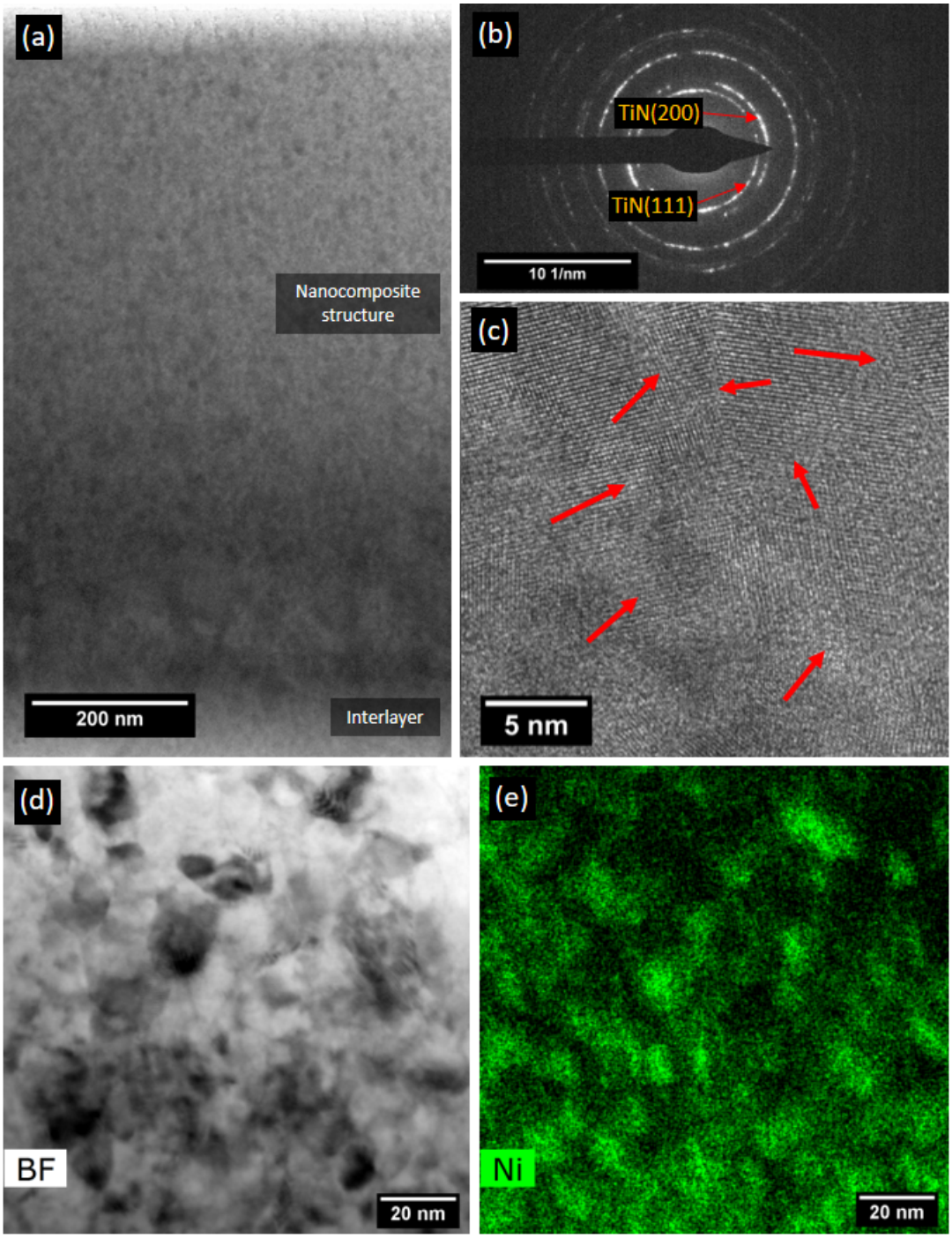


Figure 5.4: Images of the cross-section of the TiN(10)Ni coating: (a) BF TEM; (b) ED pattern; (c) HREM, (d) BF STEM and (e) EDS map of the corresponding area showing the Ni distribution.

Figure 5.5 presents an image from the cross-section of the 10TiN-2Ni multilayer coating. The multilayer structure is clearly revealed in the BF image of figure 5.5 (a). The ED pattern, figure 5.5 (b), shows elongated spots for (111) and (200) $\delta$-TiN, revealing a preferred (200)

orientation for $\delta$-TiN. Figure 5.5 (c) shows a BF STEM area of the coating and (d) the Ni distribution in the same area. Ni is not distributed uniformly within the layers, but it forms elongated discontinuous particles. This microstructure may have formed due to the immiscibility between Ni and TiN, together with the agglomeration of Ni from the thin layers into particles. Despite the formation of these particles, Ni does not appear in the diffraction pattern.

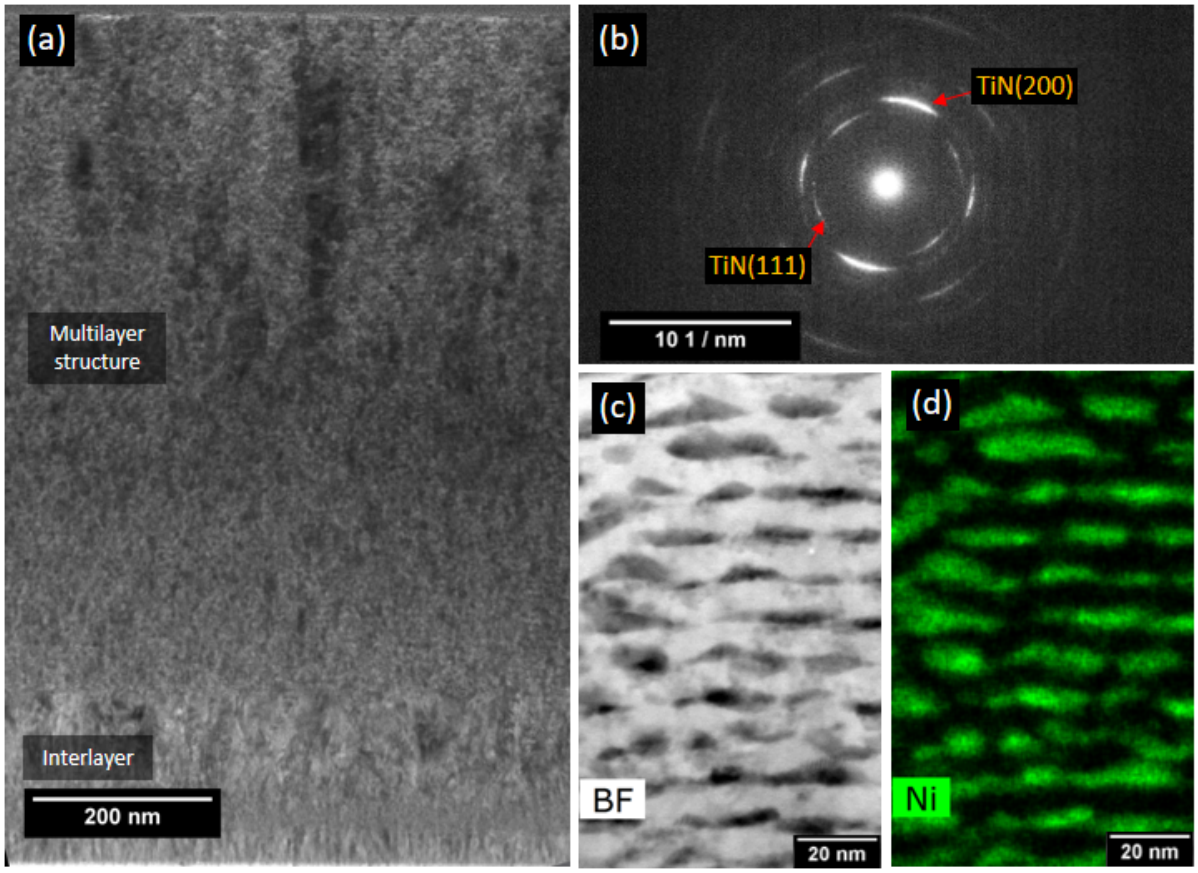


Figure 5.5: Images of the cross-section of the 10TiN-2Ni coating: (a) BF TEM; (b) DP; (c) BF STEM and (d) EDS map of the corresponding area showing the Ni distribution.

Figure 5.6 shows the TEM images obtained from 10TiN(10)Ni-2Ni combining the nanocomposite with the multilayer structure. The multilayer structure is clear in the BF TEM in figure 5.6 (a). The ED pattern (b) shows the common diffraction rings for equiaxed TiN grains encountered for the TiN(10)Ni nanocomposite structure, together with diffraction spots that can be attributed to Ni, indicating the partial crystallization of this phase. Furthermore, it is noticed that the (200) $\delta$-TiN ring has a higher intensity than the (111) with a brighter region which coincides with the elongated dot observed in 10TiN-2Ni. The BF STEM image in (c) and EDX map of Ni corresponding to the same region in (d). The images show a similar struc-

ture to that found for 10TiN-2Ni, in which the Ni layers are not continuous, but form elongated particles.

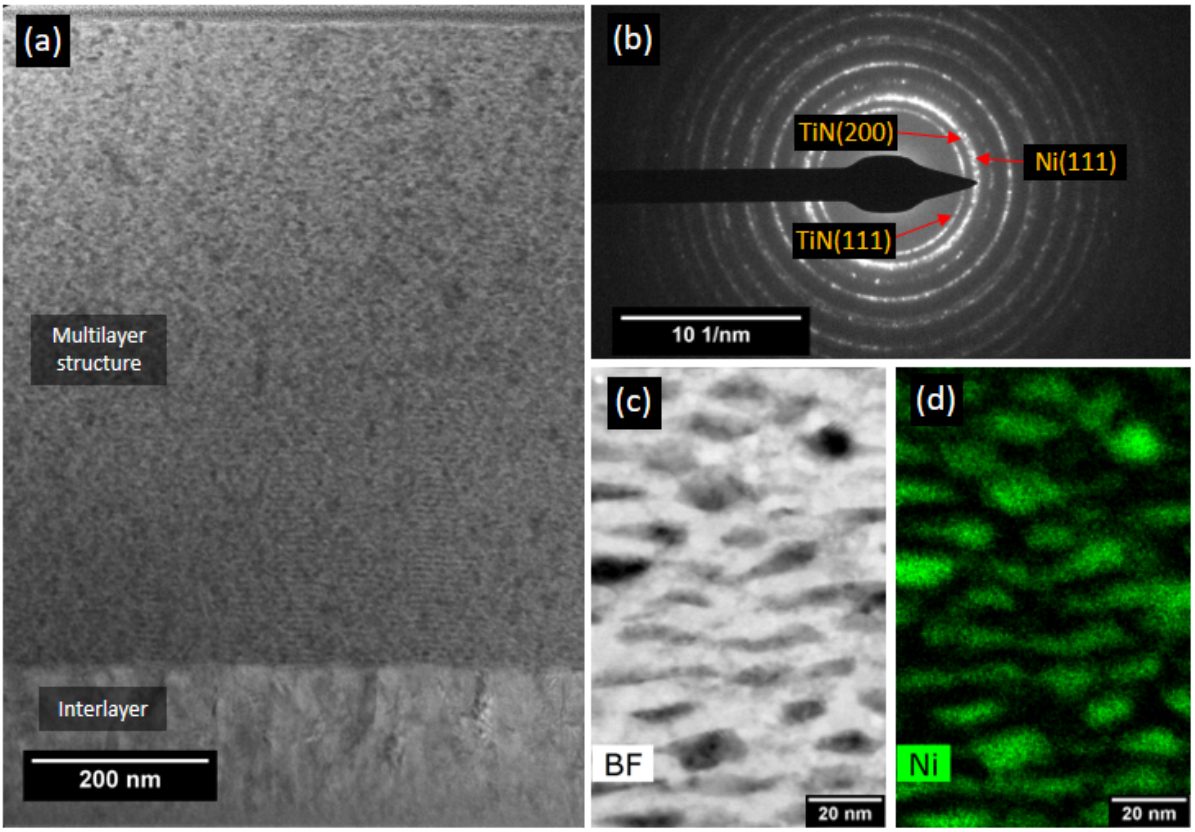


Figure 5.6: Images of the cross-section of the 10TiN(10)Ni-2Ni coating: (a) BF TEM; (b) DP; (c) BF STEM and (d) EDS map of the corresponding area showing the Ni distribution.

Figure 5.7 presents images from 100TiN-60Ni. It has to be reminded that the deposition conditions for Ni were changed due to adhesion problems. However, as it can be seen in the STEM BF image in figure 5.7 (a) the coating presents a large number of pores within the first layer of Ni after the interlayer. Additionally, a lot of discontinuities are seen at the Ni grain boundaries, some of which extend through several layers.The Ni grains are equiaxial and are adjacent to the other leaving cavities in the first layer. Furthermore, figure 5.7 (c) shows a TiN layer which grows from a Ni grain forming a columnar microstructure The image shows how the TiN grains, due to the rough surface, do not necessarily grow parallel to the deposition direction, but in the direction dictated locally by the growth front. This explains the differences in the prefered orientation of the thicker multilayers, with respect to the thinner multilayers, which maintain a planar growth front. The diffraction pattern (b) presents multiple spots for

each orientation and not showing any preferred orientation of either $\delta$-TiN nor Ni. The BF STEM, figure 5.7 (d) and its Ni EDs map (e) confirm what was observed previously, Ni grains grow more or less equiaxially with a single grain per layer while TiN accommodates and partially fills the space between the grains.

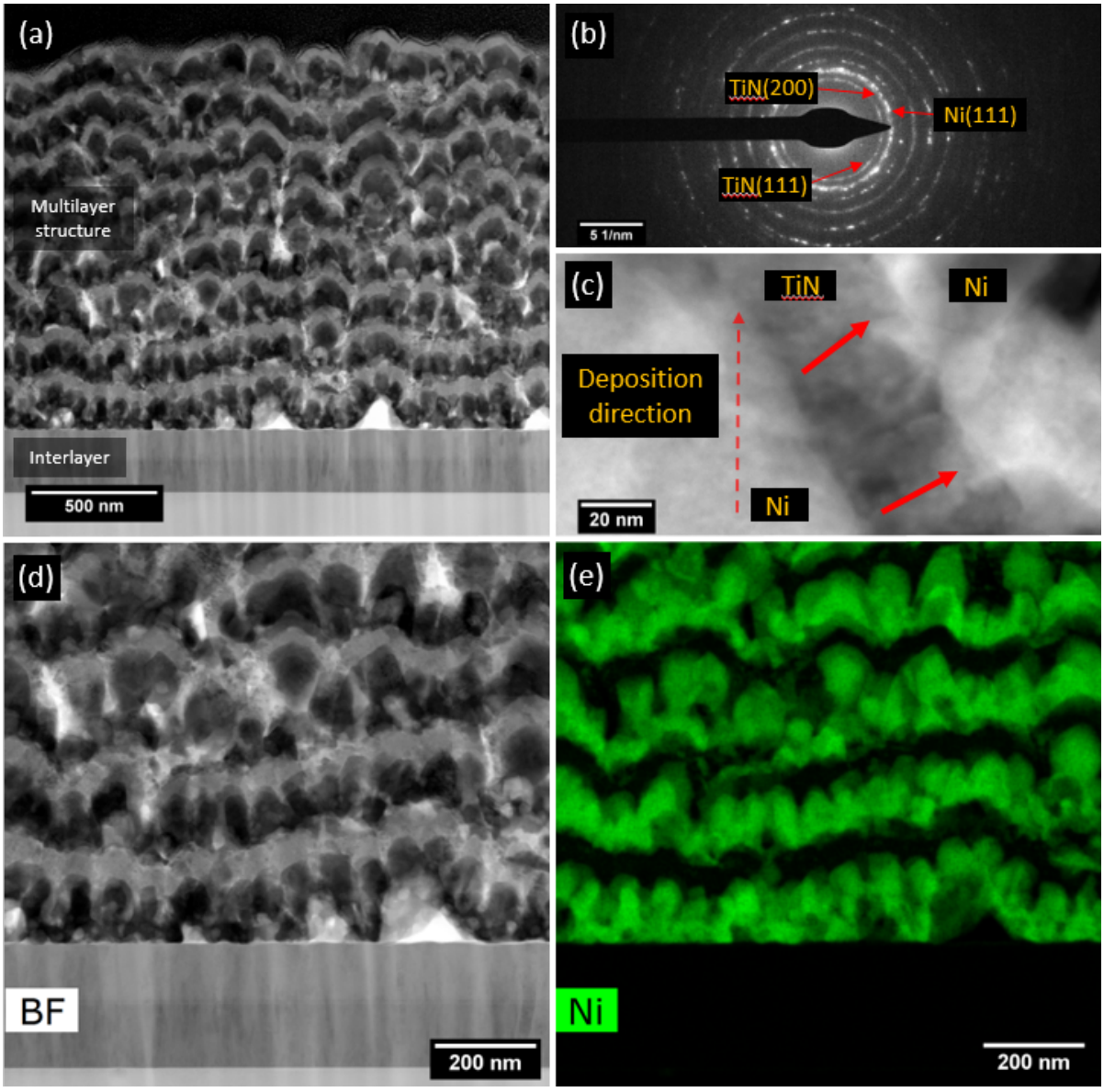


Figure 5.7: Images of the cross-section of the 100TiN-60Ni coating: (a) BF STEM; (b) DP; (c) HAADF STEM, (d) BF STEM from the area where EDS was performed and (e) EDS map of the corresponding area showing the Ni distribution.

Figure 5.8 shows images obtained from 100TiN(10)Ni-60Ni. A BF STEM image (a) from the coating reveals that, as for 100TiN-60Ni, the coating presents a lot of pores and cavities formed at the first Ni layer. The diffraction pattern is similar as well, presenting TiN (111) and

(200) rings and Ni (111) spots. Figure 5.8 (c) shows that the TiN between Ni layers exhibits a fine columnar structure. The BF STEM (d) and the EDX Ni map (e) show that the Ni layers are very rough and formed by big Ni grains with TiN filling the spaces in between, very similarly to case of the pure TiN.

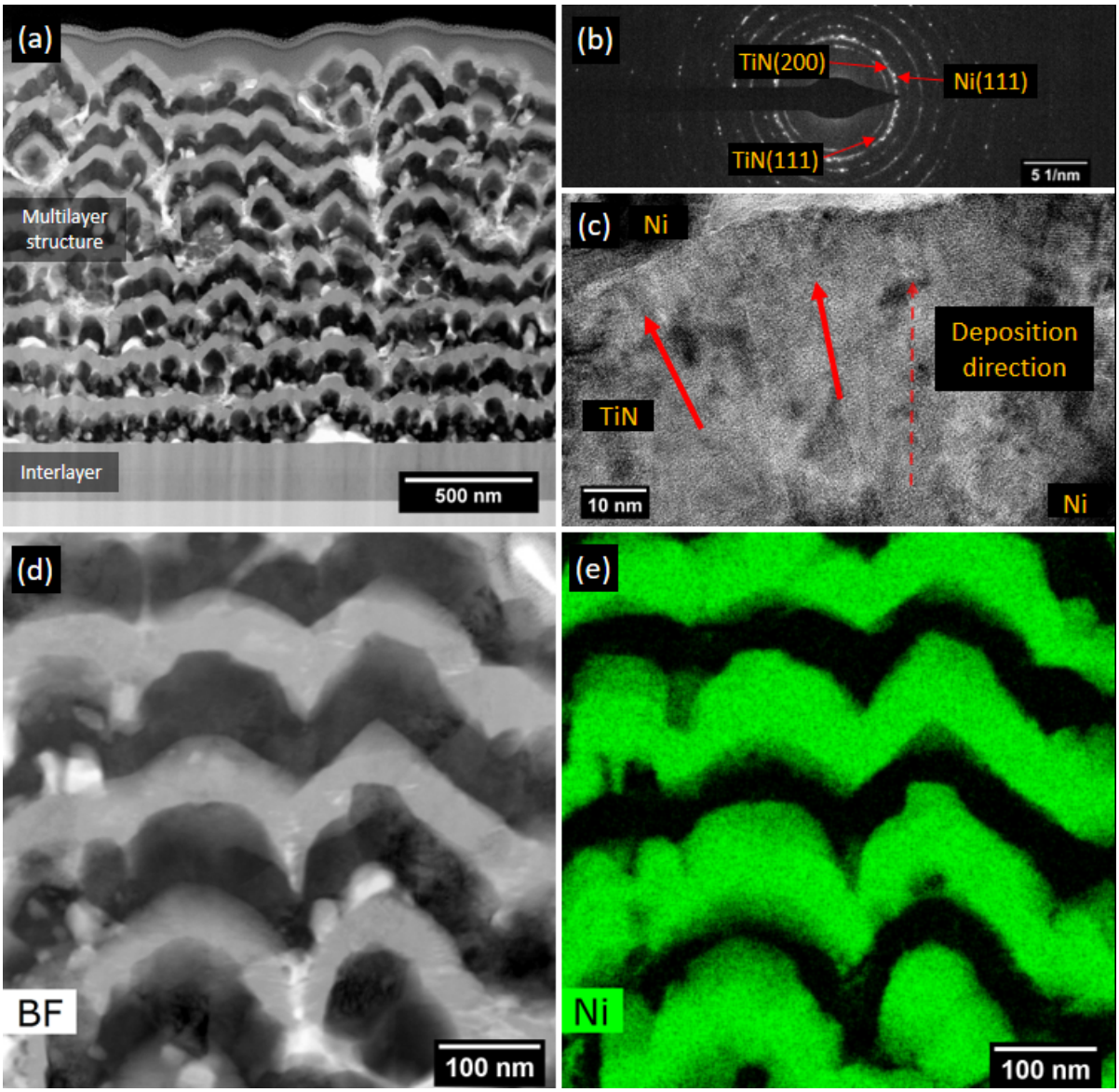


Figure 5.8: Images of the cross-section of the 100TiN(10)Ni-60Ni coating: (a) BF STEM; (b) DP; (c) HAADF STEM, (d) BF STEM from the area where EDX was performed and (e) EDS map of the corresponding area showing the Ni distribution.

The TEM analysis reveals that the thick Ni layers are very rough, which may be the reason why a mixed texture appear in the XRD spectra. Figure 5.9 shows a schematic of the growth of TiN after the deposition of a Ni layer, in which the back dotted lines mark the growth ori-

entation with the respect to the growth front and the red arrows, the orientation perpendicular to the Si wafer. In figure 5.9, for grain (a) both lines are parallel, while for grain (b) they form an angle. In both cases, the TiN grain grows with the more stable (200) orientation and perpendicular to the surface of the previous layer. However, since the orientation of grain (b) is not perpendicular to the Si substrate, this grain will not appear as (200) $\delta$-TiN in the X-ray analysis but with a random orientation.

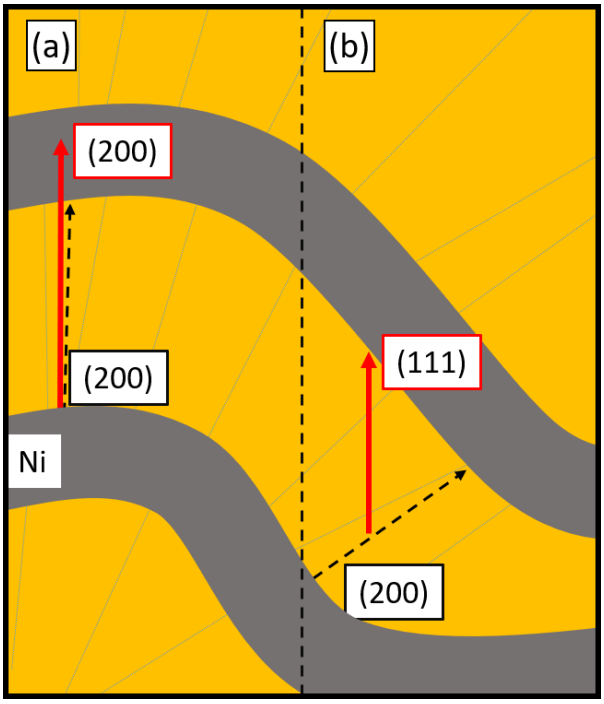


Figure 5.9: Schetch of TiN growth on rough Ni layer.

## 5.5 Mechanical properties

### 5.5.1 As-deposited coatings

Figure 5.10 presents the elastic modulus, hardness and toughness of the monolithic reference samples and the multilayer as-deposited samples tested at room temperature. Taking TiN as reference for comparison, TiN(10)Ni presents higher values as seen during the high-throughput study for all mechanical properties. In the case of the thin multilayered coating with pure TiN, while it presents lower hardness and elastic modulus, its fracture toughness is much higher than

pure TiN although not as much as TiN(10)Ni. However, when having this multilayer system with TiN(10)Ni instead of pure TiN, the elastic modulus, hardness and toughness increase. For the latter, the toughness is even higher than the monolithic TiN(10)Ni despite having somewhat lower hardness and elastic modulus. Both thick multilayer coatings present very low hardness and elastic modulus compared to the rest of the coatings while the toughness of these coatings is only slightly lower compared to TiN.

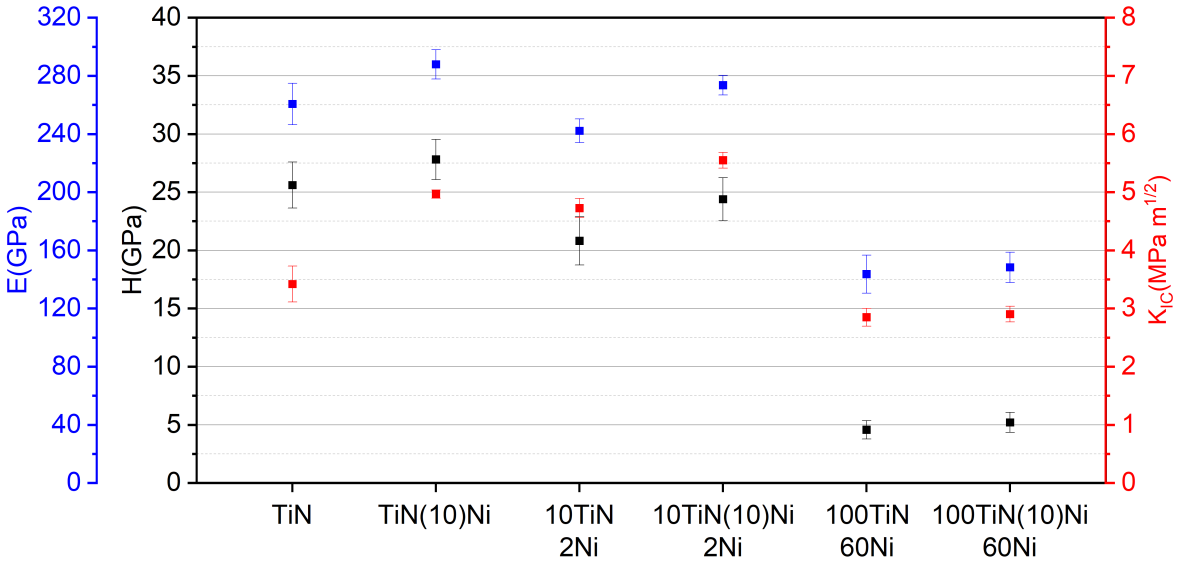


Figure 5.10: Hardness, elastic modulus and fracture toughness of monolithic reference and multilayer coatings

As it was seen during the high-throughput study, TiN(10)Ni presents overall better mechanical properties due to the grain refinement and the formation of a nanocomposite structure [67]. Regarding the thin multilayer coatings it is noted that despite the reduction of the hardness and elastic modulus caused by the addition of the thin Ni discontinuous layers, the toughness notably increases as compared to monolithic TiN. The reduction of the elastic modulus was expected since pure Ni presents a lower value than TiN. Due to its microstructure there are two main mechanisms coming into play, the introduction of a high number of interfaces and the refinement of the structure of the ceramic phase as seen in figure 5.5. Both of them inhibit the crack growth and therefore, despite the lower hardness, present higher toughness

than their respective monolithic coatings.

The changes are very relevant specially for TiN(10)Ni and 10TiN-2Ni. The microstructural change from TiN to TiN(10)Ni is the refinement of the grain size accompanied by the formation of the Ni tissue phase. However, the addition of the Ni elongated particles reduces the hardness but further increases the toughness. This increment in toughness may be caused by the addition of more interfaces and a further refinement of the grain size.

The thick multilayer systems present lower elastic modulus and hardness values since the Ni content is very high. However, the values are well below what would be expected by any rule of mixtures, this huge drop in mechanical properties is explained by the high amount of defects seen in the TEM analysis.

Figure 5.11 shows the fracture surface of the tested micropillars in order to further explain the changes of the fracture toughness observed for the different coatings. As it can be seen in figure 5.11(a), the surface of the TiN sample presents a fracture mode in which the cracks develop vertically along the testing direction. It can be noticed that the fracture at the bottom of the pillar propagates at the interface between the interlayer and the substrate. In the case of TiN(10)Ni (figure 5.11(b)) it is noticed that the surface is rough which confirms the fact that a refined structure was obtained, forming a nanocomposite structure. As it was observed for TiN, the fracture at the base of the pillars mostly occurs between the substrate and the interface. As it is observed in the figure, some cracks partially develop between the interlayer and the coating. For the thin TiN-Ni multilayer (figure 5.11(c)) the surface looks much more refined due to the presence of the thin Ni layers, but some traces of the columnar structure persist. It could be that, despite the forced renucleation, part of the columnar structure seen in pure TiN is carried through several layers since the Ni layers are incomplete. The microstructure that this coating presents resembles more the one shown by TiN(10)Ni than by TiN. In this case, the base of the pillar extended a bit into the Si and the crack propagated through it. The equivalent TiN(10)Ni-Ni coating presented in (figure 5.11(d)) combines a thin multilayer structure with a nanocomposite structure, which seems to result in much finer nanocomposite structure than the one obtained in the monolithic TiN(10)Ni due to the addition of thin Ni layers. Similar to the previous cases, the crack propagated between the interlayer and the substrate. Figure

5.11(e) shows the thick multilayer TiN-Ni tested micropillar which presents a very coarse microstructure and a lot of pores. Additionally, it presents a clear detachment between the coating and the interlayer. No pillar from 100TiN(10)Ni-60Ni broke completely and thus, no micrograph could be taken from its fracture surface.

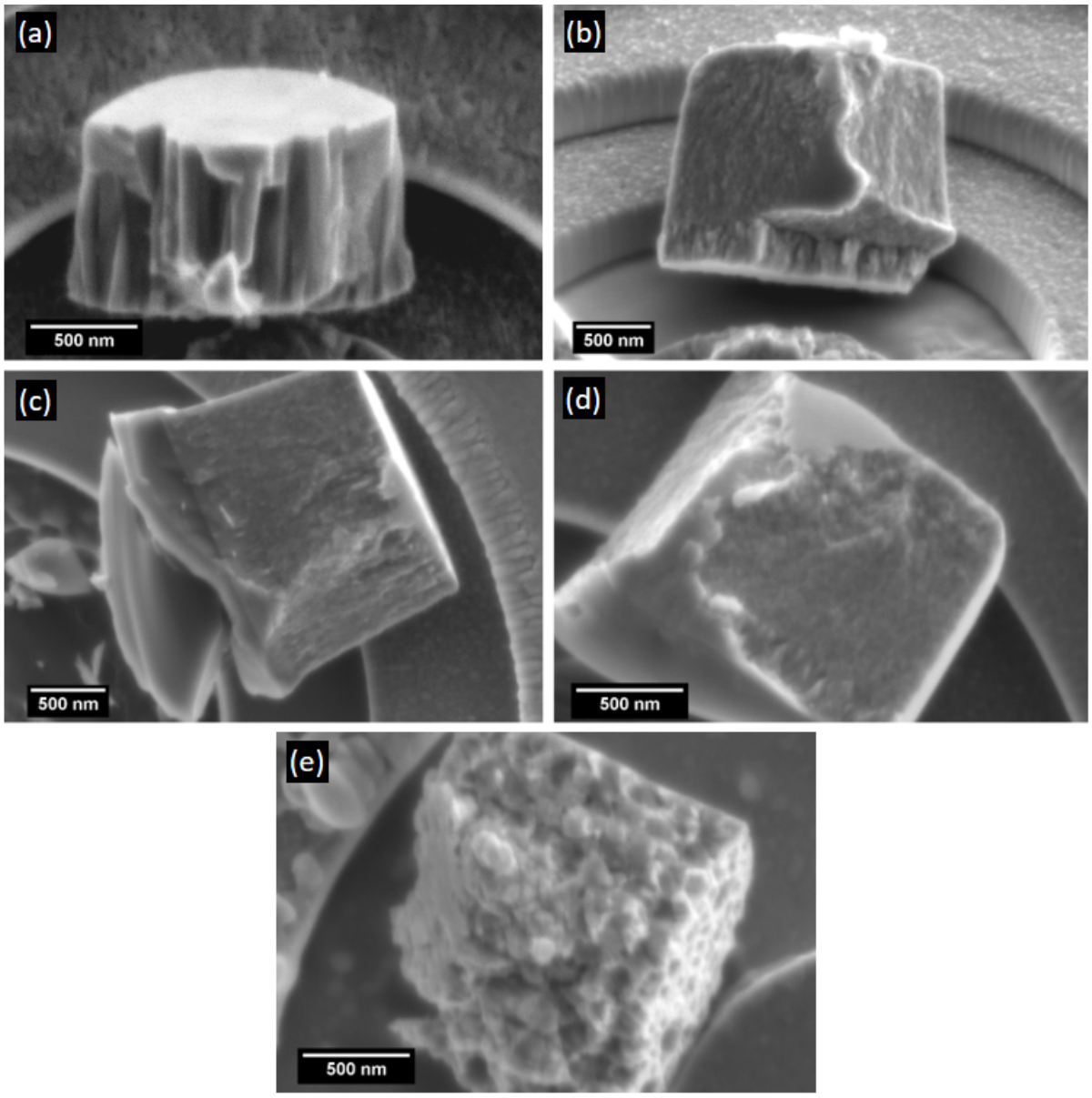


Figure 5.11: SEM images from tested micropillars of the monolithic reference samples and the multilayer coatings. (a) TiN, (b) TiN(10)Ni, (c) 10TiN-2Ni, (d) 10TiN(10)Ni-2Ni and (e) 100TiN-60Ni.

Based on the microstructures observed in TEM and the fracture surfaces from the tested pillars it can be hypothesized how the crack propagates through the material. In TiN it seems to happen along grain boundaries, thus the crack grows very easily across the material presenting very low toughness. Similarly, for TiN(10)Ni the crack probably develops through the grain boundaries as well, but since they are formed by nanograins and they present a tissue phase of Ni, the crack needs a higher load to propagate and has a more tortuous path to grow. As seen in its fracture surface, the roughness may be coming from the crack surrounding the grains while growing.

Regarding the thin multilayer coatings, the crack likely propagates through interfaces as well. Despite them being more compliant due to the Ni particles, they introduce a lot of interfaces which may deflect the crack along their interface with the hard phase increasing the tortuosity of the crack, leaving a rough fracture surface. Therefore, the coating shows a higher indentation depth before failure. Furthermore, the addition of the TiN(10)Ni nanocomposite structure to the multilayer, despite the fracture surface not showing any big difference, probably further inhibits the growth of the crack due to the reinforcement of the grain boundaries of the Ni tissue phase.

Due to the high thickness of the Ni layers, the thick multilayer coatings should present a more ductile behavior compared to the other samples. However, this cannot be observed in figure 5.11(e) due to the coarse microstructure and high amount of pores. Nevertheless, this difference in behavior can be noticed in the loading curves.

Figure 5.12 shows a representative loading curve up to the failure of the micropillars, except for 100TiN(10)Ni-60Ni for which none of the pillars broke catastrophically. The monolithic and the thin multilayer coatings present the same behavior in which the load increases up to failure while the thick layered coatings performed differently. Their loading curves, when getting closer to the maximum load, flatten before the pillar failure and presenting cycles in which the load oscillates.

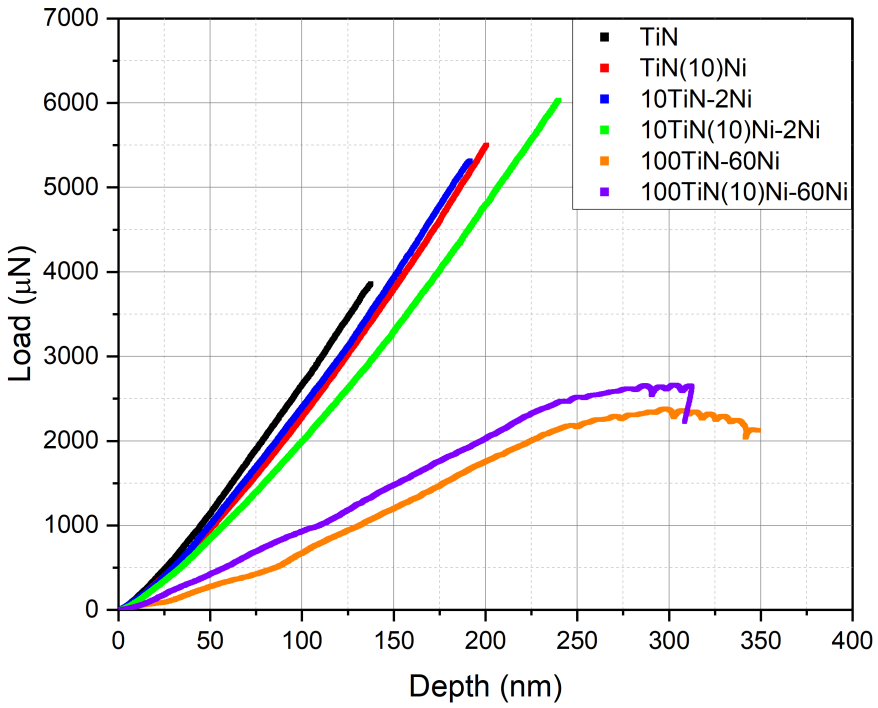


Figure 5.12: Representative load curves from micropillar splitting tests.

The main difference in the design of the coatings with respect to pure TiN is that the thick multilayer coating should present plastic behavior to improve the toughness of the coating while the TiN(10)Ni and the thin multilayer coatings are focused on increasing the toughness by delaying the catastrophic growth of the crack by increasing the length of its propagation path. However, after the deposition of the coatings there are other factors affecting the mechanical properties of the thick multilayer coatings compared to the rest. One of them is the surface morphology, because the thick multilayer coatings have a much rougher surface. The second is the relatively low adhesion of the coating to the interlayer that was observed in figure 5.11(e) due to the crack propagating in between them. Finally, the presence of defects in the form of pores seen in the TEM images (figures 5.7 and 5.8) The effect of the roughness can be observed at the very beginning where there is very high displacement of the curve compared to the load. After that, the pillar is loaded until the curve start to flatten when reaching the highest load to later present an increase in the displacement with relatively constant load. At this point the curve presents some "bumps", and their occurence could be related to the number

of bilayers of the coatings. This could mean that the Ni layers are acting as barriers slowing the crack growth while through the TiN layers it propagates easier. Due to the fact that these coatings present very high deformation and layers with distinct mechanical properties, pillar splitting may not be the most accurate test to evaluate their toughness. The reason behind is that the value of $\gamma$ used in equation 3.3 assumes a homogeneous coating along the thickness of the coating and it cannot be applied in this case. However, it still provides information about the crack propagation and the ductility of the Ni layers.

The thick multilayer samples are not tested any further due to the low mechanical properties and the high amount of pores seen in the TEM since it would not provide any useful information regarding the material.

### 5.5.2 High temperature behavior

Before analyzing the results of the experiments performed at high temperature it is important to remind that the state at which the samples were after being tested was very poor. All the coatings tested at high temperature showed partial to total delamination. Therefore, the results obtained at high temperatures, specially at 500°C, are not considered to be reliable since the effect of the substrate is likely very relevant. Therefore, results obtained at this temperature from the pillar splitting tests will be analyzed qualitatively and no nanoindentation measurement is considered valid.

Figure 5.13 presents the load-displacement curves obtained from micropillar splitting tests performed at 500°C. The samples tested were the monotlithic and the thin multilayer coatings. As it can be observed the behavior of TiN, TiN(10)Ni and 10TiN-2Ni shows an increasing fracture load respectively. The 10TiN(10)Ni-2Ni coating presents a completely different behavior since the load curve is continuous until the end of the load curve set for the test. This difference in the loading curves is related to a change from brittle to plastic behavior and makes pillar splitting experiments not an ideal method to measure fracture toughness.

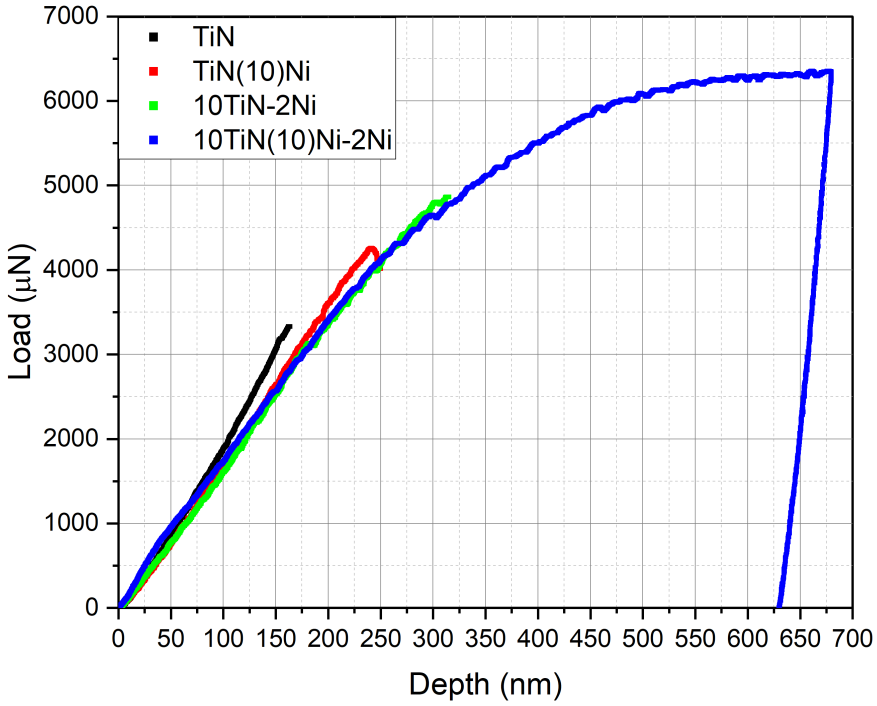


Figure 5.13: Representative load curves from micropillar splitting tests at 500°C.

As it was inferred by the loading curves, in figure 5.14 the tested pillars from the first three samples present a brittle fracture similar to what was observed at room temperature. However, for the 10TiN(10)Ni-2Ni the pillar is not fractured and presents a crack on the side. Looking at this crack, it is seen that the side of the pillar is curved and the parts into which the pillar normally would be divided are still joined together.

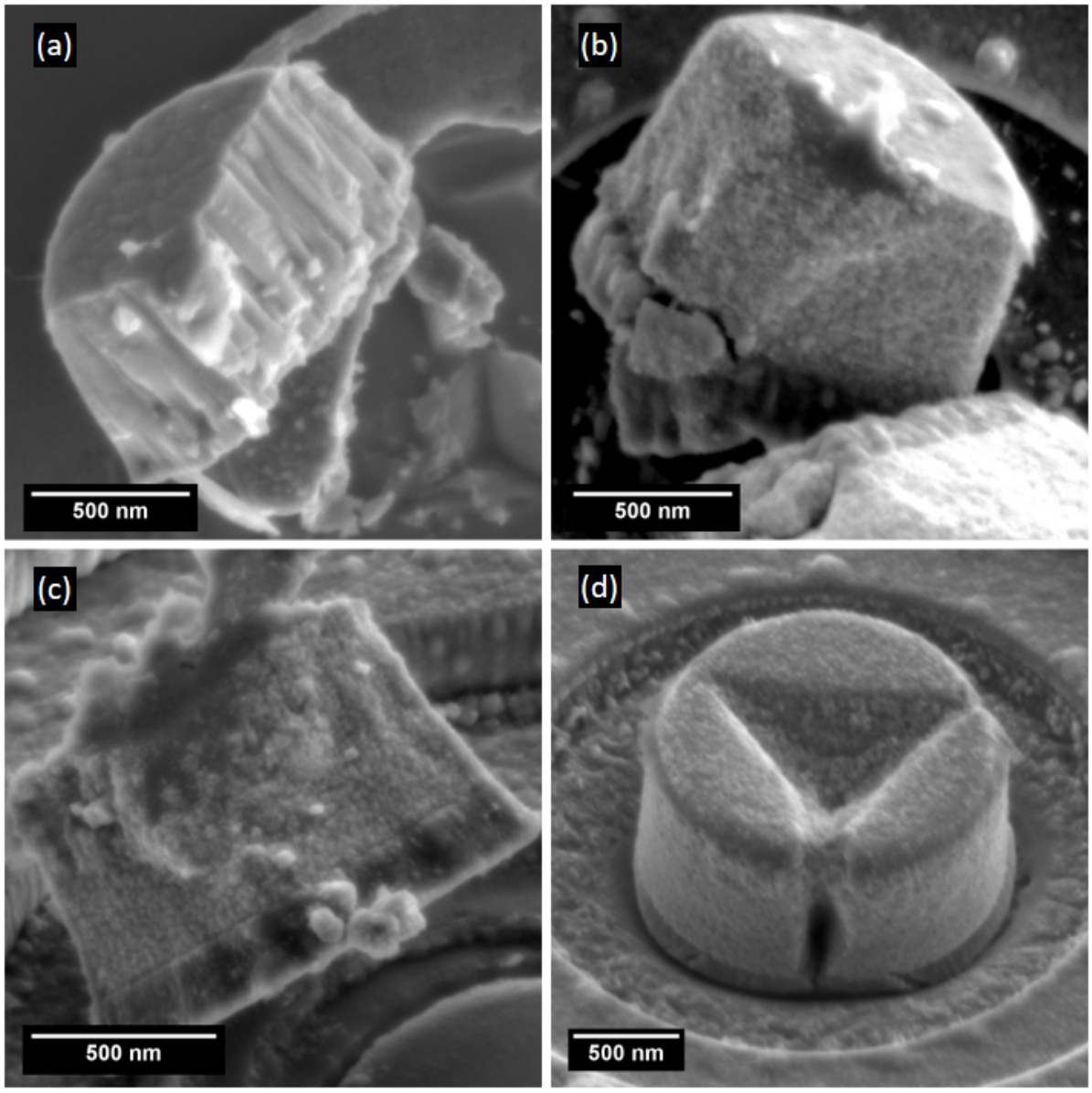


Figure 5.14: SEM images from micropillars of the monolithic reference samples and the multilayer coatings tested at 500°C. (a) TiN, (b) TiN(10)Ni, (c) 10TiN-2Ni and (d) 10TiN(10)Ni-2Ni.

Due to the change in behavior of the 10TiN(10)Ni-2Ni coating, the fracture model presented previously is no longer valid in this case, although it can still be applied to the other coatings. Based on figure 5.14 (d), the failure of the pillar seems to occur by compression rather than by crack initiation at the indentor tip and its growth. At this temperature the grains of TiN surrounded by the Ni tissue phase together with the Ni particles may have been able to accommodate the high deformation by grain sliding.

## 5.6 Discussion

This work shows it has been seen that the addition of toughening mechanisms at different scales mimicking the microstructure of nacre has proven to be an effective way to increase the toughness of the coating. Additionally, quantitative results from high temperature tests could still be analyze despite coating delamination. Among these results, it was observed a change in mechanical behavior of 10TiN(10)Ni from brittle to ductile. Moreover, different results for similar coatings to the ones obtained in the gradient coatings were observed, thus, these results need to be further discussed.

Concerning the phases that appear in the coatings, as it was seen in the high throughput analysis and figure 5.3, pure TiN presents a (111) $\delta$-TiN columnar structure result of a competitive growth between the different orientations. (111) $\delta$-TiN overlaps the rest of orientations since it presents the faster growth. Moreover, pure TiN coatings are subjected to relatively high compressive residual stresses. On the other hand, TiN(10)Ni presents a nanograin structure with an amorphous-like tissue phase of Ni which provided the coating with higher mechanical properties. Moroever, the nanocomposite TiN(10)Ni coatings also show a reduced level of compressive residual stresses with respect to pure TiN.

The hardness and elastic modulus of the thin multilayer coatings slightly dropped compared to the monolithic coatings but presented higher fracture toughness. However, the Ni layers were not continous, but tend to form elongated particles. The formation of this Ni distribution may be caused due to a combination of a relatively high substrate temperature and immiscibility of Ni in TiN. These two factors together might be helping Ni to agglomerate instead of staying as a uniform layer. The only differences in the Ni particle distribution between the TiN and the TiN(10)Ni multilayer coatings is that the particles seem to be a bit thicker. However this small difference is not expected to affect the mechanical properties.

Concerning the failure of the coatings, it seems clear that the failure mechanism for pure TiN is the growth of the crack generated by the indentor along the grain boundaries. This was seen in the fracture surface of the pillars previously and in figure 5.15, which shows a crack that grows surrounding the grains supports this argument.

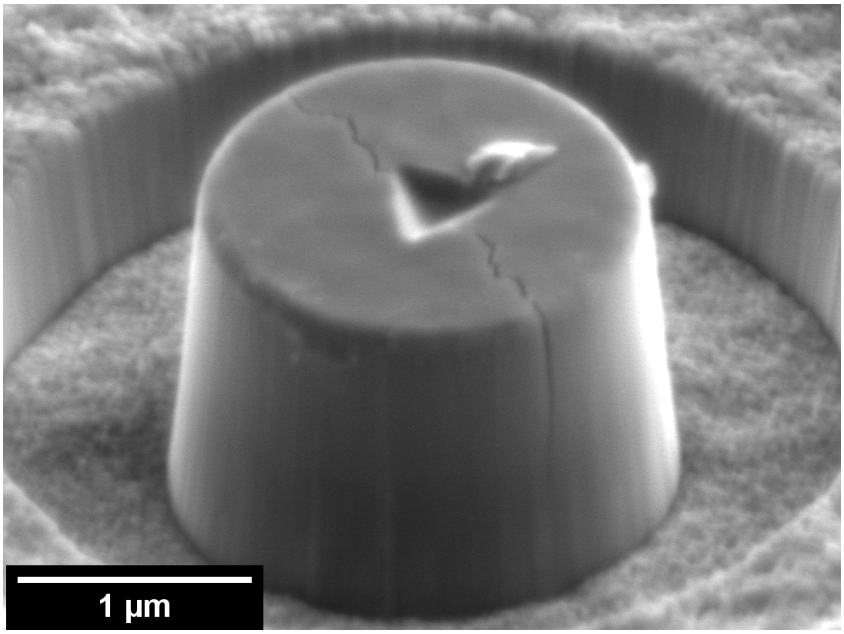


Figure 5.15: SEM image from pure TiN coating with crack growing.

If the crack propagation still occurs along the grain boundaries for the rest of the coatings, it could explain the differences in fracture toughness and the roughness of the fracture surface of the tested pillars. A columnar microstructure like TiN presents very low resistance to crack growth once it is nucleated. This is due to the propagation of the crack along the grain boundaries, which follows a straight line from the top of the coating to the substrate. However, TiN(10)Ni presenting a Ni tissue phase, makes it harder for the cracks to propagate, and a finer microstructure which increases the crack length presenting a more tortuous path. Both microstructural changes lead to an increment in toughness. The variations introduced in the coating by the multilayer system are the creation of a large amount of grain boundaries due to the refinement of the microstructure. This increases the tortuosity of the crack path increasing the fracture toughness. 10TiN-2Ni presents a high tortuous path, however, it does not present grain boundaries reinforced by an amorphous-like phase so the crack propagation along the TiN layers does not present very high resistance. Nevertheless, the addition on both mechanisms results a further increment of the fracture toughness.

Figure 5.16 shows a sketch of the crack propagation through the thin multilayer systems following the hypothesis explained before. Both thin multilayer microstructures are sketch as well as a likely crack propagation path (red dotted line). 10TiN-2Ni, figure 5.16 (a), shows that the TiN present a columnar structure which allows the crack to easily grow along the the grain boundaries only being slowed down by the Ni particles. However, the crack propagation path in 10TiN(10)Ni (figure 5.16 (b)) presents a higher tortuosity due to the nanocomposite structure. This allows the material to dissipate more energy before failure and thus presents a higher fracture toughness.

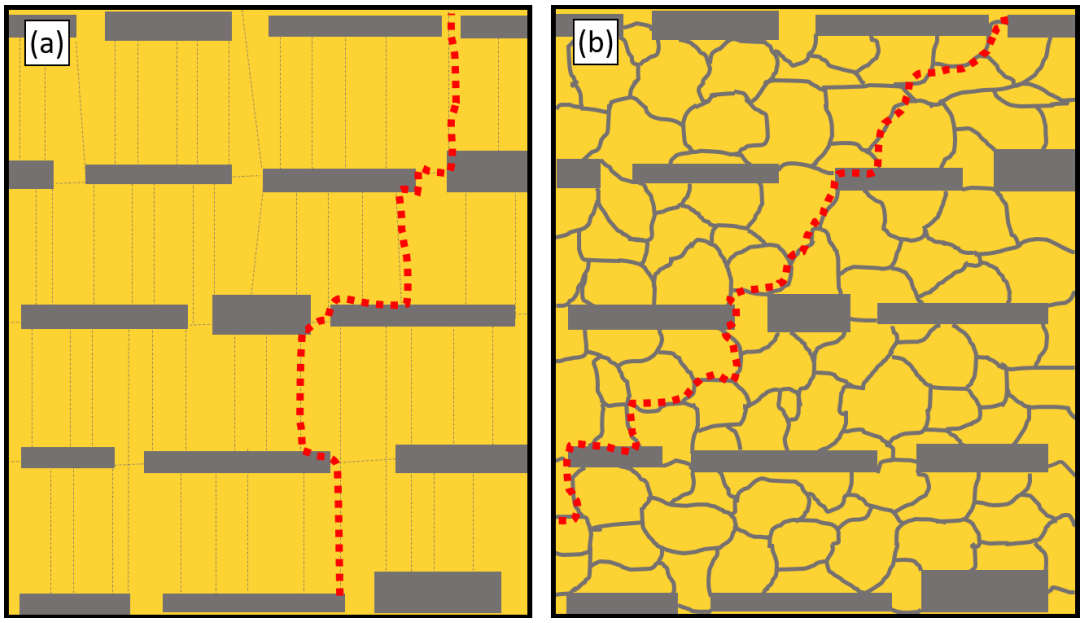


Figure 5.16: Crack path sketch of (a) 10TiN-2Ni and (b) 10TiN(10)Ni-2Ni.

In order to confirm this hypothesis, further examination of the crack propagation was performed. A lamella with a perpendicular view of a crack was prepared and examined by TEM. This crack was generated by loading the coating with a pyramidal diamond tip on a microhardness tester. Figure 5.17 (a) shows that the crack did not propagate perpendicular to the coating and that the crack grew forming steps at the layer and Ni particle interfaces. At a higher magnification ((b) and (c)) several lines are noticed, this is caused due to the thickness of the lamella and the crack surrounding grains and particles. Therefore, the material discontinuity is not always perpendicular to the TEM foil and multiple lines appear. The stair-like propagation together with the multiple lines observed imply that the crack propagation occurs through grain boundaries of both TiN(10)Ni grains and Ni particles, which supports the hypo-

thesis made before. This is also observed in figure 5.17 (d), which shows a BF STEM image from approximately the same area as (c). Due to the better composition contrast of STEM it is seen that the crack lines surround the Ni particles.

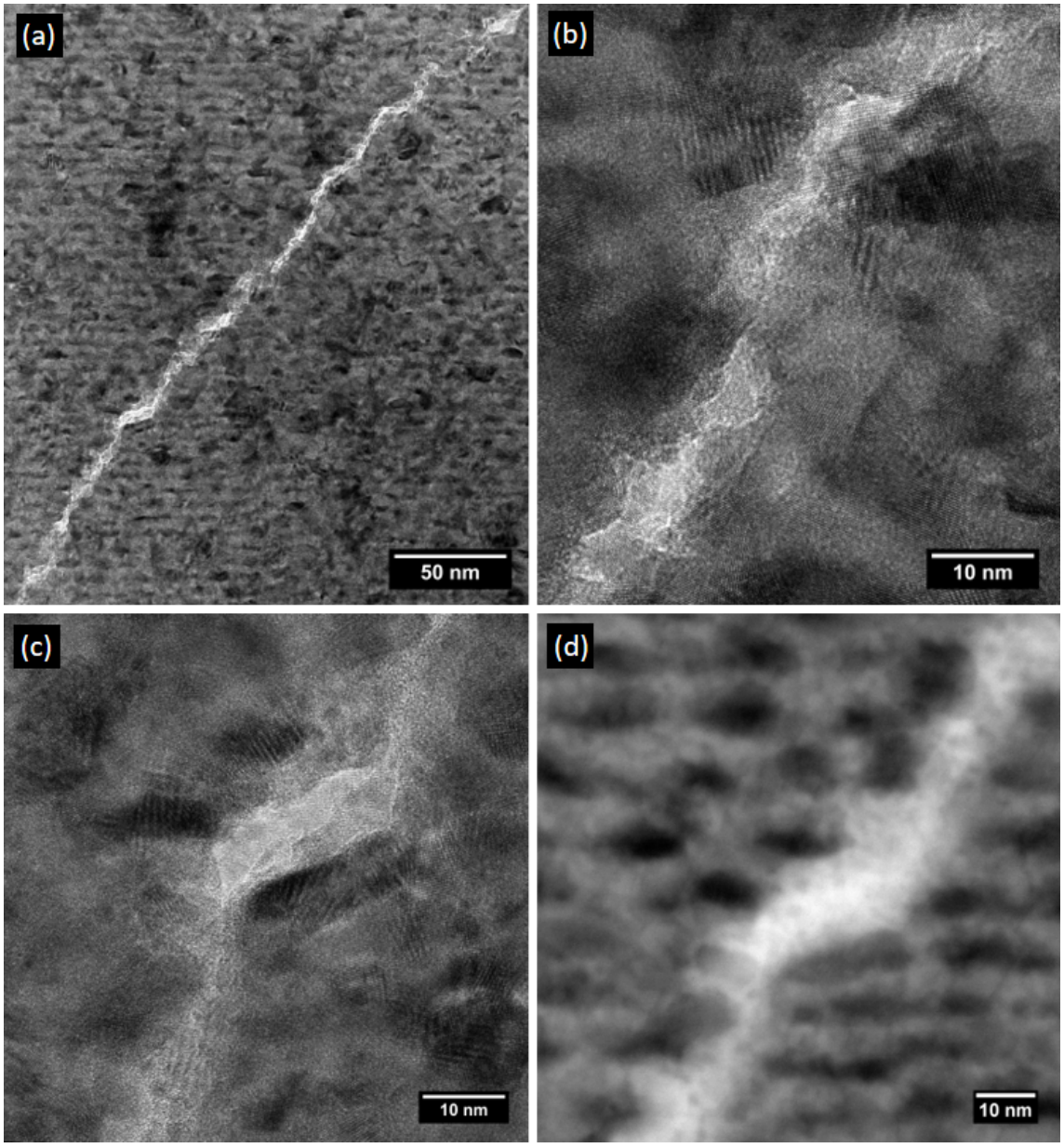


Figure 5.17: Crack propagated through 10TiN(10)Ni-2Ni: (a) BF TEM image, (b) and (c) HREM from the crack and (d) BF STEM image from same area as (c).

The thick multilayer coatings, despite not being able to accurately describe the mechanical properties of the coating due to the defects and the validity of the micro-pillar splitting test on ductile materials, could be analyzed through the loading curves. It was seen that the loading curve presented some bumps which could be related to the crack propagating through the Ni layers. Figure 5.18 shows a crack growing in a 100TiN-60Ni coating, it is observed that the crack nucleates by at the indenter corners and grows deflecting at the interfaces between layers. This propagation goes through the Ni layer, thick enough to present plastic behavior which can arrest the crack. As seen before, this resulted in the presence of bumps in the loading curve. A similar behavior was observed in the 100TiN(10)Ni-60Ni loading curves.

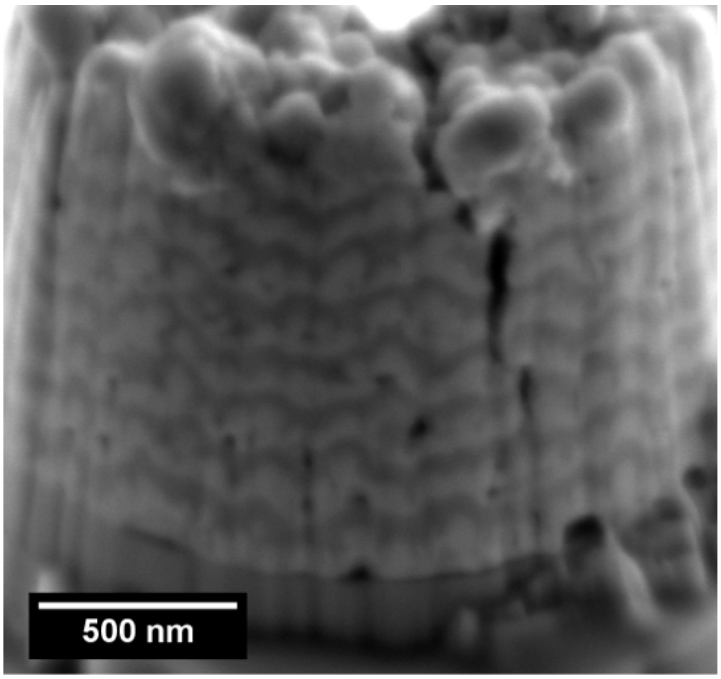


Figure 5.18: Tested 100TiN-60Ni pillar with crack growing.

The coating presented a lot of cracks, as seen in figures 5.7 and 5.8. This explains the lack of residual stresses of the thick multilayer coatings. The presence of cavities at the first Ni layer could be due to the directional deposition and the Ni agglomeration into particles which induces cavities due to shadowing effects. After the rough Ni layer, TiN deposits filling the spaces between the Ni grains leaving a smooth surface but maintaining the waviness from the first layer. The following layers are more or less parallel to the previous one. Nevertheless, the following layers are not able to adapt completely and voids are left in all layers, which also contribute to deteriorate the mechanical properties.

The serious adhesion problems and the large number of defects appeared with Ni layers thicker than 20 nm deposited from 200 to 400°C. Furthermore, these delamination issues seemed to be related to Ni layer thickness and deposition conditions. It was observed that depositing layers about 2-3nm thick using -100V bias and 400°C lead to the formation of inhomogeneous Ni layers formed by particles with sizes around 5-10nm. A larger bias voltage allowed the deposition of for thicker Ni layers without delamination, but the coatings still presented a large number of pores and very large roughness. Moreover, the grain size and the crystallinity of Ni grains was reduced. Therefore, it could be that the bigger grain size, usually related to a higher roughness, and the agglomeration of Ni over TiN could be making the amount and size of pores bigger losing adhesion and causing the coating to delaminate. Nevertheless, increasing the bias was not enough to produce a defect free coating. Therefore, the use of Ni to introduce ductility in the form of thick layers is discouraged.

In order to further analyze the change in mechanical behavior of 10TiN-2Ni and 10TiN(10)Ni-2Ni at high temperature, from brittle to ductile, the microstructure of the as-deposited and heat treated coating is analyzed in figure 5.19 and 5.20. The ED patterns (figure 5.19 (a) and (b)) show that the rings are formed by more defined spots in the heat treated than the as-deposited coatings which could be related to an increase of the crystallinity. Looking at the HAADF images (figure 5.19(c) and (d)) and the EDS maps ((e) and (f)) it is noticed that the distribution and size of the Ni particles have barely changed.

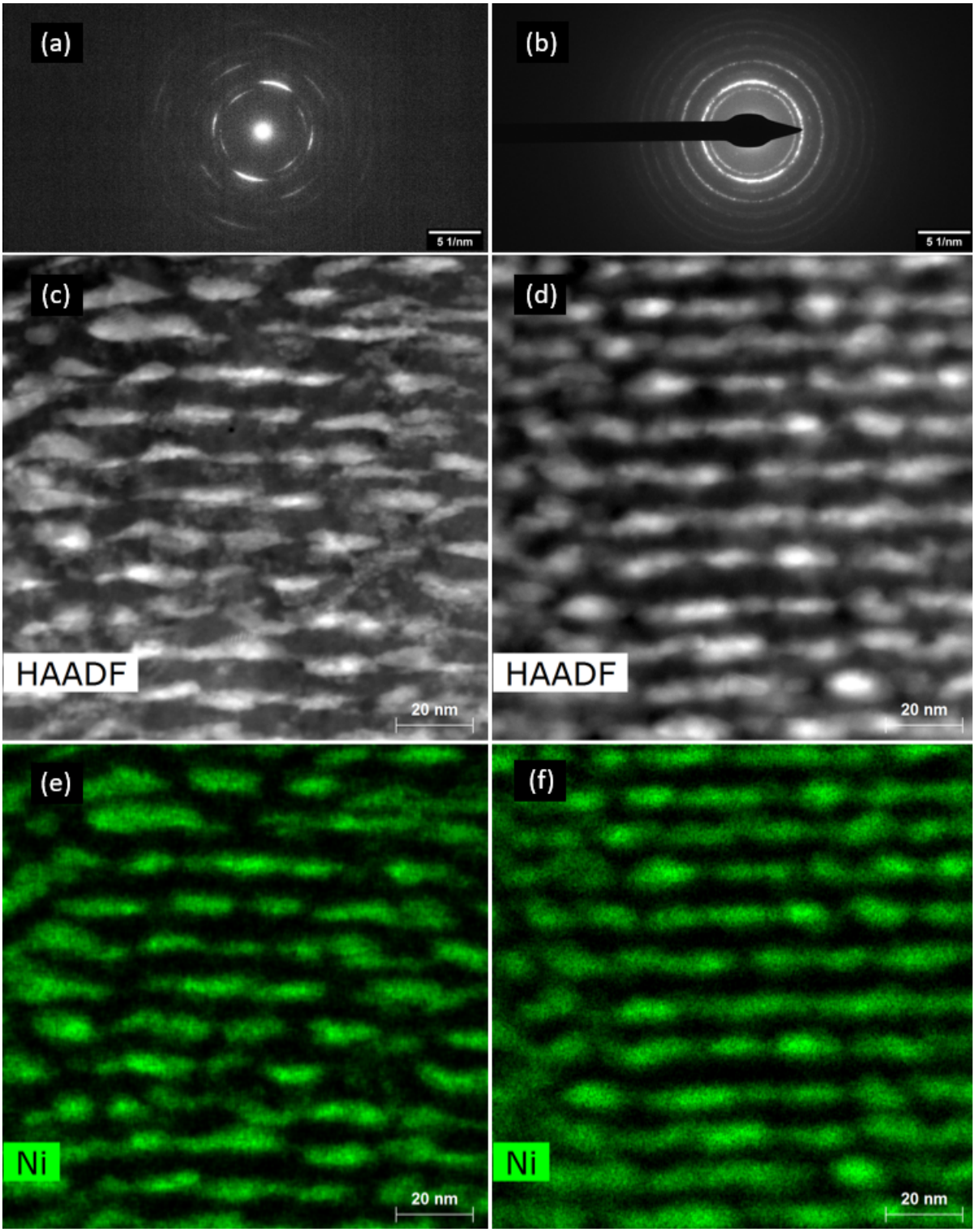


Figure 5.19: TEM images from as-deposited and heat treated 10TiN-2Ni. (a) and (b) DPs; (c) and (d) HAADF and; (e) and (f) EDX maps of the corresponding area showing the Ni distribution.

As it was observed for 10TiN-2Ni, the ED patterns (figure 5.20(a) and (b)) show that the rings are formed by more defined spots in the heat treated than the as-deposited coatings which could be related to an increase of crystallinity. Comparing the HAADF images (figure 5.20(c) and (d)) and the Ni EDX map (figure 5.20(e) and (f)) of the same area it is noticed that the Ni particles are bigger and more defined. This could be related to a further diffusion of Ni from the grain boundaries to the particles in contrast to 10TiN-2Ni where all Ni was already forming particles and its behavior did not change. At 500°C the Ni particles become softer and behave in a more ductile manner, which might cause the transition together with the higher Ni volume fraction. The TiN crystallites would be able to slide over Ni and thus, the coating is able to deform plastically. However, a certain volume fraction of pure Ni must be necessary with the distribution presented in the coatings for this phenomenon to occur.

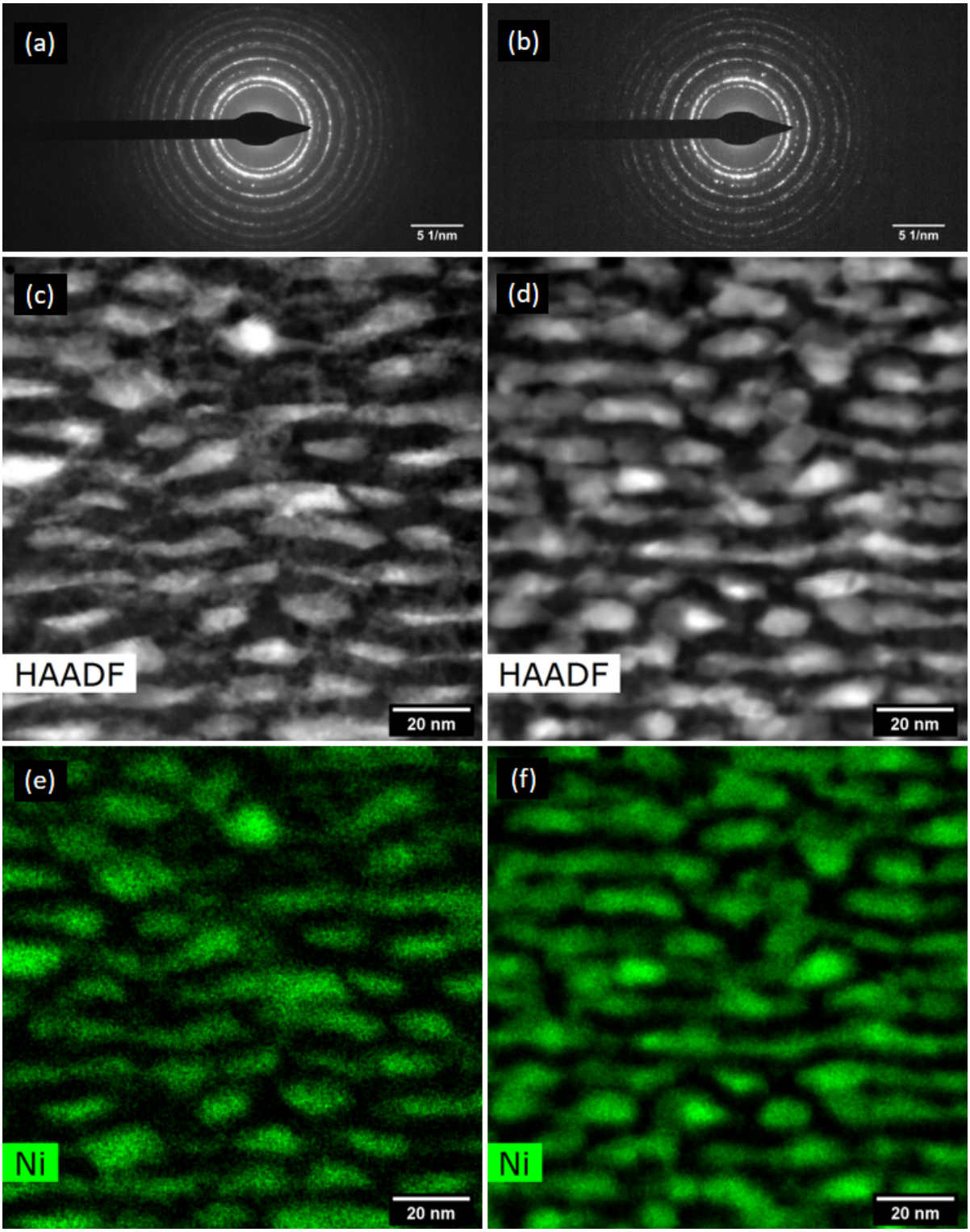


Figure 5.20: TEM images from as-deposited and heat treated 10TiN(10)Ni-2Ni. (a) and (b) DPs; (c) and (d) HAADF and; (e) and (f) EDX maps of the corresponding area showing the Ni distribution.

# Chapter 6

# Conclusions

The objectives of this investigation is the development of coating architectures that maximize fracture toughness, without sacrificing hardness by the use of hierarchical build-up of microstructures at different length scales. Moreover, the study takes advantage of using high throughput methodologies to fully explore the coating architecture based on the deposition of coatings with variable composition and/or microstructure and their characterization based on advanced micromechanical testing techniques.

During the initial phase of the project, the effort was focused on the development of coatings exploiting the benefit of nanocomposite type microstructures, based on the Ti-N-Ni system. A nanocomposite coating is expected to be composed of nanocrystalline domains of a hard phase (in this case, TiN) with a continuous matrix of a second phase that provides both hardness and toughness. This type of microstructure can be found in Ti-N-Si coatings, for which it has been demonstrated that, to maximize hardness, the continuous matrix of $SiN_x$ has to be present in a precise amount so it forms a thin tissue of amorphous $SiN_x$ around the TiN nanograins. In our case, Ni was proposed as the continuous matrix, in substitution of Si, with the objective of providing a metallic phase that can provide more toughening, but maintaining stability at high temperatures.

Firstly, a high throughput methodology has been developed to produce coatings of Ti-Ni-N, with a gradient in Ni content, ranging from 0 to 20%. The coatings were produced by reactive magnetron sputtering using two targets of Ti and Ni, in an Ar-$N_2$ atmosphere. The gradient in composition was achieved by mounting a long strip of Si on a stationary substrate holder, in such a way that the deposition rates of TiN and Ni changed continuously along the length of the substrate. The objective was successfully achieved although with a reduced thickness uniformity due to the non-rotating substrate holder. Moreover, in order to avoid delamination during deposition of the coatings, it was crucial to use a long thermal stabilization step and to introduce a Ti interlayer before the deposition of the final coating.

The microstructure and mechanical properties of the Ti-N-Ni coatings were analyzed as a function of Ni content, reaching the following conclusions:

- The preferred growth orientation changed from TiN(111) to TiN(200) as the Ni content increased up to 7.6-15 at.% Ni. The stoichiometry of the TiN phase is not affected in this composition range, maintaining a Ti/N ratio close to 1. For higher Ni contents, the texture was more random, the Ti/N ratio decreases, and the lattice parameter of the TiN phase gets reduced.

- No presence of a distinct crystalline Ni phase was found in the as-deposited coatings, implying that some Ni might be dissolved in the TiN lattice, segregated as an amorphous-like phase or both.

- The elastic modulus of the Ti-N-Ni coatings remains constant for Ni contents up to 13 at.% Ni, implying that the coatings are primarily formed by the TiN phase, and enforcing the conclusion that the Ni might be dissolved in the TiN lattice or segregated as an amorphous-like phase, but without affecting its bonding strongly. Higher amounts of Ni, however lead to a drastic reduction in the elastic modulus, as the TiN phase becomes Ti deficient.

- The most interesting effect of the Ni addition in the composition range between 0 and 13 at.% was found on the hardness and fracture toughness. They followed a similar trend, with both of them increasing to a maximum for a Ni content of 9.5 at.%, after which

they decrease again for larger Ni contents. The maximum hardness and toughness at room temperature were 32 GPa and 4.8 MPa $m^{1/2}$ respectively.

- The microstructure of the coating with increasing Ni content evolved from a (111) columnar microstructure for pure $\delta$-TiN to (200) oriented $\delta$-TiN grains with an amorphous-like Ni tissue phase at around 10 at.% Ni. The further addition of Ni made the microstructure become randomly oriented with fine columnar microstructure with Ni islands and voids between grains.

- Based on the XRD and TEM observations, the peak in hardness and toughness can be attributed to the development of a nanocomposite type microstructure, for which the TiN nanograins adopt a TiN(200) preferred growth orientation and some Ni is partially segregated in the grain boundaries as an amorphous-like phase, while the rest remains dissolved within the TiN phase. This microstructure seems responsible for partially reducing residual stresses.

- Upon annealing, the integrity of the coatings for Ni contents higher than 13 at.% Ni is compromised. For lower Ni contents, the coatings survive the annealing process with a little delamination, but the Ni phase crystallizes. As a consequence, the elastic modulus drops with the Ni content.

- High temperature indentation tests revealed that TiN with around 10% Ni presents superior hardness over pure TiN at 350°C. However, at 500°C this difference is lost since TiN/Ni hardness decreased to 11 GPa while the hardness of pure TiN dropped below 10 GPa. This difference in their mechanical properties is likely due to the difference in microstructure.

Once the effect of Ni in the TiN phase was fully understood, a multilayer structure is implemented with two different layer thickness. On the one hand, thin layers of Ni were deposited in order to increase the amount of interfaces and on the other, thick layers so some plasticity is introduced. Both systems were deposited using TiN and TiN/Ni as the hard phase. However, the thin multilayers do not present homogeneous Ni layers but unconnected platelets/particles. The thick multilayers presented a lot of problems to avoid its delamination while making them and showed a lot of defects. From the characterization and analysis of the monolithic TiN, TiN(10)Ni and the multilayer coatings can be concluded:

- The use of a multilayer structure composed of pure 10 nm thick layers of pure TiN alternated with 2 nm thick amorphous-like Ni layers results in a similar enhancement in fracture toughness than the nanocomposite approach. These layers are responsible for the suppression of columnar growth, since the TiN layers are forced to renucleate after each Ni layer, explaining the change in crystalline orientation and the increase fracture toughness.

- The formation of Ni particles in the thin multilayer coating seems to be related to the inmiscibility of Ni in TiN and high mobility of Ni atoms at the deposition temperature. The latter becomes more clear in the formation of the big equiaxial grains in the thick multilayer coatings.

- A coating with a hierarchical microstructure composed of 10 nm thick TiN(10)Ni layers and 2 nm thick amorphous-like Ni layers was successfully produced. Such microstructure resembles that of nacre and confirming the initial hypothesis of this work, results in a substantial increase in fracture toughness, from 3.5 to 5.5. MPa $m^{1/2}$, without a significant drop in hardness. Several mechanisms were found to be responsible for this enhancement, including the strengthening of the grain boundaries by the Ni thin tissue surrounding the TiN nanocrystals and the crack arrest and crack deflection at the Ni particle interlayers.

- The microstructural change from the columnar structure of pure TiN to nanocomposite with the Ni particles does not change the crack growth mechanism, the crack still propagates along grain boundaries. However, the grain refinement, together with the

strengthening of the grain boundaries by the amorphous-like Ni tissue contribute to a considerable increase in the toughness of the coatings.

- Such hierarchical microstructure showed a very ductile behavior at 500 °C, as opposed to the pure TiN, the nanocomposite TiN(10)Ni and the TiN/Ni multilayers. It is speculated that the ductile behavior was the consequence of the formation of a large number of Ni islands due to the segregation of Ni out of the TiN(10)Ni layers, which compromises the high temperature stability of the coatings.

- Thick multilayer coatings presented a more ductile behavior due to the plasticity of Ni layer, however it was found that the integrity of the coating is lost when depositing Ni layers of 20nm or higher.

# Chapter 7

# Future work

After all the work that has been presented in this work, further study into these materials can be performed as a direct continuation and future research lines are proposed following the principles learnt in this project.

- Deposition of thin multilayer coatings using a lower deposition temperature. It was observed that Ni layers formed aligned Ni particles result of the immiscibility and high mobility at the chosen temperature. Additionally, it was noticed that cracks were propagating surrounding the Ni layers. Therefore, if the Ni was distributed as a homogeneous layer it could be having a stronger effect on the toughness by elongating the crack path and deflecting the crack more effectively. This may be achieved reducing the deposition temperature so Ni may not be able to diffuse into forming particles.

- Since one of the most typical application of these coatings is to protect machining tools, studying their behavior directly with wear tests could provide valuable information of the mechanical behavior of these coatings.

- Due to the problems experience with temperature, other material systems could benefit from this microstructure in which Ni is substituted by a ceramic phase like SiN. Coatings like MeSiN present higher temperature stability and very high hardness but very low toughness, thus the use of nacre's hierarchical microstructure (MeSiN-SiN) could benefit them. Elements like B or C could also be added in order to form other hard phases.

- By using these elements, a microstructure composed of grains of different sizes and phases surrounded by a tissue phase, being a more complex nanocomposite structure that emulates the structure of concrete at a nanoscale.

# References


[1] H. Xu, Y. Du, Z. Yuan and H. Chen, "Nitrogen – Nickel – Titanium," pp. 406–414,

[2] W. Li, P. Liu, S. Zhao, K. Zhang, F. Ma, X. Liu, X. Chen and D. He, "Microstructural evolution, mechanical properties and strengthening mechanism of TiN/Ni nanocomposite film," *Journal of Alloys and Compounds*, vol. 691, no. 2017, pp. 159–164, 2017.

[3] Y. X. Wang, S. Zhang, J. W. Lee, W. S. Lew and B. Li, "Influence of bias voltage on the hardness and toughness of CrAlN coatings via magnetron sputtering," *Surface and Coatings Technology*, vol. 206, no. 24, pp. 5103–5107, 2012.

[4] X. Li, Z. H. Xu and R. Wang, "In situ observation of nanograin rotation and deformation in nacre," *Nano Letters*, vol. 6, no. 10, pp. 2301–2304, Oct. 2006.

[5] J. Sun and B. Bhushan, "Hierarchical structure and mechanical properties of nacre: A review," *RSC Advances*, vol. 2, no. 20, pp. 7617–7632, Sep. 2012.

[6] Albert Yu-Min Lin, "STRUCTURAL AND FUNCTIONAL BIOLOGICAL MATERIALS: ABALONE NACRE, SHARP MATERIALS, AND ABALONE FOOT ADHESION," Ph.D. dissertation, 2008.

[7] A. P. Jackson, J. F. V. Vincent and R. M. Turner, "The mechanical design of nacre," *Proc. R. Soc. Lond. B*, vol. 234, pp. 415–440, 1988.

[8] J.-Y. Sun and J. Tong, "Fracture Toughness Properties of Three Different Biomaterials Measured by Nanoindentation," Tech. Rep., 2007, pp. 11–17.

[9] Y. Xi and S. Zhang, "Toward hard yet tough ceramic coatings," *Surface & Coatings Technology*, vol. 258, pp. 1–16, 2014.

[10] P. H. Mayrhofer, C. Mitterer, L. Hultman and H. Clemens, "Microstructural design of hard coatings," *Progress in Materials Science*, vol. 51, no. 8, pp. 1032–1114, 2006.

[11] C. Wang, K. Shi, C. Gross, J. M. Pureza, M. de Mesquita Lacerda and Y. W. Chung, "Toughness enhancement of nanostructured hard coatings: Design strategies and toughness measurement techniques," *Surface and Coatings Technology*, vol. 257, pp. 206–212, 2014.

[12] H. Holleck, "Material selection for hard coatings," *Journal of Vacuum Science & Technology A*, vol. 4, no. 6, pp. 2661–2669, 1986.

[13] E. O. Hall, "The deformation and ageing of mild steel: Iii discussion of results," *Proceedings of the Physical Society. Section B*, vol. 64, no. 9, p. 747, 1951.

[14] N. J. Petch, "The cleavage strength of polycrystals," *Journal of the Iron and Steel Institute*, vol. 174, pp. 25–28, 1953.

[15] J. H. Schneibel and M. Heilmaier, "Hall-petch breakdown at elevated temperatures," *Materials Transactions*, vol. 55, no. 1, pp. 44–51, 2015.

[16] J. Musil, "Hard nanocomposite coatings: Thermal stability, oxidation resistance and toughness," *Surface and Coatings Technology*, vol. 207, pp. 50–65, 2012.

[17] S. Veprek and S. Reiprich, "A concept for the design of novel superhard coatings," *Thin Solid Films*, vol. 268, pp. 64–71, 1995.

[18] M. Diserens, J. Patscheider and F. Lévy, "Mechanical properties and oxidation resistance of nanocomposite TiN–SiNx physical-vapor-deposited thin films," *Surface and Coatings Technology*, vol. 120-121, pp. 158–165, 1999.

[19] M. Mišina, J. Musil and S. Kadlec, "Composite TiN-Ni thin films deposited by reactive magnetron sputter ion-plating," *Surface and Coatings Technology*, vol. 110, no. 3, pp. 168–172, 1998.

[20] J. Musil, H. Hrubý, P. Zeman, H. Zeman, R. Čerstvý, P. H. Mayrhofer and C. Mitterer, "Hard and superhard nanocomposite Al-Cu-N films prepared by magnetron sputtering," *Surface and Coatings Technology*, vol. 142-144, pp. 603–609, 2001.

[21] J. Šůna, J. Musil, V. Ondok and J. G. Han, "Enhanced hardness in sputtered Zr-Ni-N films," *Surface and Coatings Technology*, vol. 200, no. 22-23 SPEC. ISS. Pp. 6293–6297, 2006.

[22] J. Musil, P. Zeman, H. Hrubý and P. H. Mayrhofer, "ZrN/Cu nanocomposite film - A novel superhard material," *Surface and Coatings Technology*, vol. 120-121, pp. 179–183, 1999.

[23] J.S.Koehler, "Attempt to Design a Strong Solid," vol. 379, no. 1950, 1968.

[24] M. Kato, T. Mori and L. H. Schwartz, "Hardening by spinodal modulated structure," *Computer Science and Communications Dictionary*, p. 1036, 1979.

[25] U. Helmersson, S. Todorova, S. A. Barnett, J. E. Sundgren, L. C. Markert and J. E. Greene, "Growth of single crystal TiN/VN strained layer superlattices with extremely high mechanical hardness," *Journal of Applied Physics*, vol. 62, no. 2, pp. 481–484, 1987.

[26] H. C. Barshilia and K. S. Rajam, "Structure and properties of reactive DC magnetron sputtered TiN/NbN hard superlattices," *Surface and Coatings Technology*, vol. 183, no. 2-3, pp. 174–183, 2004.

[27] S. H. Tsai and J. G. Duh, "Microstructure and mechanical properties of CrAlN/SiNxnanostructure multilayered coatings," *Thin Solid Films*, vol. 518, no. 5, pp. 1480–1483, 2009.

[28] G. Zhang, T. Fan, T. Wang and H. Chen, "Microstructure, mechanical and tribological behavior of MoN x/SiNx multilayer coatings prepared by magnetron sputtering," *Applied Surface Science*, vol. 274, pp. 231–236, 2013.

[29] M. Stueber, H. Holleck, H. Leiste, K. Seemann, S. Ulrich and C. Ziebert, "Concepts for the design of advanced nanoscale PVD multilayer protective thin films," *Journal of Alloys and Compounds*, vol. 483, no. 1-2, pp. 321–333, 2009.

[30] J. H. Hsieh, P. C. Liu, C. Li, M. K. Cheng and S. Y. Chang, "Mechanical properties of TaN-Cu nanocomposite thin films," *Surface and Coatings Technology*, vol. 202, no. 22-23, pp. 5530–5534, 2008.

[31] Y. X. Wang, S. Zhang, J. W. Lee, W. S. Lew and B. Li, "Toughening effect of Ni on nc-CrAlN/a-SiNx hard nanocomposite," *Applied Surface Science*, vol. 265, pp. 418–423, 2013.

[32] B. Basu, T. Venkateswaran and D.-Y. Kim, "Microstructure and properties of spark plasma-sintered $ZrO_2$/$ZrB_2$ nanoceramic composites," *Journal of the American Ceramic Society*, vol. 89, no. 8, pp. 2405–2412,

[33] D. E. Ruddell, B. R. Stoner and J. Y. Thompson, "The effect of deposition parameters on the properties of yttria-stabilized zirconia thin films," *Thin Solid Films*, vol. 445, no. 1, pp. 14–19, 2003.

[34] M. Sharear, P. Munroe, Z. Zhou and Z. Xie, "Scratch adhesion and tribological behaviour of graded Cr / CrN / CrTiN coatings synthesized by closed- fi eld unbalanced magnetron sputtering," *Wear*, vol. 380-381, pp. 163–175, 2017.

[35] J. Lin, B. Mishra, S. Myers, P. Ried and J. J. Moore, "The development of a nanostructured, graded multilayer cr-cr x n y -cr1x al x n coating produced by pulsed closed field unbalanced magnetron sputtering (p-cfubms) for use in aluminum pressure die casting dies," *Journal of Nanoscience and Nanotechnology*, vol. 9, no. 6, pp. 3514–3523, 2009.

[36] Y. X. Wang, S. Zhang, J. W. Lee, W. S. Lew, D. Sun and B. Li, "Toward hard yet tough CrAlSiN coatings via compositional grading," *Surface and Coatings Technology*, vol. 231, pp. 346–352, 2013.

[37] R. Daniel, M. Meindlhumer, J. Zalesak, B. Sartory, A. Zeilinger, C. Mitterer and J. Keckes, "Fracture toughness enhancement of brittle nanostructured materials by spatial heterogeneity: A micromechanical proof for CrN/Cr and TiN/SiOxmultilayers," *Materials and Design*, vol. 104, pp. 227–234, 2016.

[38] R. Hahn, M. Bartosik, R. Soler, C. Kirchlechner, G. Dehm and P. H. Mayrhofer, "Superlattice effect for enhanced fracture toughness of hard coatings," *Scripta Materialia*, vol. 124, pp. 67–70, 2016.

[39] W. Li, P. Liu, Y. Zhao, F. Ma, X. Liu, X. Chen and D. He, "New understanding of hardening mechanism of tin/sinx-based nanocomposite films," *Nanoscale Research Letters*, vol. 8, pp. 1–7, 1 2013.

[40] J. Musil, P. Karvánková and J. Kasl, "Hard and superhard Zr-Ni-N nanocomposite films," *Surface and Coatings Technology*, vol. 139, no. 1, pp. 101–109, 2001.

[41] Y. J. Kim, T. J. Byun, H. Y. Lee and J. G. Han, "Effect of bilayer period on CrN/Cu nanoscale multilayer thin films," *Surface and Coatings Technology*, vol. 202, no. 22-23, pp. 5508–5511, 2008.

[42] T. Vieira, J. Castanho and C. Louro, "Hard Coatings Based on Metal Nitrides , Metal Carbides and Nanocomposite Materials : PVD Process and Properties," in *Materials Surface Processing*, 2006.

[43] P. Wiecinski, J. Smolik, H. Garbacz and K. J. Kurzydlowski, "Failure and deformation mechanisms during indentation in nanostructured Cr / CrN multilayer coatings," *Surface & Coatings Technology*, vol. 240, pp. 23–31, 2014.

[44] A. Sharma, S. Mohan and S. Suwas, "The influence of deposition temperature on the structure, microstructure, morphology and magnetic properties of sputter deposited nickel thin films," *Thin Solid Films*, vol. 619, pp. 91–101, 2016.

[45] F. Ye, Z. Zhuying, Z. Guoqing and Y. Fujia, "Cross sections for 165º backscattering of 2.0-9.0 MeV He ions from nitrogen," *Nuclear Instruments and Methods in Physics Research*, vol. 94, pp. 11–14, 1994.

[46] J. García López, F. J. Ager, M. B. Rank, F. J. Madrigal, M. A. Ontalba, M. A. Respaldiza and M. D. Ynsa, "CNA: the first accelerator-based IBA facility in Spain," *Nuclear Instruments and Methods in Physics Research, Section B: Beam Interactions with Materials and Atoms*, vol. 161, pp. 1137–1142, 2000.

[47] M.Mayer, "{SIMNRA}, Version 6.02," *Max Planck Institut für Plasmaphysik*,

[48] A. M. Korsunsky, M. Sebastiani and E. Bemporad, "Residual stress evaluation at the micrometer scale: Analysis of thin coatings by FIB milling and digital image correlation," *Surface and Coatings Technology*, vol. 205, no. 7, pp. 2393–2403, 2010.

[49] M. R. Ardigo, M. Ahmed and A. Besnard, "Stoney formula: Investigation of curvature measurements by optical profilometer," *Advanced Materials Research*, vol. 996, pp. 361–366, 2014.

[50] G. M. Pharr, W. C. Oliver, G. M. Pharr, W. C. Oliver and G. M. Pharr, "An improved technique for determining hardness and elastic modulus using load and displacement sensing indentation experiments," *Journal of Materials Research*, vol. 7, no. 6, pp. 1564–1583, 1992.

[51] M. Sebastiani, K. E. Johanns, E. G. Herbert, F. Carassiti and G. M. Pharr, "A novel pillar indentation splitting test for measuring fracture toughness of thin ceramic coatings," *Philosophical Magazine*, vol. 95, no. 16-18, pp. 1928–1944, 2015.

[52] M. Ghidelli, M. Sebastiani, K. E. Johanns and G. M. Pharr, "Effects of indenter angle on micro-scale fracture toughness measurement by pillar splitting," *Journal of the American Ceramic Society*, vol. 100, no. 12, pp. 5731–5738, 2017.

[53] I. Petrov, P. B. Barna, L. Hultman and J. E. Greene, "Microstructural evolution during film growth," *Journal of Vacuum Science & Technology A: Vacuum, Surfaces, and Films*, vol. 21, no. 5, S117–S128, 2003.

[54] H. A. Wriedt and J. L. Murray, "The N-Ti (Nitrogen-Titanium) system," *Bulletin of Alloy Phase Diagrams*, vol. 8, no. 4, pp. 378–388, 1987.

[55] G. Abadias, "Stress and preferred orientation in nitride-based PVD coatings," *Surface and Coatings Technology*, vol. 202, no. 11, pp. 2223–2235, 2008.

[56] A. Mehta and P. J. Heaney, "Structure of La2NiO4.18," *Physical Review B*, vol. 49, no. 1, pp. 563–571, 1994.

[57] B. H. Park, Y. I. Kim and K. H. Kim, "Effect of silicon addition on microstructure and mechanical property of titanium nitride film prepared by plasma-assisted chemical vapor deposition," *Thin Solid Films*, vol. 348, no. 1, pp. 210–214, 1999.

[58] S. Zhang, D. Sun, Y. Fu and H. Du, "Toughening of hard nanostructural thin films: A critical review," *Surface and Coatings Technology*, vol. 198, no. 1-3 SPEC. ISS. Pp. 2–8, 2005.

[59] A. Akbari, C. Templier, M. F. Beaufort, D. Eyidi and J. P. Riviere, "Ion beam assisted deposition of TiN-Ni nanocomposite coatings," *Surface and Coatings Technology*, vol. 206, no. 5, pp. 972–975, 2011.

[60] J. A. Thornton, “Influence of substrate temperature and deposition rate on structure of thicksputtered Cu coatings,” *J. Vac. Sci. Technol.*, vol. 12, no. 4, pp. 830–835, 1975.

[61] A. Akbari, J. P. Riviere, C. Templier, E. Le Bourhis and G. Abadias, “Hardness and residual stresses in TiN-Ni nanocomposite coatings deposited by reactive dual ion beam sputtering,” *Reviews on Advanced Materials Science*, vol. 15, no. 2, pp. 111–117, 2007.

[62] M. Irie, H. Ohara, A. Nakayama, N. Kitagawa and T. Nomura, “Deposition of Ni-TiN nano-composite films by cathodic arc ion-plating,” no. 96, pp. 0–3, 1997.

[63] J. E. Sundgren, “Structure and properties of TiN coatings,” *Thin Solid Films*, vol. 128, no. 1-2, pp. 21–44, 1985.

[64] S. Nagakura, T. Kusunoki, F. Kakimoto and Y. Hirotsu, “ Lattice parameter of the non-stoichiometric compound TiN x,” *Journal of Applied Crystallography*, vol. 8, no. 1, pp. 65–66, 1975.

[65] L. Hultman, J. E. Sundgren and J. E. Greene, “Formation of polyhedral N2 bubbles during reactive sputter deposition of epitaxial TiN(100) films,” *Journal of Applied Physics*, vol. 66, no. 2, pp. 536–544, 1989.

[66] I. Petrov, L. Hultman, J.-E. Sundgren and J. E. Greene, “Polycrystalline TiN films deposited by reactive bias magnetron sputtering: Effects of ion bombardment on resputtering rates, film composition, and microstructure,” *Journal of Vacuum Science & Technology A: Vacuum, Surfaces, and Films*, vol. 10, no. 2, pp. 265–272, 1992.

[67] I. Lopez-Cabanas, J. Llorca, R. Gonzalez-Arrabal, E. I. Meletis and J. M. Molina-aldareguia, “High throughput optimization of hard and tough TiN / Ni nanocomposite coatings by reactive magnetron sputter deposition,” *Surface & Coatings Technology*, vol. 418, 2021.